M 2025

U.PORTO
FEUP FACULDADE DE ENGENHARIA
UNIVERSIDADE DO PORTO

Characterisation of Dissimilar Welds for Railway Vehicle Applications

INÊS CUNHA DA SILVA

MASTER'S DEGREE DISSERTATION IN MATERIAL ENGINEERING
SUBMITTED TO THE FACULTY OF ENGINEERING OF THE
UNIVERSITY OF PORTO

SUPERVISOR
PROFESSORA LAURA RIBEIRO

U.PORTO
FEUP FACULDADE DE ENGENHARIA
UNIVERSIDADE DO PORTO

CANDIDATO	Inês Cunha da Silva	*Código* 202008055
TÍTULO	Characterisation of Dissimilar Welds for Railway Vehicle Applications	
DATA	18-09-2025	
LOCAL	Faculdade de Engenharia da Universidade do Porto – Sala F106 – 14:00	

JÚRI	*Presidente*	Manuel Fernando Gonçalves Vieira	DEMEC/FEUP
	Arguente	Francisco José Gomes da Silva	DEM/ISEP
	Orientador	Laura Maria Melo Ribeiro	DEMEC/FEUP

“So make the friendship bracelets, take the moment and taste it
You've got no reason to be afraid.”
Taylor Swift

ABSTRACT

This dissertation investigates the metallurgical and mechanical properties of dissimilar welded joints between structural steel S355J2 (EN 10025-2:2004) and austenitic stainless steel AISI 301LN (EN 10088-2:2005), aiming to identify the most suitable filler metal for the floor of a railway vehicle. Three filler metals, AWS A5.9 ER307, AWS A5.9 ER308LSi, and AWS A5.22 E309LMoT0-1/4, were applied using Gas Metal Arc Welding (GMAW), more specifically, the Metal Active Gas (MAG) welding process.

The study began with the characterisation of the base materials, in which dilatometric tests were conducted for the S355J2 steel, fatigue tests were performed for the AISI 301LN steel, and tensile tests were carried out for both steels. The welded joints were analysed macroscopically and microscopically to verify the presence of defects and microstructural evolution. The mechanical performance of these joints was evaluated through microhardness, tensile and fatigue tests.

Dilatometric tests on S355J2 steel made it possible to relate the cooling rate to phase transformations, with the microstructure of the HAZ corresponding to a cooling rate of around 10 ºC/s.

Regarding the welding defects, a lack of fusion was observed in the joint that used AWS A5.9 ER308LSi filler metal. Across all joints, microstructural analysis revealed: grain refinement in the stainless steel HAZ due to recrystallisation; ferrite delta within the weld metal, with morphology skeletal, lathy or Widmanstätten dependent on the filler; and in the HAZ of S355J2 steel, Widmanstätten ferrite coexisting with equiaxial ferrite. One detail was that the S355J2 steel used in the joint with AWS A5.22 E309LMoT0-1/4 exhibited reduced pearlite content, suggesting a variation in chemical composition. Mechanical testing identified the joint with AWS A5.9 ER307 as the best-performing joint, displaying superior tensile strength, a higher number of cycles till failure in fatigue tests, as well as a ductile fatigue fracture mode in the machined specimens.

Keywords: MAG; Dissimilar Welding; AISI 301LN; S355J2; Filler Metal; AWS A5.9 ER307; AWS A5.9 ER308LSi; AWS A5.22 E309LMoT0-1/4; Microstructure Evolution; Tensile Tests; Fatigue Tests; Train Floor.

RESUMO

Esta dissertação investiga as propriedades metalúrgicas e mecânicas de juntas dissimilares entre aço estrutural S355J2 (EN 10025-2:2004) e aço inoxidável austenítico AISI 301LN (EN 10099-2:2005), com o objetivo de identificar o metal de adição mais adequado para o piso de um comboio. Utilizaram-se três metais de adição, AWS A5.9 ER307, AWS A5.9 ER308LSi e AWS A5.22 E309LMoT0-1/4, no processo de soldadura por arco elétrico e gás protetor (GMAW), mais especificamente o processo de soldadura com gás ativo (MAG).

O estudo iniciou-se com a caracterização do material base, na qual se realizaram ensaios dilatométricos para o aço S355J2, ensaios de fadiga para o aço AISI 301LN e ensaios de tração para ambos os aços. Analisaram-se as juntas de soldadura macroscopicamente e microscopicamente para avaliar a presença de defeitos e a evolução microestrutural. Avaliou-se o desempenho mecânico das juntas via ensaios de microdureza, tração e fadiga.

Os ensaios dilatométricos do aço S355J2 permitiram relacionar a velocidade de arrefecimento com as transformações de fase, sendo a microestrutura da Zona Termicamente Afetada correspondente a uma velocidade de arrefecimento aproximadamente de 10 ºC/s.

No que se refere a defeitos de soldadura, observou-se falta de fusão na junta com o metal de adição de AWS A5.9 ER308LSi. Em todas as juntas, a análise microestrutural demonstrou: refinamento de grão na HAZ do aço inoxidável devido à recristalização; presença de ferrite delta na zona fundida, com morfologia *skeletal, lathy* ou *Widmanstätten* dependendo do metal de adição; e na Zona Termicamente Afetada do aço S355J2, ferrite do tipo *Widmanstätten* a coexistir com ferrite equiaxial. É de realçar que o aço S355J2 usado para a junta com AWS A5.22 E309LMoT0-1/4 apresentou um menor teor de perlite, sugerindo variação na composição química. Os ensaios mecânicos identificaram a junta com AWS A5.9 ER307 como a de melhor desempenho, apresentando maior resistência à tração, maior número de ciclos até à fratura nos ensaios de fadiga, assim como fratura por fadiga de carácter dúctil.

Palavras-Chave: MAG; Soldadura Dissimilar; AISI 301LN; S355J3; Metal de Adição; AWS A5.9 ER307; AWS A5.9 ER308LSi; AWS A5.22 E309LMoT0-1/4; Evolução Microestrutural; Ensaios de Tração; Ensaios de Fadiga; Piso do Comboio.

ACKNOWLEDGEMENTS

I want to express my heartfelt gratitude to everyone who supported me throughout my academic journey, which culminated in this project.

First, I am deeply grateful to my supervisor, Prof. Laura Ribeiro, for her constant support and for always being available when I needed guidance. I would also like to thank my internship supervisor, Bernardo Begonha, for his patience and for making me feel welcome during the internship. To João Silva, for helping me through the mechanical tests and consistently answering my questions.

I am thankful for several people from the Department of Mechanical Engineering who crossed paths with me and, with their willingness to help, made my days better. To José Ramiro Soares, Maria João Moreira, Maria Cândida Silva, Emília Soares, Abílio Manuel Jesus, José Carlos Fonseca, Joana Angélica Loureiro and Manuel Fernando Vieira. I would also like to thank a few people from the Faculty of Materials Science and Technology from the Technical University of Ostrava who helped me in the ERASMUS^{+} program: Petr Sehnoutka, Monika Losertová and Petr Opěla.

I am especially thankful to those who supported me behind the scenes. To my boyfriend Gonçalo Cruz, thank you for always being there with me and helping me constantly throughout this chapter and these five years. To my best friends Bela, Pena, Mike and Lou, thank you for always making me laugh and lifting my spirits. I would also like to thank my father, my grandparents, and my aunts Ana and Paula for all the help and love they have provided throughout this long journey. Lastly, I want to thank my mother for her unwavering support, love and encouragement, and my brother, because without him, this journey would have been far less fun.

INSTITUCIONAL ACKNOWLEDGEMENTS

I want to thank the Centro de Formação Profissional da Indústria de Fundição (CINFU) for conducting the tensile tests on the S355J2 steel and performing the chemical analysis, especially to Eng. Aurélia Graça and Manuel Alberto.
I would also like to express my gratitude to SERMEC GROUP for allowing me to do an internship, particularly to Mário Duarte and João Cruz.
This work is a result of Agenda "PRODUCING RAILWAY ROLLING STOCK IN PORTUGAL", nr. C645644454-00000065, investment project nr. 55, financed by the Recovery and Resilience Plan (PRR) and by European Union - NextGeneration EU.



TABLE OF CONTENTS

ABSTRACT i

RESUMO ii

ACKNOWLEDGEMENTS iii

INSTITUCIONAL ACKNOWLEDGEMENTS iv

LIST OF FIGURES vi

LIST OF TABLES xiii

LIST OF ABBREVIATIONS xiv

1 INTRODUÇÃO 1

1.1 Motivation 1

1.2 Objectives 2

1.3 Dissertation's Structure 2

2 Literature Review 3

2.1 Overview of S355J2(EN 10025-2:2004) and AISI 301LN steels (EN 10088-2:2005) 3

2.1.1 Steel S355J2 (EN 10025-2:2004) 3

2.1.2. Steel AISI 301 LN (EN 10088-2:2005) 4

2.1.3. Railway Vehicles 5

2.2. Welding of Dissimilar Metals 8

2.2.1 Residual Stresses in a Joint 9

2.2.2 Welding Defects 9

2.2.3 Welding of Austenitic Stainless Steels 12

2.2.4 Welding of Carbon Steel 13

2.2.5 Challenges of Welding Dissimilar Materials 14

2.2.6 Gas Metal Arc Welding 17

3 MATERIALS AND METHODS 22

3.1 Materials 22

3.1.1 Dilatometric Tests 25

3.2 Welding Procedure 25
3.3 Mechanical and Microstructural Characterisation 26
3.3.1 Tensile Tests 27
3.3.2 Microstructure Analysis 27
3.3.3 Microhardness Test 28
3.3.4 Fatigue Tests of AISI 301LN 28
3.3.5 Fatigue Tests of Welded Specimens 30

4 RESULTS PRESENTATION AND DISCUSSION 31
4.1 Dilatometric tests of S355J2 31
4.2 Mechanical Properties of Base Materials 32
4.2.1 Tensile Tests of Base Materials 32
4.2.2 Fatigue Tests of AISI 301LN 33
4.3 Welding Specimen's Characterisation 35
4.3.1 Welding with Filler AWS A5.9 ER307: 4-6% ferrite in WRC diagram 35
4.3.2 Welding with Filler AWS A 5.9 ER308LSi: 10% ferrite in WRC Diagram 39
4.3.3 Welding with Filler AWS A5.22 E309LMoT0-1/4: 28% ferrite in WRC Diagram 41
4.3.4 Microhardness Test of Welded Joints 43
4.3.5 Tensile Tests of Welded Joints 45
4.3.6 Fatigue Test of Welded Joints 46

5 CONCLUSIONS AND FUTURE WORK 51

REFERENCE 52

APPENDIX 58

LIST OF FIGURES

Figure 1: Carriages under production in Portugal: a) pilot coach and 1st class; b) 2º class and bar; c) 2º class [3]. 1
Figure 2:Diagram Fe-C focusing on the eutectoid transformation [11]..... 4
Figure 3: CCT diagram of S355 steel [13]..... 4
Figure 4: Railcar VT2E with stainless steel and carbon steel structure [26]..... 6
Figure 5: Structure of the train under production in Portugal..... 6
Figure 6: Illustrative diagram of rail vehicle floor. 6
Figure 7: Constant amplitude loading [32]. 7
Figure 8: Types of welding processes, highlighting the ones applied to dissimilar metals welding [39]..... 8
Figure 9: Scheme of stress in the joint, by the author. 9
Figure 10: Scheme of residual stress in the joint [48]. 9
Figure 11: Welding defects [49]..... 10
Figure 12: Types of primary phase solidifications depending on the chemical composition of the steel [55]. 13
Figure 13: Schematic representation of solidification mode and morphology in austenitic stainless steel welds [55]. 13
Figure 14: Scheme of the joint microstructure of an X10CrMoVNb9-1 steel [57]. 14
Figure 15: Buttering the carbon steel-stainless steel joint [56]..... 15
Figure 16: Schaeffler diagram [70]. 17
Figure 17: WRC Diagram [18]..... 17
Figure 18: Schematic representation of GMAW [77]. 18
Figure 19: Volt-Ampere Curve for a constant voltage power source [78]..... 19
Figure 20: Relationships between parameters [78]. 20
Figure 21: Thermocouple position in HAZ in a master's thesis [82]. 20
Figure 22: Set up of 4 thermocouples [83]. 20
Figure 23: Base image from [70], extra drawing done by the author..... 24
Figure 24: Base diagram from [18], extra drawing done by the author. 25
Figure 25: Joint design used [94]. 26
Figure 26: Welding sequence done [94]..... 26
Figure 27: Location of test specimens, adapted from ISO 15614-1. 26
Figure 28: Shape of tensile test specimens [91], [93]. 27
Figure 29: Rows of indentation in welded joints. 28
Figure 30: Shape of AISI 301LN fatigue test specimens [102]..... 29
Figure 31: Dimensions of welded fatigue specimens..... 30
Figure 32: Shape of non-machined specimens. 30
Figure 33: Microstructure results of dilatometric tests with: a) 3 ºC/s cooling rate; b) 10 ºC/s cooling rate; c) 30 ºC/s cooling rate; d) 50 ºC/s cooling rate. 32
Figure 34: S-N curve of AISI 301LN..... 33
Figure 35: Microstructure of specimen 8. 34
Figure 36: Microstructures of specimen 6: a) Martensite; b) Austenitic grains with martensite. 35
Figure 37: Macrostructure of welded joint with filler metal AWS A5.9 ER307. 35
Figure 38: Microstructure of: a) BM AISI 301LN (position 1); b) HAZ and FM upper weld pass (position 2); c) HAZ between upper and centre weld pass (position 3). 36
Figure 39: Microstructure of: a) upper right pass (position 4); b) centre weld pass (position 5); c) HAZ (position 6); d) HAZ (position 7)..... 37
Figure 40: Microstructure of: a) HAZ with upper weld pass (position 8); b) HAZ with centre weld pass (position 9); c) HAZ with lower weld pass (position 10). 38
Figure 41: Microstructure of: a) HAZ (position 11); b) BM S355J2 (position 12). 38
Figure 42: Macrostructure of welded joint with filler metal AWS A5.9 ER308LSi..... 39
Figure 43: Microstructure of: a) BM AISI 301LN (position 1); b) HAZ with upper weld pass (position 2); c) upper left pass in FM (position 3); d) centre weld pass in FM (position 4). 40

Figure 44: Microstructure of FM: a) position 5; b) position 6. 40
Figure 45: Microstructure of: a) HAZ with upper weld pass (position 7); b) HAZ with centre weld pass (position 8); c) BM S355J2 (position 9). 41
Figure 46: Macrostructure of welded joint with filler metal AWS A5.9 ER309LMoT0-1/4. 41
Figure 47: Microstructure of: a) AISI 301LN (location 1); b) HAZ of AISI 301LN with upper pass (location 2); c) centre weld pass of filler metal AWS A 5.22 E309LMoT0-1/4 (location 3); d) lower weld pass of filler metal AWS A 5.22 E309LMoT0-1/4 (location 4)..... 42
Figure 48: Microstructure of: a) weld metal in HAZ of AISI 301LN (location 5); b) weld metal in HAZ of S355J2 (location 6)..... 42
Figure 49: Microstructure of: a) HAZ of S355J2 with upper weld pass (location 7); b) HAZ of S355J2 with centre weld pass (location 8); c) HAZ of S355J2 with lower weld pass (location 9); d) S355J2 (location 10). 43
Figure 50: Microhardness profile of the welded joint with filler metal AWS A5.9 ER307..... 44
Figure 51: Macrostructure of welded joint with filler metal AWS A5.9 ER307, with the hardness profile illustrated. 44
Figure 52: Microhardness of welded joint with filler metal AWS A5.9 ER308LSi. 44
Figure 53: Macrostructure of welded joint with filler metal AWS A5.9 ER308LSi, with the hardness profile illustrated. 44
Figure 54: Microhardness of welded joint with filler metal AWS A5.22 E309LMoT0-1/4..... 45
Figure 55: Macrostructure of welded joint with filler metal AWS A5.22 E309LMoT0-1/4, with the hardness profile. illustrated 45
Figure 56: Tensile specimens of the dissimilar joints fracture. 46
Figure 57: Number of cycles to failure for a stress applied of 85% yield stress. 47
Figure 58: Fracture surface of ER307-01: a) on the AISI 301LN steel side; b) on the S355J2 steel side. 47
Figure 59: Fracture surface of ER308-01: a) on the AISI 301LN steel side; b) on the S355J2 steel side; c) lack of fusion defect extended to the lateral surface on the S355J2 steel side. 48
Figure 60: Fracture surface of ER308-02: a) on the AISI 301LN steel side; b) on the S355J2 steel side. 48
Figure 61: Fracture surface of ER309-01: a) on the AISI 301LN steel side; b) on the S355J2 steel side. 49
Figure 62: S-N curve for machined and non-machined specimens. 50
Figure 63: Fracture surface of non-machined specimens. 50

LIST OF TABLES

Table 1: Chemical composition S355J2 [8]. 3
Table 2: Mechanical and physical properties of S355 J2 steel [8-10]..... 3
Table 3: Physical properties of AISI 301LN [20]..... 5
Table 4: Chemical composition of AISI 301 LN [20]. 5
Table 5: Studies on dissimilar welding of austenitic stainless steel and carbon steel. 15
Table 6: Recommended Shielding Gas Selection for GMAW, adapted from [84]. 21
Table 7: Chemical composition of base materials used [85,86]. 22
Table 8: Chemical composition of filler materials used [87-89]. 22
Table 9: Mechanical properties of materials used [85-89]. 23
Table 10: Ni_{eq} and Cr_{eq} for parent metals and filler metals. 23
Table 11: Ni_{eq} and Cr_{eq} of filler metals for WRC Diagrams. 24
Table 12: Conditions of the dilatometric tests [13,91]. 25
Table 13: Operational parameters [94]. 26
Table 14: Dimensions of tensile test specimens [95-97]..... 27
Table 15: Dimensions AISI 301LN fatigue test specimens [102]. 28
Table 16: % Yield Stress in fatigue specimens of AISI 301LN. 29
Table 17: Transformation Temperatures of the steel S355J2. 31
Table 18: Tensile test values of base materials. 33
Table 19: Fatigue results of AISI 301LN. 34
Table 20: Spectrometry results for specimens 6 and 8 of the fatigue test. 35
Table 21: Tensile test results of the welded joints. 45
Table 22: Fatigue results for machined specimens. 46
Table 23: Fatigue results for non-machined specimens. 49

LIST OF ABBREVIATIONS

A. Austenitic
AF. Austenitic-Ferritic
BM. Base Material
CEV. Carbon Equivalent
CHAZ. Coarse Grained Heat Affected Zone
Cr_{eq}. Chromium equivalent
DCEN. Direct Current Electrode Negative
DCEP. Direct Current Electrode Positive
EU. European Union
F. Ferritic
FA. Ferritic-Austenitic
FCC. Face-Centred Cubic
FGHAZ. Fine Grained Heat Affected Zone
FM. Filler Metal
FZ. Fusion Zone
GMAW. Gas Metal Arc Welding
GTAW. Gas Tungsten Arc Welding
HAZ. Heat-Affected Zone
ICHAZ. Inter-Critical Heat Affected Zone
IIW. International Institute of Welding
MAG. Metal Active Gas
MIG. Metal Inert Gas
Ni_{eq}. Nickel equivalent
PWHT. Post Weld Heat Treatment
SAW. Submerged Arc Welding
SMAW. Shielded Metal Arc Welding
WRC. Welding Research Council

1 INTRODUÇÃO

1.1 Motivation

Trains are the most environmentally friendly mode of transport. In the European Union (EU), rail accounted for just 0.3% of transport-related greenhouse gas emissions in 2022 while carrying 8.1% of passengers and 16.6% freight. Thus, rail is central to achieving mobility goals related to the European Green Deal as well as the Sustainable and Smart Mobility Strategy. Stating this, the EU rail network had an investment of €50.8 billion in 2022, split between new infrastructure, maintenance and upgrades [1].
In line with this, a project was launched in Portugal to bring together various companies to build three carriages (Figure 1), enabling the national industry to acquire essential knowledge and strengthen the sector's production capacity [2]. This project was financed by the Recovery and Resilience Plan (PRR), titled "Producing Railway Rolling Stock in Portugal".

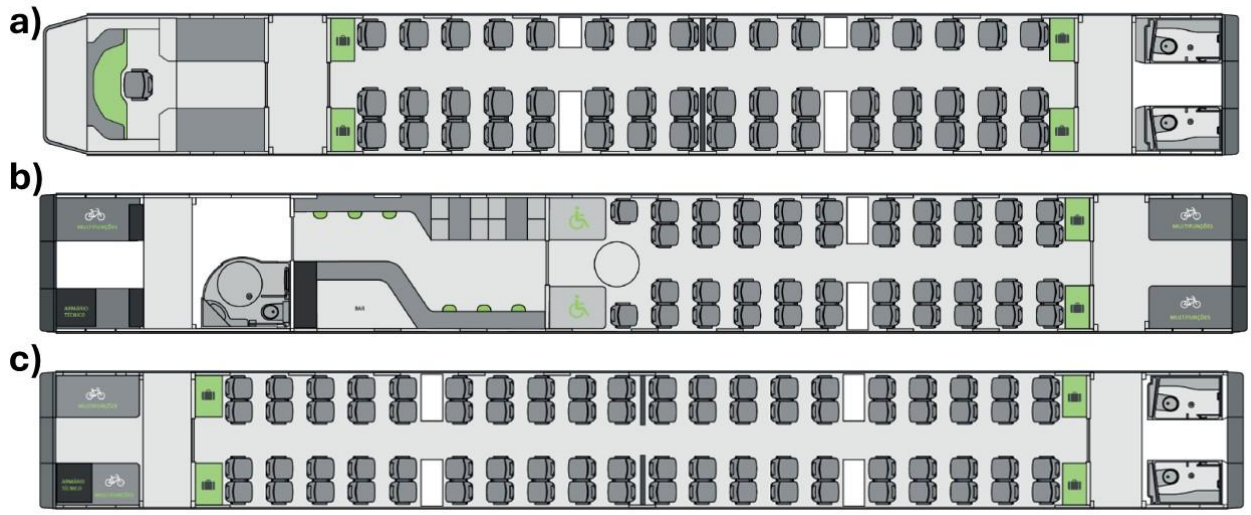


Figure 1: Carriages under production in Portugal: a) pilot coach and 1st class; b) 2º class and bar; c) 2º class [3].

Two of the many organisations involved, SERMEC GROUP and the University of Porto, have come together to enable my participation in this project, which is being conducted as part of the Master's Program in Materials Engineering at the Faculty of Engineering of the University of Porto (FEUP).
SERMEC GROUP is made up of four companies: SERMEC II, SERMEC Windpower, Weartech, and Ibermill. Mário Duarte, the current president, founded the company in 1985. Its primary clients include steelworks, rope manufacturers, cement factories, and refineries, among others. The company's principal activity is the production, repair and commercialisation of components, but maintenance and support services are also provided as part of its operations [4]. SERMEC II contributes to this project across multiple areas, including project management, the design and development of the body, and the secondary structure for interface with subsystems, such as the train floor. Furthermore,

SERMEC II offers consulting services in various operations, including testing procedures, and is responsible for transforming raw materials into structural components through machining, laser cutting, and welding. It also oversees the final assembly of the vehicle [5]. Through the supply of various base materials and welds, tests of welded joints, which will be applied to the train floor, were conducted in this thesis.

1.2 Objectives

This dissertation aims to evaluate, quantitatively and comparatively, the metallurgical characteristics and mechanical properties of dissimilar welded joints produced by Gas Metal Arc Welding (GMAW), which may be used in the train flooring's structure.
In more detail, the specific objectives are to:

1. Characterise the base materials, structural steel S355J2 and stainless steel AISI 301LN, by dilatometric test, tensile and fatigue tests;
2. Characterise the fusion zone (FZ), Heat Affected Zone (HAZ) and base metal of the joints with the filler metal AWS A5.9 ER307, AWS A5.9 ER308LSi and AWS A5.22 E309LMoT0-1/4, through metallographic preparation and microscope;
3. Compare the mechanical properties (microhardness, tensile strength and fatigue performance) of each joint to identify significant differences;
4. Identify welding defects and assess their influence on the mechanical properties of the joints;
5. Select the most suitable filler metal for the application.

1.3 Dissertation's Structure

Alongside Chapter 1, which introduces the topic of this dissertation, this thesis has four more chapters. Chapter 2 provides an overview of the materials used (structural steel S355J2 and stainless steel AISI 301LN) as well as a brief history of railway vehicles. It also focuses on welding metallurgy and potential defects that may occur. A literature review involving dissimilar joints was also done. And finally discusses the GMAW process itself and the influence of its parameters. Chapter 3 outlines the methodology employed in this study to achieve the previously defined objectives. Chapter 4 presents the results of all activities, aiming to address the research questions that guide this dissertation. In the end, Chapter 5 synthesises the most important results and suggests future work to complement this research.

2 Literature Review

This chapter provides an in-depth overview of S355J2 and AISI 301LN steel, focusing on their properties and applications in railway vehicles. The chapter then transitions into welding metallurgy and the challenges associated with dissimilar joints. It also addresses the Gas Metal Arc Welding (GMAW) process, highlighting some parameters of great importance.

2.1 Overview of S355J2(EN 10025-2:2004) and AISI 301LN steels (EN 10088-2:2005)

2.1.1 Steel S355J2 (EN 10025-2:2004)

The steel S355J2 (EN10025-2:2004) is a type of structural steel, also referred to as a C-Mn steel. Some applications of this steel are found in construction (e.g. bridges), ships, pipelines and transportation, such as vehicle frames and suspension components [6,7].
The prefix "S" in this steel denotes Structural Steel, while "355" indicates the minimum yield strength for materials with a thickness below 16 mm, expressed in MPa, and "J2" refers to the minimum impact energy of 27 J at a temperature of -20 ºC [8]. The maximum values of each element in the chemical composition are displayed in Table 1. The mechanical and physical properties are seen in Table 2.

Table 1: Chemical composition S355J2 [8].

	C (%)	Si (%)	Mn (%)	P (%)	S (%)	Cu (%)
S355 J2	0.20	0.55	1.60	0.025	0.025	0.55

Table 2: Mechanical and physical properties of S355 J2 steel [8-10].

Mechanical and physical properties	
Rp 0.2	355 MPa
Rm	470-630 MPa
A	22%
Coefficient of thermal expansion	$12\times 10^{-6}\,K^{-1}$
Thermal conductivity at 20 ºC	40-45 $\frac{W}{m\times K}$

Due to its carbon content of 0.20%, this steel is classified as a hypoeutectoid steel. In equilibrium conditions, the eutectoid transformation occurs at approximately 723 ºC, during which the high-temperature phase, austenite, transforms into two low-temperature phases, ferrite and cementite (Figure 2) [11,12]. Due to the low carbon content, proeutectoid ferrite nucleates in the grain boundaries between A_{c3} and A_{c1} [11,13]. Depending on the cooling rate, this steel may form different phases as seen in Figure 3. This steel can also be classified as an unalloyed one, besides the presence of copper. This element can strengthen steel either through solid solution, up to 12 MPa

through the addition of 0.5%, or by precipitation hardening in a ferrite matrix [14].

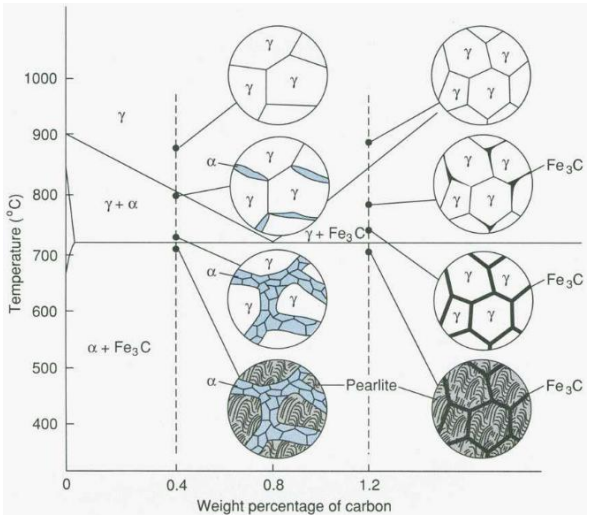


Figure 2: Diagram Fe-C focusing on the eutectoid transformation [11].

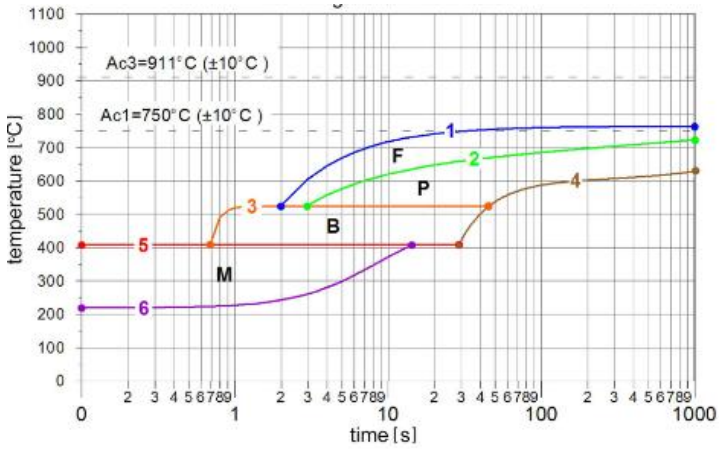


Figure 3: CCT diagram of S355 steel [13].

2.1.2. Steel AISI 301 LN (EN 10088-2:2005)

The steel AISI 301 LN (EN 10088-2:2005), also known as X2CrNiN18-7, is an austenitic stainless steel containing a minimum of 11% chromium, which forms a passive Cr_2O_3 film, providing good resistance to atmospheric corrosion [6,15-17]. Austenitic stainless steels exhibit a "single-phase, Face-Centred Cubic (FCC) structure" demonstrating high ductility, strength, weldability and castability, making it the most used stainless steel [18,19].

The austenitic stainless steels are non-magnetic, and type 301 is a chromium-nickel stainless steel [15]. This steel is classified as "metastable austenitic steel" due to its low alloy content, which allows the austenitic structure to transform into martensite during plastic deformation or upon cooling to cryogenic temperatures [20,21]. Therefore, since this type of steel cannot be hardened by heat treatment, it may be work-hardened to create martensite in the microstructure [21]. The austenite stability, which is the resistance to transformation to martensite during deformation, depends on the nitrogen content. When the steel is subjected to temperatures between 700 ºC and 800 ºC, nitrogen

promotes the formation of Cr_2N precipitates, reducing the stability of austenite [22].
The applications of this steel are springs, belts, utensils, structural parts and trailer bodies [16]. Also, austenitic stainless steels are often used when only certain parts of the welded structure require corrosion resistance [23].
These steels exhibit a high coefficient of thermal expansion and low thermal conductivity (Table 3), compared with the structural steel. When heated, such as during welding, the material expands but inhibits rapid heat dissipation, creating a temperature gradient within it, making it prone to distortion [19].

Table 3: Physical properties of AISI 301LN [20].

Mean coefficient of thermal expansion (between 20 ºC and 100 ºC)	Thermal conductivity at 20 ºC
19 X 10^{-6} K^{-1}	15 $\frac{W}{m \times K}$

The chemical composition of this steel is shown in Table 4, and its C1000 grade refers to the tensile strength level of this steel [17,20].

Table 4: Chemical composition of AISI 301 LN [20].

	C (%)	Si (%)	Mn (%)	P (%)	S (%)	Cr (%)	Ni (%)	N (%)
AISI 301LN	0.03	1.00	2.00	0.045	0.015	16.50 - 18.50	6.0 - 8.0	0.10 - 0.20

2.1.3. Railway Vehicles

Trains consume the least energy per person per distance among all the transportation systems, that is, half the energy of buses and one-sixth that of cars, making them the most environmentally friendly option. To meet the demands for weight reduction, high strength, and recyclability, a multi-material structure can be employed, where different materials are joined through welding [24,25]. Trains are subjected to various forces throughout their operation, so ensuring their structural integrity is essential, especially given their typical service life of around thirty years [26].
An example of a vehicle with a carbon steel and a stainless steel structure is seen in Figure 4. This vehicle uses types of steel comparable to those used in our project. Stainless steel is used for the external sheeting, while structural steel is employed in the floor and the window frame construction [26].

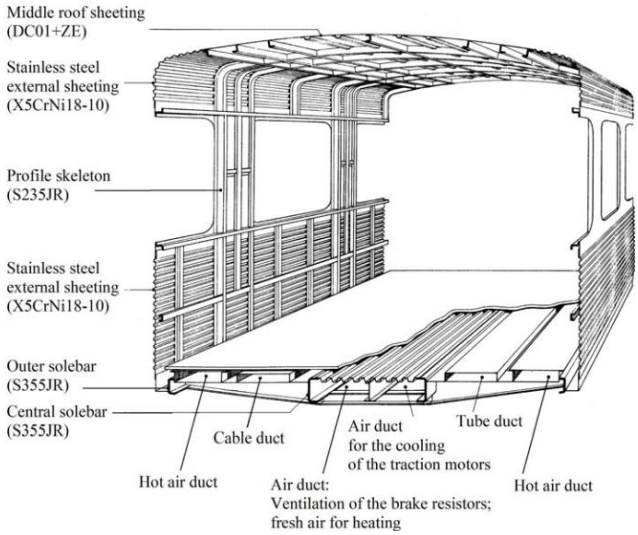


Figure 4: Railcar VT2E with stainless steel and carbon steel structure [26].

In a welded steel structure, carbon steel is used where thicker sections are required [27]. Arc welding is commonly applied to the structural frames of the floors, sides and roofs, typically using Gas Metal Arc Welding (GMAW) with an austenitic stainless steel filler [27]. Figure 5 illustrates the structural design of the train that is currently under production in Portugal. This project emphasises the welding involved in the train's construction, specifically on its floor. At both ends of the train floor, the material employed is S355J2, and it is welded by GMAW to AISI S301LN located in the middle of the floor, as illustrated in Figure 6.

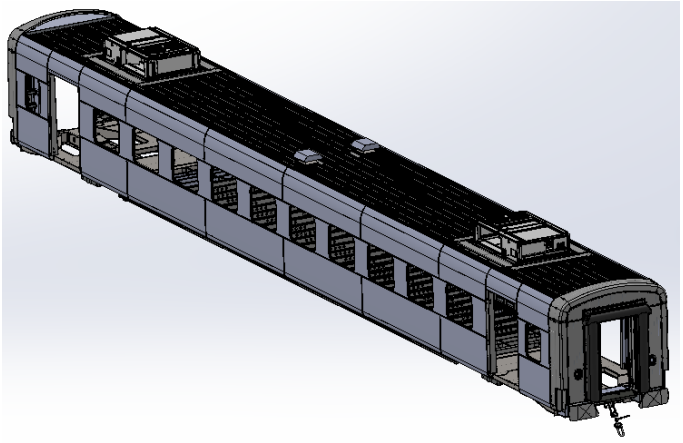


Figure 5: Structure of the train under production in Portugal.



Figure 6: Illustrative diagram of rail vehicle floor.

2.1.3.1. Fatigue in a Railway Vehicle

Fatigue is the "localised damage process of a component produced by cyclic loading", such as the floor of the train, which experiences dynamic loads from the movement of the train, passenger weight and vibrations [28-30]. The standard EN 15085-3:2022+a1:2023 establishes the stress category and stress factor for materials used in railway vehicles. Due to its location in the railway vehicle, this joint is considered high stress (stress factor>0.9) because of the potentially severe consequences in the event of failure [31]. The fatigue process consists of 3 phases [28,32]:

- Crack Initiation: starts in a shear plane near a high-stress concentration, for example, in a notch present. This is a discontinuity in the material introduced by the design or the manufacturing process that leads to crack initiation. In welded joints, residual stresses can favour this phase;
- Propagation: the crack tends to grow along the plane of maximum shear stress;
- Failure: the system is unstable and can't manage another cycle of tension and fractures. This phase compromises the structural integrity and safety of railway vehicles.

In welded structures, joints are particularly susceptible to fatigue failure, especially when dissimilar metals are involved, due to the complex combination of chemical compositions and phases within the joint [24]. Other factors that influence fatigue are welding defects, tensile residual stresses and distortions [33,34]. In welded structures, crack initiation typically occurs at the joint and is a brief stage, while propagation takes place in the remaining material, with most of the time being spent in this stage [35,36].

The fracture surface, when analysed, can be divided into three regions: radial lines indicating crack initiation, lines indicating crack propagation, and a rough surface representative of a brittle fracture [35,37]. Fatigue can be classified into two regimes: high-cycle fatigue, which involves 10^5 or more cycles and is dependent on the crack initiation period, and low-cycle fatigue, limited to 10^5 cycles, where crack propagation plays a significant role [28]. The main characteristic of cyclic loading in a fatigue test is illustrated in Figure 7, and Equations 1-4 are used to calculate the test parameters [32,38].

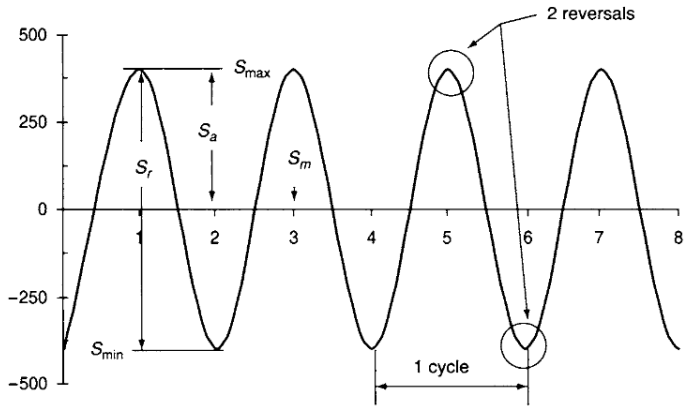


Figure 7: Constant amplitude loading [32].

$$\boldsymbol{Sa} = \frac{(\boldsymbol{Smax} - \boldsymbol{Smin})}{\mathbf{2}} \quad (1)$$

Where Sa is the stress amplitude, Smax is the maximum stress, and Smin is the minimum stress.

$$\boldsymbol{Sm} = \frac{(\boldsymbol{Smax} + \boldsymbol{Smin})}{\mathbf{2}} \quad (2)$$

Where Sm is the mean stress, Smax is the maximum stress, and Smin is the minimum stress.

$$R = \frac{Smin}{Smax} \quad (3)$$

Where R is the stress ratio, Smax is the maximum stress, and Smin is the minimum stress.

Through the S-N methodology, the data is obtained by recording the number of cycles until the sample ruptures or until a predefined threshold is reached. The equation can describe the curve of the test represented in:

$$log\Delta S = logC - clog\Delta N \quad (4)$$

Where ΔS is the stress amplitude, ΔN is the number of cycles until rupture, c and C are material and test constants, respectively.

2.2. Welding of Dissimilar Metals

Welding is a process of joining materials through pressure or fusion, allowing joining thicknesses from millimetres to dozens of centimetres. This process can be applied to different materials, forms, and positions. Although various welding methods exist, only some are reported in the literature as suitable for dissimilar welding, such as the one addressed in this thesis. These processes are highlighted in purple in Figure 8 [39-41].

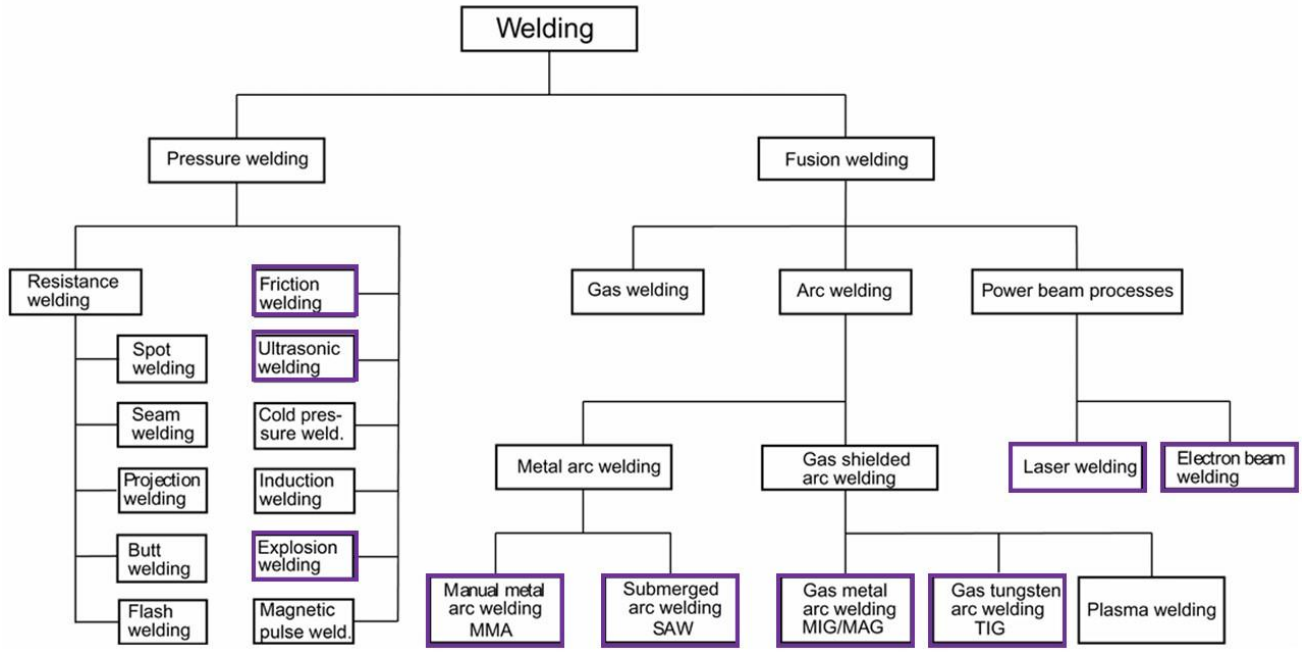


Figure 8: Types of welding processes, highlighting the ones applied to dissimilar metals welding [39].

Fusion welding is one of the most commonly used processes. Because of the metallurgical changes, it is relevant to analyse the joints [42]. The typical structure of a welded joint consists of three zones: the Fusion Zone (FZ), the Heat-Affected Zone (HAZ) and the unaffected base metal zone. In the FZ, and especially close to the HAZ, a chemical composition gradient is usually observed due to chromium migration from the base material to the FZ when dealing with carbon steel [43]. A consideration to have is that the FZ should be "equal to or stronger than the weaker material being joined" [41].
The literature provides limited information on welding processes involving simultaneous

variations in both material type and thickness, as those used in this work. When such cases are reported, the thickness variations are relatively minor, typically around 50% [44] and 20% [45], in contrast to the 140% thickness difference addressed in this work.

2.2.1 Residual Stresses in a Joint

Due to thermal changes and restrictions in movement, stresses develop within the joint when welding. A filler metal is deposited along the joint in liquid form. This material tries to expand, but the cold material restrains it by compressing forces. During the cooling phase, the metal in the FZ attempts to contract but is restrained by the base material, creating residual tensile stresses. Due to material equilibrium, compressive stresses were developed [36,46,47]. A schematic representation of these stresses is in Figure 9. In a welded joint (Figure 10), stress concentrations are predominantly observed at the weld toes, which represent the transition zone between the weld bead and the base material. In comparison, the weld roots exhibit less stress concentration, although it is still relevant [47,48].

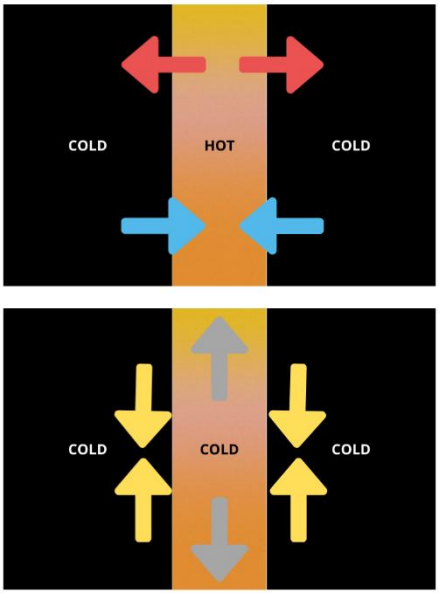


Figure 9: Scheme of stress in the joint, by the author.

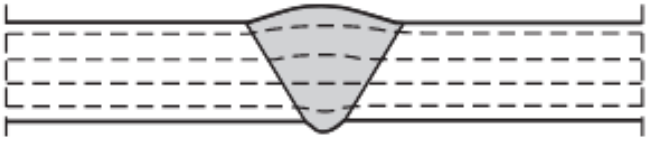


Figure 10: Scheme of residual stress in the joint [48].

2.2.2 Welding Defects

Quality is established in the service requirements and encompasses the chemical composition, mechanical properties, and hardness of the materials. Discontinuities are related to the process or metallurgical behaviour and can alter the stress distribution and mechanical properties [49]. The usual welding defects are shown in Figure 11.

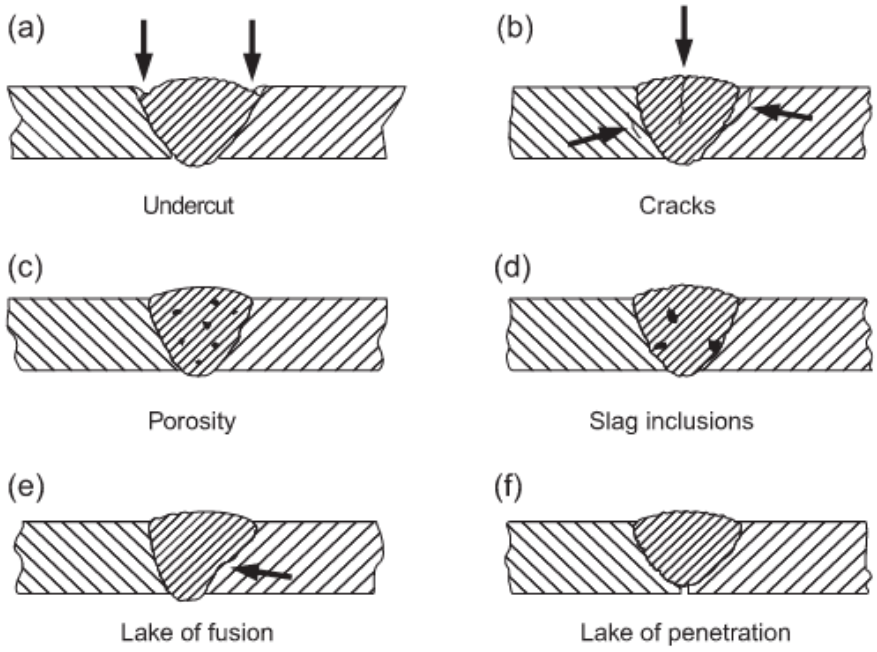


Figure 11: Welding defects [49].

- **Undercut**

Undercut can be caused by improper welding technique and/or excessive current. This type of defect acts as a stress concentrator, reducing fatigue properties. The acceptability of the undercut depends on analysing its depth and length.

Cracking can occur in four forms: cold, hot, lamellar and stress-corrosion [18,49].

- **Cold cracking**

Cold cracking occurs after solidification when three conditions are present: hydrogen in the material, a crack-susceptible microstructure (such as martensite) and high residual stress [49]. Hydrogen originates from humidity in the shielding gas, the electrode coating in Shielded Metal Arc Welding (SMAW), the flux in Submerged Arc Welding (SAW) and the base material. Preheating can be a solution to remove the hydrogen [50]. Another vital precaution is performing post-heating at a temperature below the martensite formation finish point. This allows time for hydrogen to diffuse, thereby delaying the maximum stress value, reducing the risk of hydrogen cracking. In this approach, no metallurgical modification occurs [51]. Another solution is to use a low-hydrogen filler metal [50].
The mechanism of hydrogen that leads to cracking is the following [50,52]:

- Formation of hydrogen ions because of humidity;
- Dissolution of the ions into the weld pool;
- Diffusion of hydrogen through the microstructure. But if there is martensite present, the hydrogen has extremely low solubility and eventually forms hydrogen molecules (H_2);
- These molecules accumulate till a critical concentration and build up internal stress to a level that causes a crack.

The carbon equivalent is crucial in this type of cracking because it determines the steel's

susceptibility to forming a fragile structure during welding [50].

- **Hot cracking**

Hot (or solidification) cracking occurs at elevated temperatures during, or shortly after, solidification [49]. A eutectic is a constituent that has the lowest melting point, while other constituents exhibit a range of melting points. This eutectic is pushed towards the centre of the weld, the last place to cool, where cooling induces high stress, causing the joint's centre to separate. In steel, sulphur is the element responsible for generating a low melting point eutectic (FeS). This cracking can be avoided by adding manganese to form manganese sulphide (MnS), which has a melting point similar to steel. Additionally, removing surface contaminants and using a material with a sulphur content below 0.03% may help prevent this issue [52,53].

- **Lamellar Tearing**

Lamellar tearing/cracking results from high stress perpendicular to MnS inclusions. This structure is parallel to the material thickness. It most commonly appears in T or corner joints [49,52]. One way to prevent lamellar tearing is by applying a buttering layer around the joint, using a more ductile filler material. This approach reduces stress in the material as the added layer absorbs it. An alternative approach is to modify the joint design to reduce stress levels [52].

- **Stress-corrosion cracking**

Stress-corrosion cracking occurs in austenitic stainless steel when the material is exposed to tensile stress in a corrosive environment. Crack propagation can be either intergranular or transgranular, with transgranular cracking typically observed in chloride and caustic media. This type of cracking is initiated in the weld due to the high residual stress level there [18].

- **Porosity**

Porosity is a gas entrapped in the FZ and is usually spherical. The causes are poor welding technique or poor weld hygiene. Generally, porosity is not a serious problem in normal loading and fatigue conditions. However, it becomes significant if the weld needs to resist brittle fracture at lower temperatures, as this defect can facilitate crack initiation [49].

- **Slag inclusions**

Slag inclusions are particles trapped within the joint as a result of the welding process. The ideal scenario is that the slag inclusion goes to the surface [49].

- **Lack of fusion and penetration**

Lack of fusion and incomplete penetration are critical defects, as they can create stress concentrations that serve as initiation sites for cracks. Lack of fusion results from insufficient welding current, while lack of penetration is caused by inadequate heat input and improper joint design [49].

2.2.3 Welding of Austenitic Stainless Steels

All austenitic stainless steels, except AISI 303, are easily welded, and the joints obtained are ductile [19].

However, two key factors must be considered when welding these steels. The first is the carbide precipitation in unstabilised stainless steels [19,52]. Precipitation of chromium carbides occurs between 425 ºC and 900 ºC (some authors also state temperatures ranging between 600 ºC and 850 ºC), which reduces the chromium content in the steel and makes it susceptible to intergranular corrosion [19,52]. This originates a sensitised zone, usually in the HAZ [52]. A straightforward way to prevent this is by using a low-carbon stainless steel, which reduces the amount of carbon available to form the chromium carbides, or by using stabilised stainless steel, which has titanium or niobium because they are stronger carbide formers than chromium, so the chromium can stay in solution and protect against corrosion [52]. This issue can also be resolved through an annealing process, which involves heating the steel to 1100 ºC to dissolve the chromium carbides, followed by rapid cooling to prevent their precipitation [19]. Another solution is to minimise the heat input, thereby reducing the time the steel remains within the critical temperatures [52].

Additionally, the formation of low-melting impurities can be a problem because it causes fissures in the grain boundary, but this can be minimised if ferrite is produced, because this constituent can absorb these impurities [19]. More specifically, if the ferrite forms through the primary solidification mode (mode Ferritic-Austenitic: FA), the low-melting-point liquid phase does not “wet” in the austenite-ferrite interphase boundaries as easily as in austenite or ferrite boundaries, leading to a higher resistance to solidification cracking [54]. This solidification mode depends on the relationship between the chromium equivalent (Cr_{eq}) and the nickel equivalent (Ni_{eq}). Specifically, in austenitic stainless steel welds, there are four modes of solidification (Figure 12). The mode Austenitic (A) results in a fully austenitic microstructure because the primary phase after liquid is austenite only. The mode Austenitic-Ferritic (AF) has the same primary phase as the last one, but during cooling, a small part of ferrite can form. The mode Ferritic-Austenitic (FA) has a primary phase of ferrite, and in the final stages of solidification, austenite can form. In mode Ferritic (F), ferrite is once again the primary phase. As the Cr_{eq} to Ni_{eq} ratio increases, the solidification mode shifts further to the right in Figure 13 [55].

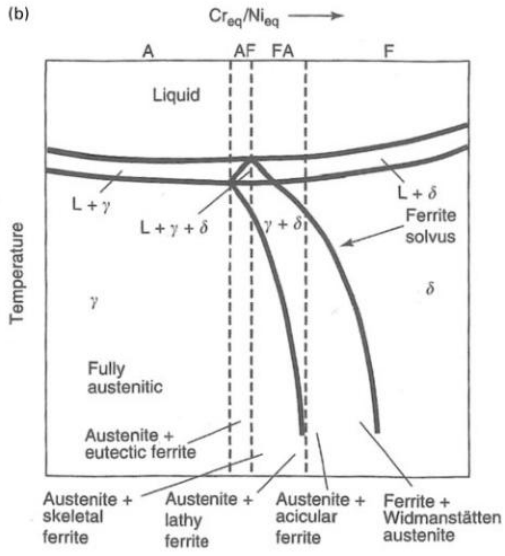


Figure 12: Types of primary phase solidifications depending on the chemical composition of the steel [55].

Although different modes of solidification exist, a single weld can exhibit various ferrite morphologies due to local variations in chemical composition (Figure 13) [55].

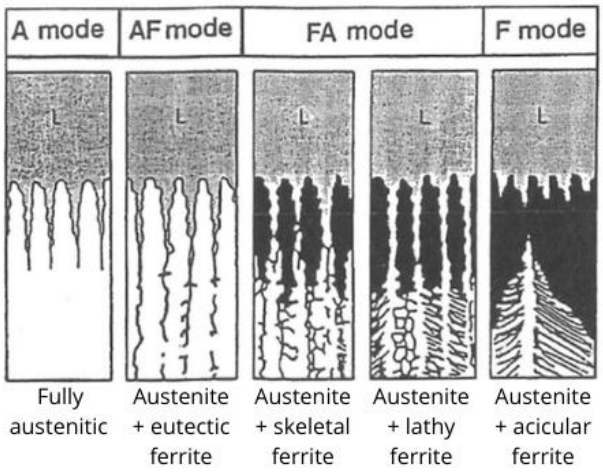


Figure 13: Schematic representation of solidification mode and morphology in austenitic stainless steel welds [55].

2.2.4 Welding of Carbon Steel

Welding in carbon steel generates a temperature gradient that spans from the melting point at the joint to ambient temperature farther away [56]. The typical microstructure of a weld joint is shown in Figure 14. Due to the welding process and the thermal changes, there is a HAZ that can be divided into subzones that have different microstructures and properties [57]:

- Coarse Grained Heat Affected Zone (CGHAZ): the temperatures go above A_{c3} and result in coarse grains of austenite;
- Fine Grained Heat Affected Zone (FGHAZ): temperatures go up to A_{c3}, resulting in smaller austenite grains;
- Inter-Critical Heat Affected Zone (ICHAZ): temperatures between A_{c3} and A_{c1}, causing partial transformation of austenite during the heating phase. This zone usually has the

lowest value of hardness;

- Over-tempered zone: temperatures are lower than A_{c1}, so the microstructure does not undergo phase transformation. The microstructure is tempered, and there is coarsening of precipitation.

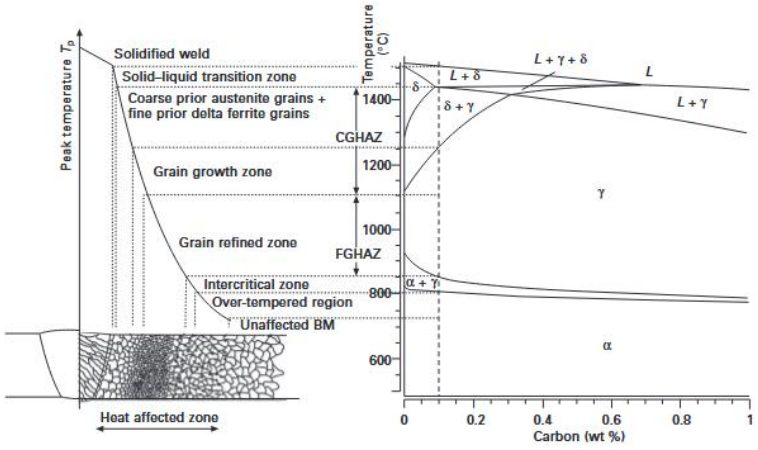


Figure 14: Scheme of the joint microstructure of an X10CrMoVNb9-1 steel [57].

2.2.4.1 Carbon equivalent in carbon steel

Weldability is "the ability of a material to be welded and still retain its specified properties". It depends on the chemical composition, the process used, and the mechanical properties. Poor weldability leads to cracking problems, with a contributing factor being a microstructure prone to cracking [58].
This susceptibility depends on the carbon and other elements present in the carbon steel. Including the percentage of the most critical constituents in Equation 5, a measure of the material's hardenability is calculated [58,59]. In simpler terms, give a metric of how susceptible the carbon steel is to cracking. It is considered good weldability if the Carbon Equivalent (CEV) is up to 0.4%, limited between 0.4 and 0.5%, and poor above this value [58].

$$CEV = C + \frac{Mn}{6} + \frac{Cr + Mo + V}{5} + \frac{Ni + Cu}{15} \quad (5)$$

2.2.5 Challenges of Welding Dissimilar Materials

The aim of joining different materials is to get a good-quality joint. However, failure can result from the formation of brittle phases and undesirable residual stress distribution across the joint, caused by differences in coefficients of thermal expansion [23,60]. A consideration about welding stainless steel and carbon steel is that stainless steel has a 50% higher coefficient of thermal expansion and a 40% lower coefficient of thermal conductivity, which means that the joint can have more contraction in the area of this material [61]. This issue can be addressed using rigid fixturing (also known as temporary attachments) or heat sinks, which help dissipate the heat generated during the welding process [62-64].
Significant problems with dissimilar welds are the microstructural heterogeneity and the carbon migration from higher carbon steel to lower carbon steel [23,60]. When austenitic

stainless steel is joined to carbon steel, it is often necessary to perform a Post-Weld Heat Treatment (PWHT) at temperatures between 550 ºC and 675 ºC to relieve residual stresses. However, this heat treatment can cause intergranular corrosion due to precipitation of chromium-rich phases. If this presents a limitation, an effective solution can be buttering the carbon steel. Buttering involves applying a layer of austenitic stainless steel filler metal, commonly E309, onto the carbon steel, followed by PWHT to relieve stresses. After that, the stainless steel is welded to the buttered layer. In this way, the joint is a conventional stainless steel joint (Figure 15) [19,56].

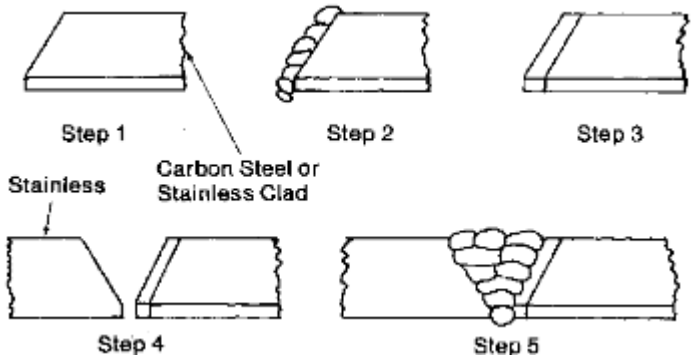


Figure 15: Buttering the carbon steel-stainless steel joint [56].

When welding these two types of steel, a stainless steel filler metal with high alloy content is typically employed. This filler inhibits martensite formation and promotes ferrite formation, which helps prevent hot cracking by incorporating sulphur and phosphorus, elements that could otherwise cause segregation in the FZ [43,56,65]. Many types of filler metal are recommended, such as stainless steel wires ER308, ER309, ER312, ER316 and ER347 [56,66].

Several studies have investigated the welding of austenitic stainless steel with carbon steel (Table 5). A carbon-depleted zone in the HAZ has been observed on the higher carbon side [23,60]. This phenomenon occurs because chromium exhibits a stronger affinity for carbon than iron. At high temperatures, above 425 ºC, carbon diffuses from the base metal into the weld metal, where it combines with chromium to form carbides [66].

Table 5: Studies on dissimilar welding of austenitic stainless steel and carbon steel.

Reference	Materials	Filler metal	Welding process	Joint type	Failure in the tensile test	Failure in the fatigue test
[23]	Structural steel (S355MC) + Stainless steel (AISI 304, 314 and 316L)	ER308LSi	Metal Inert Gas (MIG)	Butt Weld	Structural steel (S355MC)	-

Table 5: Studies on dissimilar welding of austenitic stainless steel and carbon steel (cont.).

Reference	Materials	Filler metal	Welding process	Joint type	Failure in the tensile test	Failure in the fatigue test
[60]	Ferritic steel (St37–2) + Austenitic stainless steel (AISI 304)	Austenitic filler metal	Gas Tungsten Arc Welding (GTAW)	Square Butt Weld	Ferritic steel (St37–2)	Ductile tearing mode fracture in the weld metal
[67]	AISI 1045 + AISI 304	Electrode E6013 and E7016	SMAW (Shielded Metal Arc Welding)	double bevel groove, V-groove, and double V-groove	-	-
[68]	AISI 1020/AISI 1045 + AISI 304/AISI 316	Electrodes Eutectrode 52 NG, 54 NG e 57 NG	SMAW (Shielded Metal Arc Welding)	Butt weld	Weld metal	-
[69]	Austenitic stainless steel (304) and low-carbon steel	Austenitic filler metal	GTAW/SMAW	Butt weld	-	-

2.2.5.1 Schaeffler and DeLong diagram for Dissimilar Welding

For this type of welding, diagrams can be helpful to predict the resulting microstructure. The Schaeffler diagram (Figure 16) predicts the resulting microstructure based on the chemical composition of both the base materials and the filler material, allowing a more accurate choice of the filler metal through comparison [61,64]. A relevant area in this diagram is the ferrite one, because fully austenitic joints are more susceptible to hot cracking than joints containing about 5% or more ferrite [41,43]. This diagram was further refined using the DeLong diagram, which is more specific to the 3xx series stainless steels, and the Welding Research Council (WRC) diagram, which allows the prediction of ferrite content (Figure 17) [18].

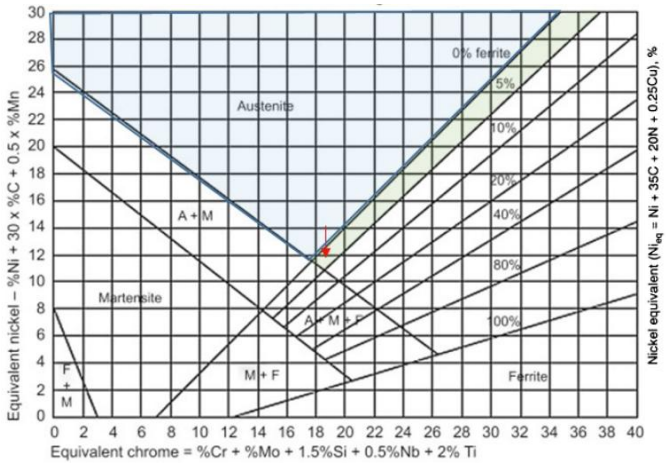


Figure 16: Schaeffler diagram [70].

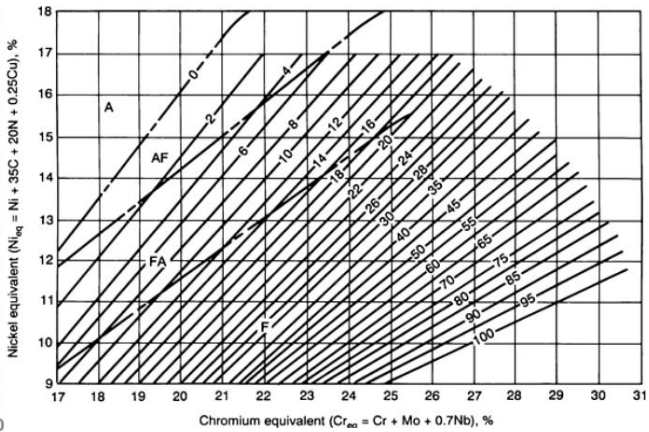


Figure 17: WRC Diagram [18].

2.2.5.2 Multi-pass Welding on Dissimilar Joints

Multi-pass welding is often employed for dissimilar joints. One disadvantage is that the joint becomes more complex due to the thermal cycles from multiple passes, which affect the microstructure, hardness and mechanical properties [69]. This is because some regions of the carbon steel can be reheated to temperatures high enough to allow austenitisation and can transform into different components during the cooling part of the transformation [71]. On the other hand, the subsequent heat can reduce the residual stresses and the energy input per pass, thereby limiting grain growth. Also, the previous passes create a certain preheat and slow down the cooling rate for the next pass, in joints with thickness homogeneity [72]. In a stainless steel-carbon steel joint, a reduction in grain size within the HAZ was observed compared with single-pass welding, along with a transition in the ferrite phase from cellular to columnar dendritic morphology in the weld metal [69].

2.2.6 Gas Metal Arc Welding

Gas Metal Arc Welding (GMAW) is “the leading welding process in most industrial countries” and one of the most used welding processes to join dissimilar materials, including carbon steel with stainless steel [40,41,73]. GMAW encompasses both MIG welding, which uses an inert shielding gas, and MAG (Metal Active Gas) welding, which employs an active shielding gas. MIG welding is ideal for aluminium and non-ferrous materials, such as copper [74]. Some applications are sheet metal welding, fabrication of pressure vessels, bridges, pipelines and repair of automobiles [75]. MAG welding is sometimes used because CO2 is less expensive than argon, which is typically used in MIG welding [74]. Applications include pipe welding, automotive maintenance and production, and shipbuilding [76].

Some advantages of GMAW in general include the ability to weld steel, aluminium, and copper; the ability to weld an extensive range of thicknesses, possibly even higher than 30 mm; and suitability for different welding positions [73,77]. A scheme of GMAW is shown in Figure 18.

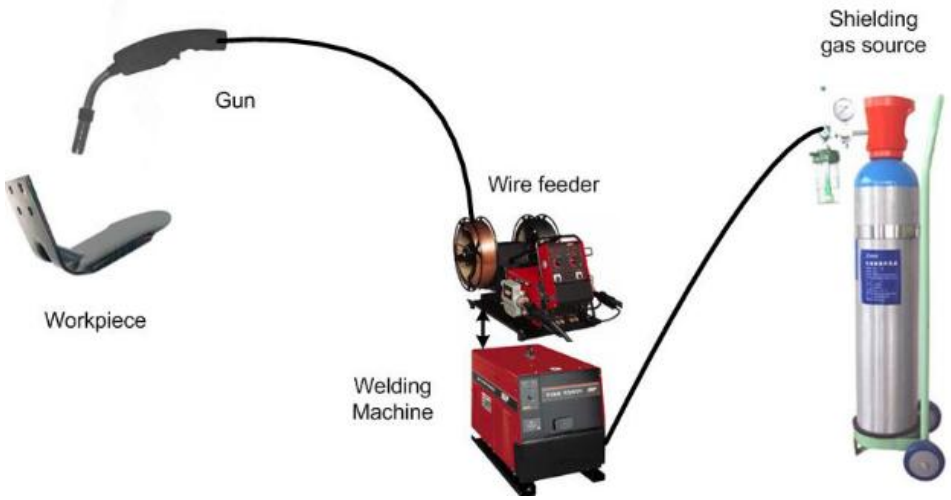


Figure 18: Schematic representation of GMAW [77].

The principle of MIG/MAG welding is an arc created between the workpiece and the consumable electrode. Electrical energy passes through the wire, usually connected to the positive pole of the power source, and the workpiece is connected to the negative pole [73]. This polarity is known as Direct Current Electrode Positive (DCEP) or straight polarity, which creates a stable arc, low spatter and good penetration. If the wire is connected to the negative pole of the power source, it is referred to as a Direct Current Electrode Negative (DCEN). However, it is rarely used because the drop size is large, and the arc is unstable [78]. The shielded gas protects the arc and the weld pool as it flows through the welding gun [73]. Because the electrode wire is fed automatically, this process is semi-automatic and requires less skill from the operator [77].

This process has three main transfer modes: globular transfer, spray transfer, and short-circuit transfer. In the globular transfer mode, the filler metal forms globular drops that are larger in diameter than the electrode wire. This mode occurs at current levels lower than those in spray mode, but higher than those in short-circuit transfer [78]. This transfer mode relies on gravity and is limited to flat and horizontal welding positions [79]. Spray transfer occurs with a higher current from these transfer modes [78]. The drop is smaller than the filler wire. In this mode, the arc is stable and spatter-free [73,79]. The short-circuit mode operates at the lowest values of current, resulting in minimal energy input [78,79]. The goal is to obtain a small droplet and spatter fine enough to impede adhesion to the piece [73].

There are specific parameters associated with this technique that are worth analysing [73,77-79]:

- Power source: It provides a constant-voltage output, which, when used with a constant-speed wire feeder, helps stabilise the arc length. A graphic of this type of power source is shown in Figure 19, illustrating a self-regulated system. Therefore, if the arc length changes during operation, the current adjusts to restore the voltage to its ideal value. For example, if the arc length is higher momentarily, the arc current will drop, and the power source will increase the current.

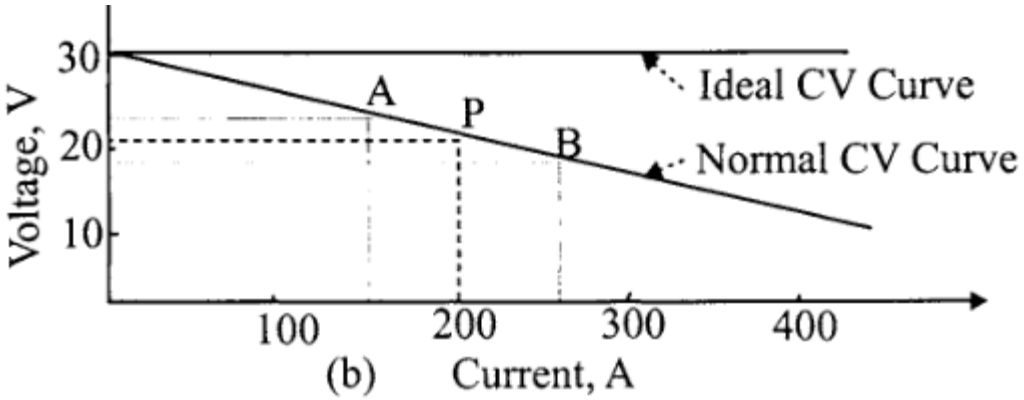


Figure 19: Volt-Ampere Curve for a constant voltage power source [78].

- Energy input: Energy applied over the weld length. The higher the energy input, the slower the cooling rate [72]. Through Equation 6, it is possible to calculate the energy input [80]:

$$H = \frac{EI}{V} \quad (6)$$

Where E is the voltage (V), I is the current (A), V is the travel speed (mm/s), and H is the energy input (J/mm)

To have a more precise value of energy input, Equation 7 can be used, adding the efficiency of the process, and calculating the net energy input [80]:

$$H\ net = \frac{fEI}{V} \quad (7)$$

Where f is the heat transfer efficiency

- Voltage: Increasing the voltage results in an increase in arc length and a wider weld bead. However, excessive voltage can cause undercutting.
- Current: This is indirectly set by the wire feed speed. Higher values of current result in greater energy input, causing faster electrode melting, increasing heat transfer to the piece, and a larger weld bead.
- Travel Speed: A higher travel speed produces less heat, resulting in a smaller weld bead. This parameter is independent of current and voltage and is controlled by the welder.

To put these parameters in a schematic representation, Figure 20 is useful [78].

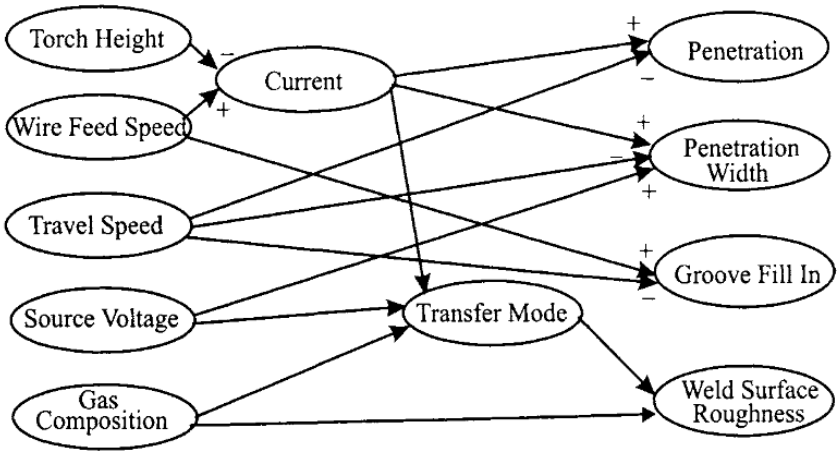


Figure 20: Relationships between parameters [78].

2.2.6.1 Cooling Rate

The cooling rate is an important parameter because it determines the microstructure and properties of the joint [80]. The faster the material cooled, the greater the probability of forming smaller grains. A high cooling rate can induce the formation of martensite in the carbon steel, resulting in a hard and brittle phase [81]. Thus, the cooling rate determines the formation of different phases, which are closely linked with the mechanical properties and microstructure of the steel [82]. One important relationship is that the higher the energy input, the lower the cooling rate is [83]. The cooling time between 800 °C and 500 °C is the most used parameter and can be calculated using Equation 8 [83].

$$Cooling\ Rate = \frac{Temperature\ range\ from\ 800\ °C\ to\ 500\ °C}{Time\ taken\ from\ 800\ °C\ to\ 500\ °C\ during\ cooling} \quad (8)$$

This parameter is important in the HAZ. Studies have been conducted to develop a system that measures the cooling rate in this zone while welding. With S355J2, an experiment was done using a K thermocouple and welding the thermocouple wires. The thermocouple recorded the cooling time between 800 °C and 500 °C and was placed perpendicular to the HAZ, as displayed in Figure 21 [82]. Another approach to measuring this parameter was done using mild steel plates in SAW welding. A thermocouple type K was also used in this investigation, but the configuration differs from the previous one. Four holes were made from the centre to the right, 1 mm apart from each other, as seen in Figure 22 [83].

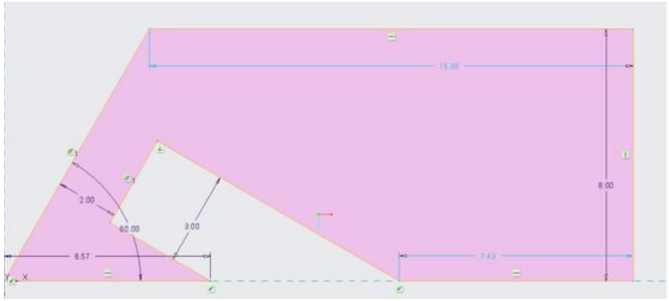


Figure 21: Thermocouple position in HAZ in a master's thesis [82].

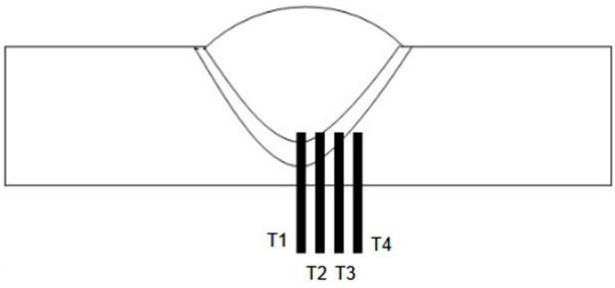


Figure 22: Set up of 4 thermocouples [83].

2.2.6.2 Shielding Gases

Many gases can be used in GMAW, but argon, carbon dioxide, helium, and oxygen are typically used for carbon steel and stainless steel (Table 6). Argon promotes excellent arc stability and penetration in such a way that, because of the high current density of the arc, it results in a fingerlike penetration. Carbon dioxide is generally used in joining carbon steel. Produces spatter and weld surfaces with irregular shapes. Helium has higher thermal conductivity, providing both heat input and an inert atmosphere. Argon mixed with oxygen increases the filler metal droplet rate and produces a more fluid weld pool, resulting in a larger weld bead. A mixture of argon and carbon dioxide is commonly used in welding carbon and low-alloy steels. Depending on the carbon dioxide, the penetration can be increased. Mixtures of argon, oxygen and carbon dioxide can be used in short-circuit, globular and spray transfer modes for both carbon and alloy steels. Mixtures of argon, helium, and carbon dioxide have increased heat input. When helium content is higher than 60% the transfer mode is short-circuit or globular. Finally, mixtures of argon, carbon dioxide and hydrogen are for austenitic stainless steel. Due to the hydrogen, this blend shall not be used for carbon steel [84].

Table 6: Recommended Shielding Gas Selection for GMAW, adapted from [84].

Material	Thickness (mm)	Transfer mode	Shielding gas
Carbon steel	>3,2	Short-circuiting	Ar-15CO_2 Ar-25CO_2 CO_2
		Globular	Ar-25CO_2 CO_2
		Conventional Spray arc	Ar-1O_2 Ar-2O_2 Ar-5CO_2
		Pulsed spray	Ar-5CO_2 Ar-He-CO_2 Ar-CO_2-O_2
Stainless steel	All sizes	Short-circuiting	Ar-He-CO_2 He-Ar-CO_2 Ar-1O_2 Ar-2O_2
		Spray arc	Ar-He-CO_2 Ar-1O_2 Ar-2O_2
		Pulsed spray	Ar-He-CO_2 Ar-1O_2 Ar-2O_2

3 MATERIALS AND METHODS

This chapter presents the materials and methodology used in this dissertation. The chemical composition and mechanical properties of the steels applied are presented, and the expected microstructure of the weld metal was predicted using the Schaeffler diagram. The details of the welding procedure are also displayed. To understand the influence of cooling rate on the transformation temperatures of steel S355J2, dilatometry tests were conducted. To evaluate the adequacy of the filler metals and welding parameters, a series of destructive tests, including tensile and fatigue tests, as well as macroanalysis, microanalysis and microhardness were performed.

3.1 Materials

Dissimilar joints were made between the structural steel S355J2 (EN 10025-2:2004) plate, with a thickness of 12 mm, and the austenitic stainless steel AISI 301LN (EN10088:2-2005) plate, with a thickness of 5 mm. Three different austenitic stainless steel fillers (AWS A5.9 ER307, AWS A5.9 ER308LSi and AWS A5.22 E309LMoT0-1/4) were used. The AWS A5.9 ER307 with 1.00 mm in diameter, the AWS A5.9 ER308LSi with 0.80 mm, and the AWS A5.22 E309LMoT0-1/4 with 1.2 mm. The steel S355J2 was processed by hot rolling. In the steel AISI 301LN, cold rolling was used to obtain a hardness condition of ½ hard.
The chemical compositions of all materials used in this study are in Table 7 and Table 8.

Table 7: Chemical composition of base materials used [85,86].

Elements in %	C	Mn	P	S	Si	Cr	Ni	N
S355 J2	0.09	0.86	0.019	0.004	0.01	-	-	-
AISI 301LN	0.02	1.62	0.034	0.001	0,52	17.37	6.57	0.12

Table 8: Chemical composition of filler materials used [87-89].

Elements in %	C	Mn	P	S	Si	Cr	Ni	N
AWS A5.9 ER307	0.10	7.00	≤ 0.025	≤ 0.025	0.80	19.00	8.50	-
AWS A 5.9 ER308LSi	0.008	1.62	0.018	0.011	0.85	19.87	10.32	0.05
AWS A 5.22 E309LMoT0-1/4	0.02	1.48	0.018	0.003	0.64	23.36	12.80	0.01

Table 8: Chemical composition of filler materials used [87-89] (cont.).

Elements in %	Co	Cu	Mo
AWS A5.9 ER307	-	-	-
AWS A 5.9 ER308LSi	0.04	0.11	0.09
AWS A 5.22 E309LMoT0-1/4	-	0.09	2.15

The mechanical properties of all materials are in Table 9. The CEV of S355J2 is 0.23, indicating good weldability.

Table 9: Mechanical properties of materials used [85-89].

Mechanical properties	Base material		Filler metals		
	S355 J2 EN 10025-2:2004	AISI 301LN EN 10088-2:2005	AWS A 5.9 ER307	AWS A 5.9 ER308LSi	AWS A 5.22 E309LMoT0-1/4
Rp0.2 (MPa)	427	792	390	371	491
Rm (MPa)	526	1041	590 - 685	549	689
A (%)	32	26	35	44	32

To predict the weld microstructure, the Schaeffler method was used [43,61]. The percentage of base metal dilution in GTAW was established to be between 20% and 40% [41]. Considering the two steels used in this work and the filler metal, the Ni_{eq} and Cr_{eq} were calculated (Table 10), and the expected microstructure was predicted, as shown in Figure 23. With AWS A5.9 ER307, a fully austenitic or austenitic with martensite microstructure is expected. With AWS A 5.9 ER308LSi, the microstructure is characterised by the presence of 5% ferrite or its absence in the area with austenite and martensite. With AWS A 5.22 E309LMoT0-1/4, the microstructure is expected to contain approximately 10% ferrite or a mixture of austenite, martensite and ferrite. Therefore, in this specific case where the dilution percentage is unknown, the results show only a range of values.

Table 10: Ni_{eq} and Cr_{eq} for parent metals and filler metals.

	S355 J2 EN 10025-2:2004	AISI 301LN EN 10088-2:2005	AWS A 5.9 ER307	AWS A5.9 ER308LSi	AWS A 5.22 E309LMoT0-1/4
Ni_{eq}	3.13	8.01	15.00	11.37	14.26
Cr_{eq}	0.02	18.15	20.20	21.24	26.47

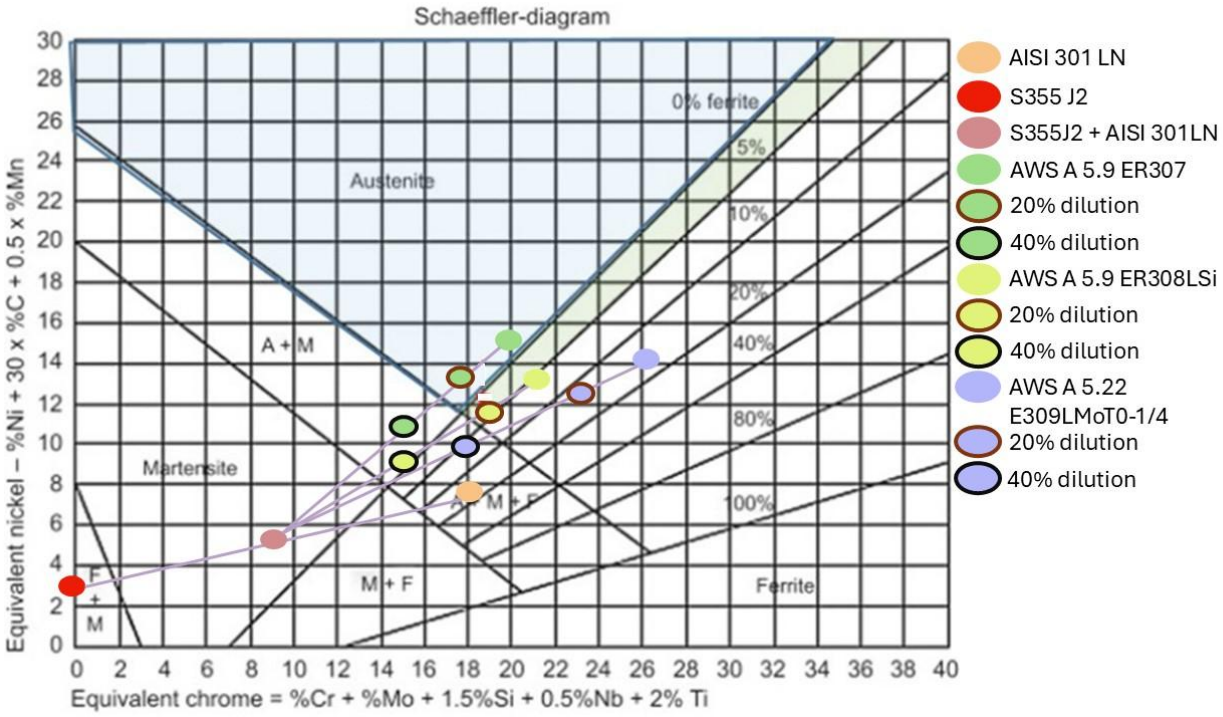


Figure 23: Base image from [70], extra drawing done by the author.

To predict the microstructure of the filler metal, the Ni_{eq} and Cr_{eq} were calculated (Table 11) and applied in the WRC diagram (Figure 24). For AWS A5.9 ER307, the microstructure falls within the ferrite region, with a ferrite content between 4% and 6%. It is also located in the solidification mode FA zone, indicating a transition between skeletal and lathy ferrite. In the case of AWS A5.9 ER308LSi, the ferrite content is about 10%, situated at the boundary of the FA solidification mode. The AWS A5.22 E309LMoT0-1/4 shows a ferrite content of approximately 28%, corresponding to the ferrite solidification mode, which is associated with an acicular/Widmanstätten ferrite morphology.

Table 11: Ni_{eq} and Cr_{eq} of filler metals for WRC Diagrams.

	AWS A 5.9 ER307	AWS A 5.9 ER308LSi	AWS A 5.22 E309LMoT0-1/4
Ni_{eq}	12.00	11.63	13.92
Cr_{eq}	19.00	19.96	25.51

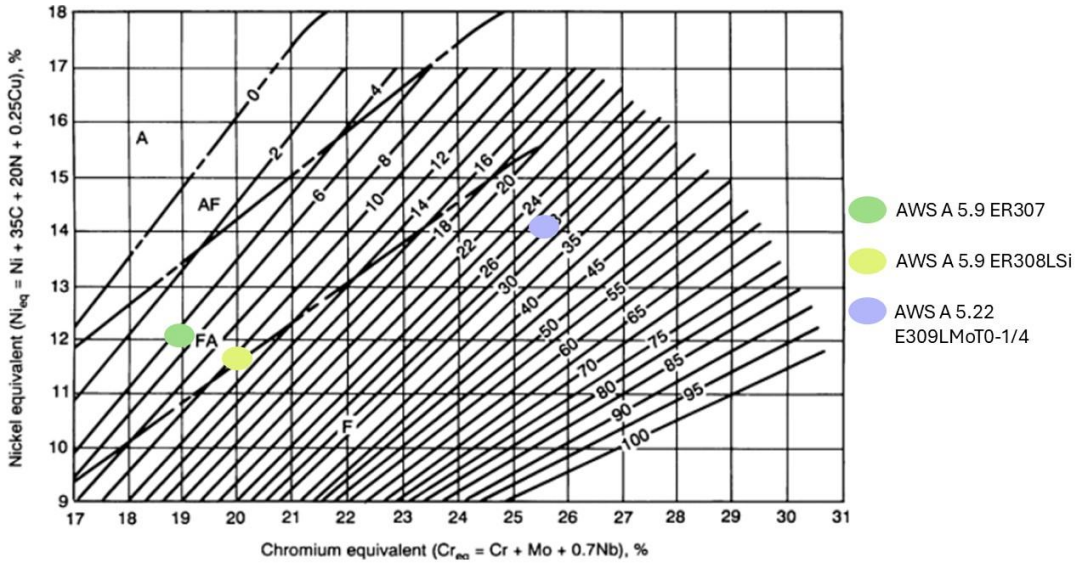


Figure 24: Base diagram from [18], extra drawing done by the author.

3.1.1 Dilatometric Tests

Dilatometric tests allow the determination of the temperatures at which microstructural constituents form during heating, isothermal holding, and cooling. This data is important in processes like welding, essentially for analysing the transformations in HAZ [90]. These tests were done on DIL 805 TA instruments. The conditions are described in Table 12.

Table 12: Conditions of the dilatometric tests [13,91].

Specimen	Starting/Finish Temperature (ºC)	Holding Temperature (ºC)	Heating Rate (ºC/s)	Holding Time (min)	Cooling Rate (ºC/s)
3C	20	1000	4	5	3
10C					10
30C					30
50C					50

The specimens used in dilatometric tests were machined to have dimensions of 4 mm in diameter and 10 mm in length.

3.2 Welding Procedure

The welding process was MAG welding with a joint type of butt weld and steel subgroup 1.2/8.1 [92]. This process was done manually. The joint design used is shown in Figure 25. The shielding gas was ISO 14175-M12 and contained 2% carbon dioxide and 98% helium [93]. The type of current used was DCEP, and the welding position was flat. Two transfer modes were employed: spray and short circuit. The welding sequence is in Figure 26.

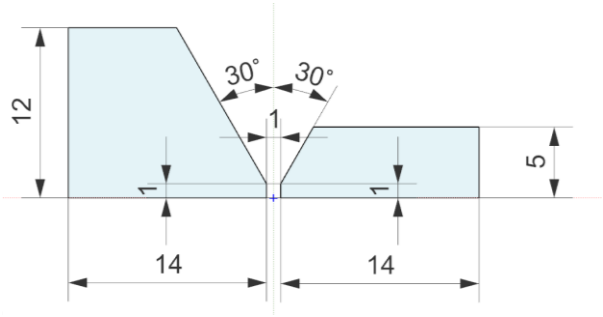


Figure 25: Joint design used [94].

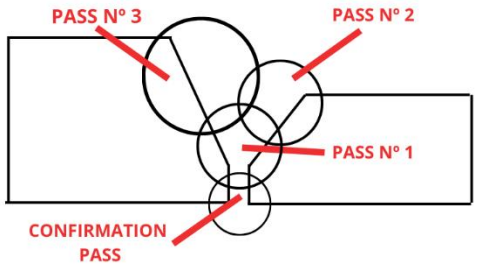


Figure 26: Welding sequence done [94].

The operational parameters stipulated are in Table 13, however the travel speed was not measured [94].

Table 13: Operational parameters [94].

Pass	Current (A)	Voltage (V)	Travel speed (cm/min)	Heat input (kJ/mm)
1	92	18.00	15	0.52
2	147	23.10	29	0.56
3	148	23.00	32	0.52
Confirmation pass	131	22.60	31	0.41

3.3 Mechanical and Microstructural Characterisation

The tests conducted on the base materials and the joint included tensile tests, fatigue tests, hardness tests, and microscopic analysis. The specimens were collected per the standard ISO 15614-1 guidelines, as illustrated in Figure 27.

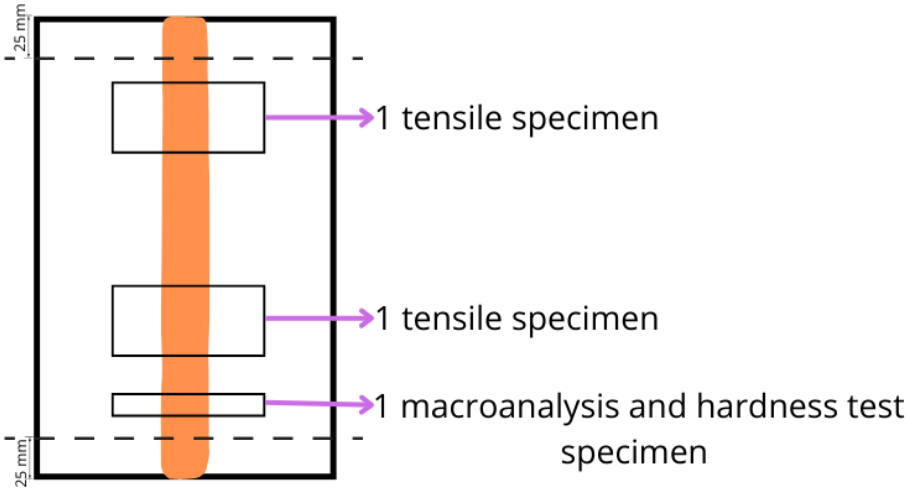


Figure 27: Location of test specimens, adapted from ISO 15614-1.

3.3.1 Tensile Tests

The tensile test specimens of the base material were cut by laser, and the test was conducted according to NP EN ISO 6892-1. For these materials, three of each were tested. The welded tensile test specimens were cut by an electric saw and machined by a CNC machine. For these specimens, the ISO 4136 standard was followed, and two specimens were taken from each joint and tested. The dimensions are presented in Table 14 and Figure 28.

Table 14: Dimensions of tensile test specimens [95-97].

	Base material specimens (mm)	Welded specimens (mm)
G – Gauge length	50.0 ± 0.1	Non specified
W - Width	12.5 ± 1.0	25
T - Thickness	Thickness of material	Thickness of material
R – Radius of fillet	12.5	25
L – Overall length	200	220
A – Length of reduced parallel section	57	70
B – Length of grip section	50	Non specified
C – Width of grip section	20	37

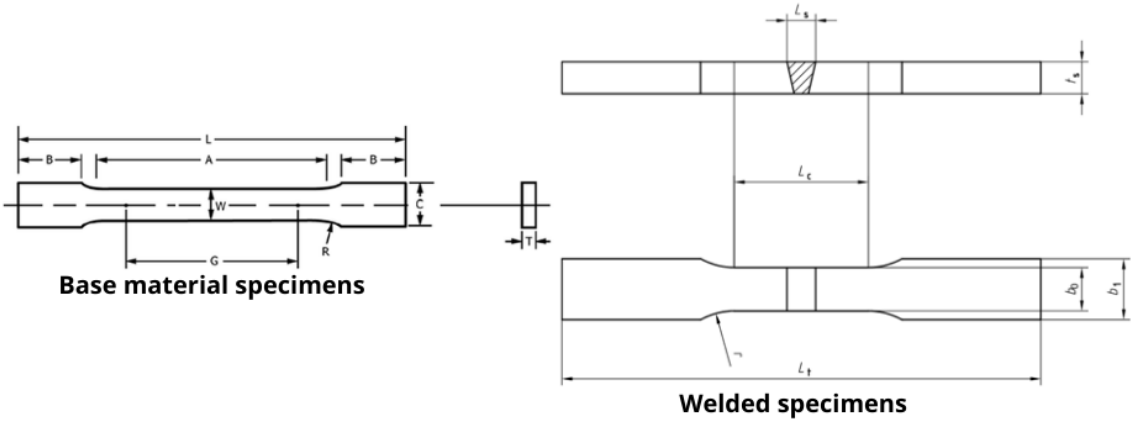


Figure 28: Shape of tensile test specimens [91,93].

The tensile tests were performed using a SHIMADZU Autograph AG-X Plus, with a maximum load capacity of 250 kN and a grip speed of 10 mm/min. Except for the tensile tests on S355J2, which were performed using a SHIMADZU UH X machine with a maximum load capacity of 1000 kN.

3.3.2 Microstructure Analysis

An electric saw cut the portion shown in Figure 27, and an abrasive disc removed transverse-section specimens for macro and microanalysis. Following ISO 17639, defect analysis was performed using unetched macroexaminations, while etched

macroexaminations were employed to evaluate the joint structure. Microexaminations with etching were used to analyse the microstructure [98].
Specimen preparation involved grinding with SiC sandpapers of 180, 320, 400, 600 and 1000 MESH at 300 rpm, followed by polishing using cloths and diamond suspensions of 6 µm and 1 µm at 150 rpm. For the microstructural analysis of stainless steel, aqua regia (a mixture of 15 mL HCl and 5 mL HNO_3) was applied for approximately one minute, yet the results were not satisfactory [99]. Therefore, electrolytic 10% oxalic acid (10 g oxalic acid and 100 mL H_20) was carried out at a current density of 1 A/cm^2 and a voltage of 6 V for 1 minute [100]. For the S355J2, a solution of Nital 4% (100 mL of 96% ethanol and 4 mL of 65% HNO_3) was used for 10 seconds [101]. The welded specimens were etched in parts, meaning the S355J2 joint part was etched with Nital 4%, while the rest was etched with electrolytic oxalic acid under the same conditions as previously mentioned.
To characterise the microstructure of the specimens, a Leica DM4000M microscope equipped with a DMC 2900 camera and the Leica LAS X software was used. Furthermore, a Leica DVM6 Digital Optical Microscope, paired with the Leica Las software, was employed to capture an image of the entire specimen.

3.3.3 Microhardness Test

For all welded joints, Vickers hardness tests were performed using a load of HV 0.1 according to ISO 9015-2. As seen in Figure 29, three rows were done, one aligned with the top weld bead, another aligned with the centre weld bead and one aligned with the root bead, using a regular interval along the row. The equipment used was the FALCON 400 micro/macro-Vickers Hardness Tester (INNOVATEST) with an applied load of 100 gf for 10 seconds.

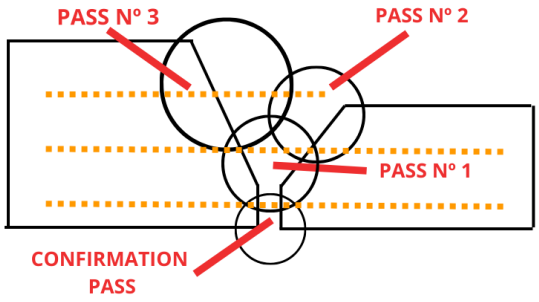


Figure 29: Rows of indentation in welded joints.

3.3.4 Fatigue Tests of AISI 301LN

Ten AISI 301LN specimens were cut using a laser, and followed the standard ISO 1099:2017. The dimensions of these specimens are shown in Table 15 and Figure 30.

Table 15: Dimensions AISI 301LN fatigue test specimens [102].

	Dimensions of Sheet Type (mm)
t - Thickness	Thickness of the material
w - Width	5<w<10
W – length of grip end	≥2w

Lp – parallel length	≥2w
R – transition radius	≥2w

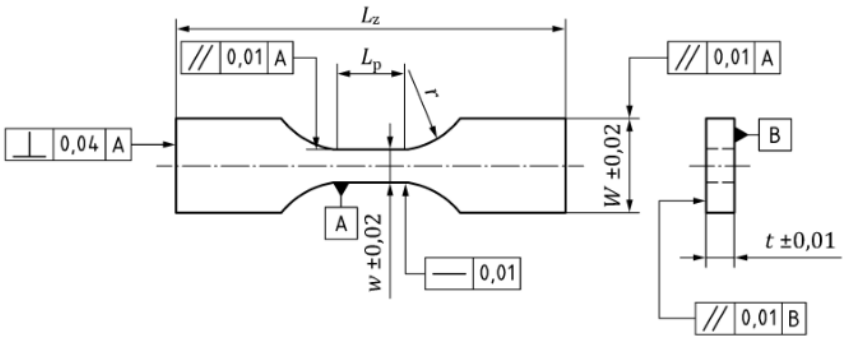


Figure 30: Shape of AISI 301LN fatigue test specimens [102].

These tests were performed using the Instron 8802, with a load cell Instron 2742-501 and a load capacity of 250 kN. After the tests, two specimens were selected to analyse the microstructure in the transverse direction of the thickness, and were removed by cutting with an abrasive disc.

It was established that the stress ratio, R, was 0.05, and the frequency varied between 5 and 15 Hz. The loading stage limited the maximum number of cycles to 5.00×10^6. Different load levels were defined as percentages of yield stress, as seen in Table 16, to establish the S-N data points. All these parameters were established by the technician responsible for carrying out the test.

For this test, the experimental data were fitted following the standard ISO 12107 to obtain the median curve, along with the corresponding coefficient of determination R^2. A reference line for the International Institute of Welding (IIW) steel base material FAT 160, representing fatigue strength at two million cycles, with a slope of m=5, was established [48,103]. A chemical composition analysis of specimens 6 and 8 was performed using a Spectro Lab.

Table 16: % Yield Stress in fatigue specimens of AISI 301LN.

Specimen	% Yield Stress
1	85
2	85
3	80
4	70
5	60
6	50
7	50
8	45
9	45

3.3.5 Fatigue Tests of Welded Specimens

An electric saw cut six welded specimens, followed by a cutting phase performed with a CNC machine to ensure uniform thickness throughout the specimens. The dimensions of these specimens are shown in Figure 31 and were removed in a non-specific zone. Two specimens of each welded joint were evaluated. Specimens without the machining phase were also tested, with a width of 35 mm and a thickness of 5 mm (Figure 32). Three specimens of each joint were tested. Both tests followed ISO 1099.

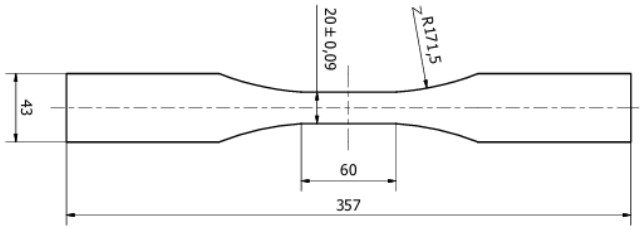


Figure 31: Dimensions of welded fatigue specimens.



Figure 32: Shape of non-machined specimens.

The same machine used for the fatigue tests on AISI 301LN was also used for these tests. A stress ratio R = 0.05 was adopted, with a constant test frequency of 15 Hz. The run-out limit was set to $5.00X10^6$ cycles. The stress levels were defined as 85% of the lowest measured yield stress among the welded joints, in order to establish the S-N data points. For specimens of identical geometry, the same maximum force was applied. However, between machined and non-machined specimens, the maximum applied force differed due to variations in the net cross-sectional area. All these parameters were established by the technician responsible for carrying out the test. A reference line of IIW as-welded condition FAT 112 for machined specimens and FAT 71 for non-machined ones, and with slope m=3, was established [103].

After the tests were completed, one specimen from each joint was analysed, along with an additional specimen of AWS A5.9 ER308LSi. These specimens were analysed using a Leica Zeiss Stemi 2000-C stereo microscope with the LeicaLas X software.

4 RESULTS PRESENTATION AND DISCUSSION

This chapter presents results from the characterisation of both the base materials and the various welded joints. For the base materials, tensile tests were performed. Specifically, dilatometric tests were conducted on steel S355J2, while fatigue tests were performed only on steel AISI 301LN. In the welded joints, microstructural and macrostructural characterisation was conducted, together with microhardness, tensile and fatigue tests. These last tests were performed on both machined and non-machined specimens.

4.1 Dilatometric tests of S355J2

The transformation temperatures, on heating, are identical across all tests due to the constant heating rate. In contrast, the different cooling rates result in distinct transformation temperatures and corresponding phases, as seen in Table 17.

Table 17: Transformation Temperatures of the steel S355J2.

Specimen	Heating Rate (ºC/s)	Transformation temperatures - Heating (ºC)		Cooling Rate (ºC/s)	Transformation temperatures - Cooling (ºC)	
		A_{C1}	A_{C3}		A_{R3}	A_{R1}
3C	4	735.25	851.02	3	698.27	620.79
10C		735.33	838.20	10	643.42	524.57
30C		727.48	837.37	30	621.82	379.47
50C		718.58	806.05	50	436.46	341.40

The cooling rates of 3 ºC/s and 10 ºC/s are sufficiently slow to allow diffusion-controlled transformation to occur (austenite → ferrite and austenite → perlite). This is consistent with the ferrite and perlite microstructure formed, as shown in Figure 33 a). For the 10 ºC/s cooling rate, a Widmanstädtten microstructure is formed, in which pearlite grows, as seen in Figure 33 b). A 30 ºC/s cooling rate results in bainite and martensite formation, which can be seen in Figure 33 c). A cooling rate of 50 ºC/s leads to the formation of a microstructure with a higher martensite fraction, as observed in Figure 33 d).
These results indicate that, depending on the cooling rate resulting from welding, different phases are formed, which influence the final mechanical properties and potential defects, particularly the susceptibility to cold cracking, since the formation of martensite increases this susceptibility.

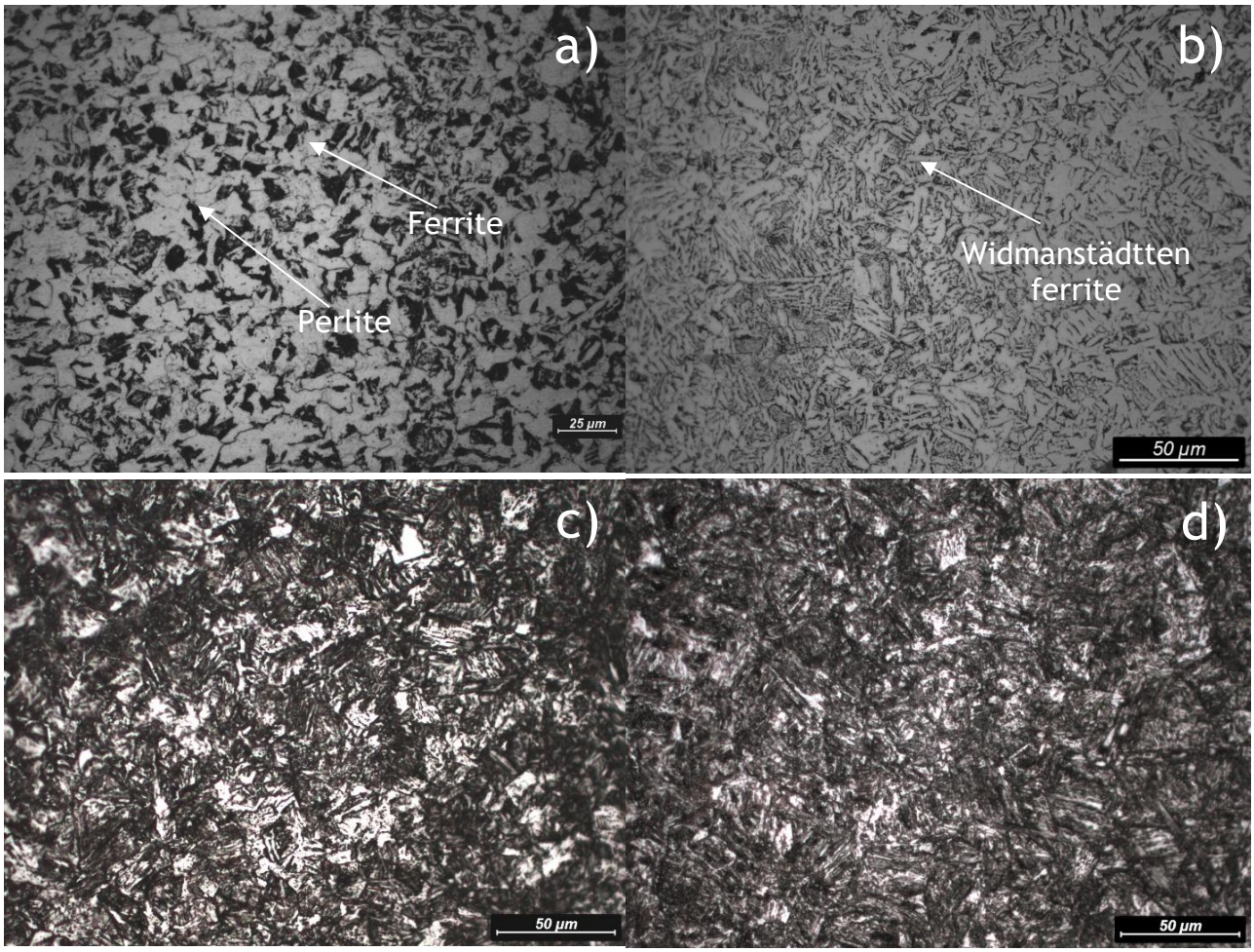


Figure 33: Microstructure results of dilatometric tests with: a) 3 ºC/s cooling rate; b) 10 ºC/s cooling rate; c) 30 ºC/s cooling rate; d) 50 ºC/s cooling rate.

4.2 Mechanical Properties of Base Materials

4.2.1 Tensile Tests of Base Materials

All specimens tested fractured in the middle of the gauge length. As shown in Table 18, the steel AISI 301LN exhibits a high level of consistency in elongation values, whereas its strength shows greater variability. On the other hand, in the steel S355J2, the standard deviation is slight across all properties. These results demonstrate that the differences between the specimens' results and the certificate data are minimal, as well as the compliance of both materials with the respective standards. Additional details on the tensile properties can be found in Annexe A.

Table 18: Tensile test values of base materials.

Mechanical properties	Steel AISI 301LN	Difference from the certified value (%) - AISI 301LN	Steel S355J2	Difference from the certified value (%) - S355J2
Rm (MPa)	1015.5 ± 12.8	2.5	495.3 ± 0.6	|-6.0|
Rp 0.2 (MPa)	801.4 ± 16.9	|-1.1|	414.0 ± 3.0	|-3.0|
A (%)	27.1 ± 0.0	|-4.2|	27.0 ± 0.8	|-16.0|

4.2.2 Fatigue Tests of AISI 301LN

Fatigue tests on AISI 301LN steel were conducted because the structure of a railway vehicle is primarily composed of this steel, and it was essential to evaluate its fatigue behaviour. As stated before, different load levels, defined as percentages of the previously determined yield stress of AISI 301LN (792 MPa), were applied to obtain S-N data points. The S-N curve in Figure 34 reveals an expected trend: as the stress amplitude decreases, the number of cycles to failure increases.

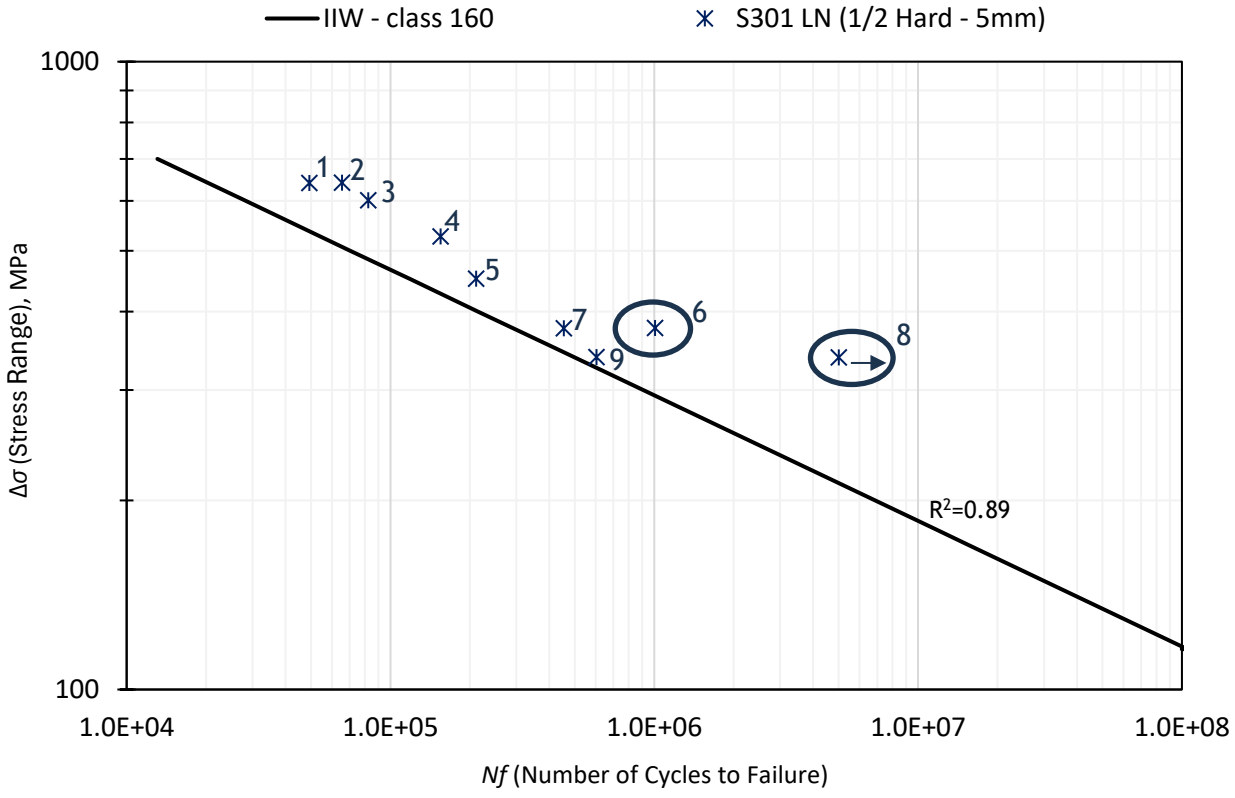


Figure 34: S-N curve of AISI 301LN.

One of the specimens with a lower stress range, specimen 8, did not fracture until the 5.00×10^6 cycles, and thus it was considered a run-out, as shown in Table 19 and indicated by a right-facing arrow in Figure 34. An R^2 value of 0.89 indicates a strong fit of the

regression model, as it is close to 1. When compared to the IIW line, the experimental data lie consistently above it, indicating higher fatigue resistance than the base design category.

Table 19: Fatigue results of AISI 301LN.

Specimen	Stress Range (MPa)	Nf (cycles)
1	320.47	$4.91x10^4$
2	320.93	$6.55x10^4$
3	300.96	$8.24x10^4$
4	263.34	$1.55x10^5$
5	225.72	$2.11x10^5$
6	188.21	$1.01x10^6$
7	188.09	$4.53x10^5$
8 (run-out)	169.14	$5.00x10^6$
9	169.30	$6.03x10^5$

Based on this information, two specimens, indicated in Figure 34, were selected to investigate differences in microstructure to understand how similar stress amplitudes could result in a significant difference in the number of cycles to failure. The specimen with the higher number of cycles, specimen 8, exhibits a homogeneous microstructure mainly composed of austenitic grains, martensite and precipitates (Figure 35). While the other specimen, specimen 6, contains a region of deformation-induced martensite, as shown in Figure 36 a), in addition to the microstructure composed of austenite grains and martensite, as seen in Figure 36 b), which may have promoted the initiation of fracture.

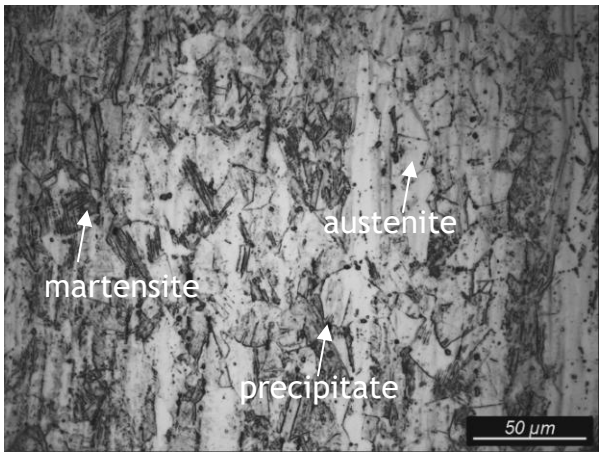


Figure 35: Microstructure of specimen 8.

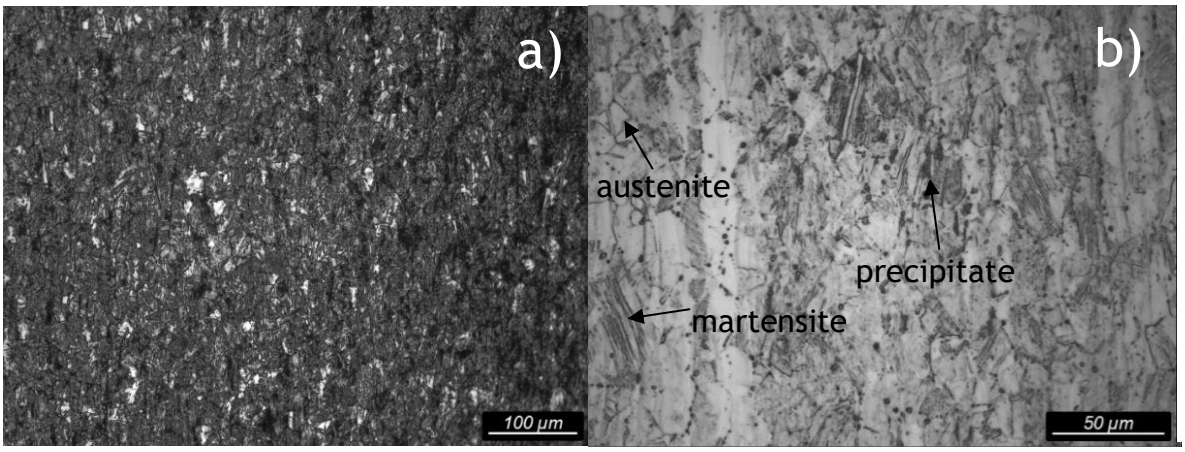


Figure 36: Microstructures of specimen 6: a) Martensite; b) Austenitic grains with martensite.

To understand this difference, a hypothesis was proposed that there might be chemical heterogeneity between the specimens, since a higher percentage of austenite-stabilising elements, particularly nickel, would prevent the transformation of austenite into martensite. However, the spectrometric analysis carried out (Table 20) showed no significant difference between the two specimens. The most likely reason for these results is probably heterogeneity in the deformation introduced during the cold rolling process.

Table 20: Spectrometry results for specimens 6 and 8 of the fatigue test.

	C (%)	Mn (%)	P (%)	S (%)	Si (%)	Cr (%)	Ni (%)	N (%)
Specimen 6	0.02	1.61	0.034	<0.0004	0.42	17.38	6.62	0.18
Specimen 8	0.03	1.59	0.033	<0.0004	0.43	17.34	6.60	0.17

4.3 Welding Specimen's Characterisation

4.3.1 Welding with Filler AWS A5.9 ER307: 4-6% ferrite in WRC diagram

4.3.1.1 Microstructure

Figure 37 shows the macrostructure of the welded joint, with no defects observed.

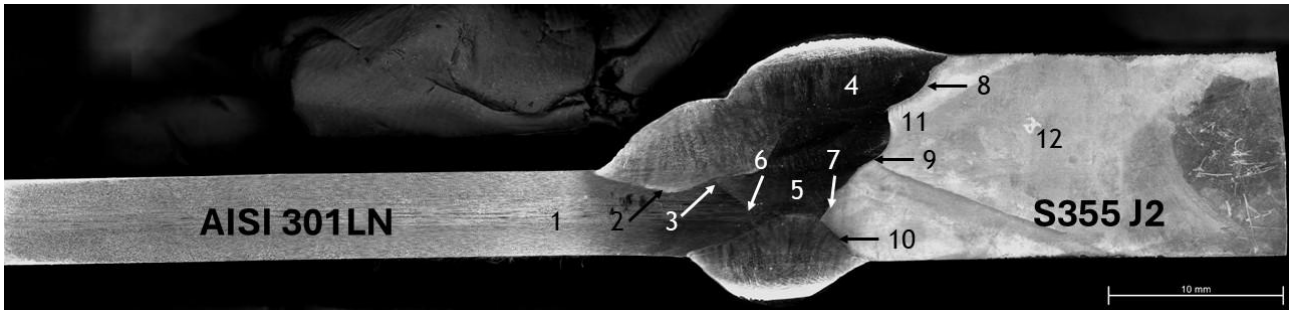


Figure 37: Macrostructure of welded joint with filler metal AWS A5.9 ER307.

The microstructure of the various zones in the dissimilar weld joint, Filler Metal region (FM), HAZ (on both sides), and the Base Material region (BM), are analysed below.
Between the BM 1, Figure 38 a), and HAZ 2, in Figure 38 b) and Figure 38 c), a reduction

of the grain size is observed, which can be a result of the austenite recrystallisation due to the heat imposed in this region, as shown in the reference [60]. Also in BM 1, small precipitates, possibly chromium carbides, are observed in the austenitic grains. These precipitates are also observed along the grain boundaries in the HAZ (position 2), consistent with findings reported in other studies [23].

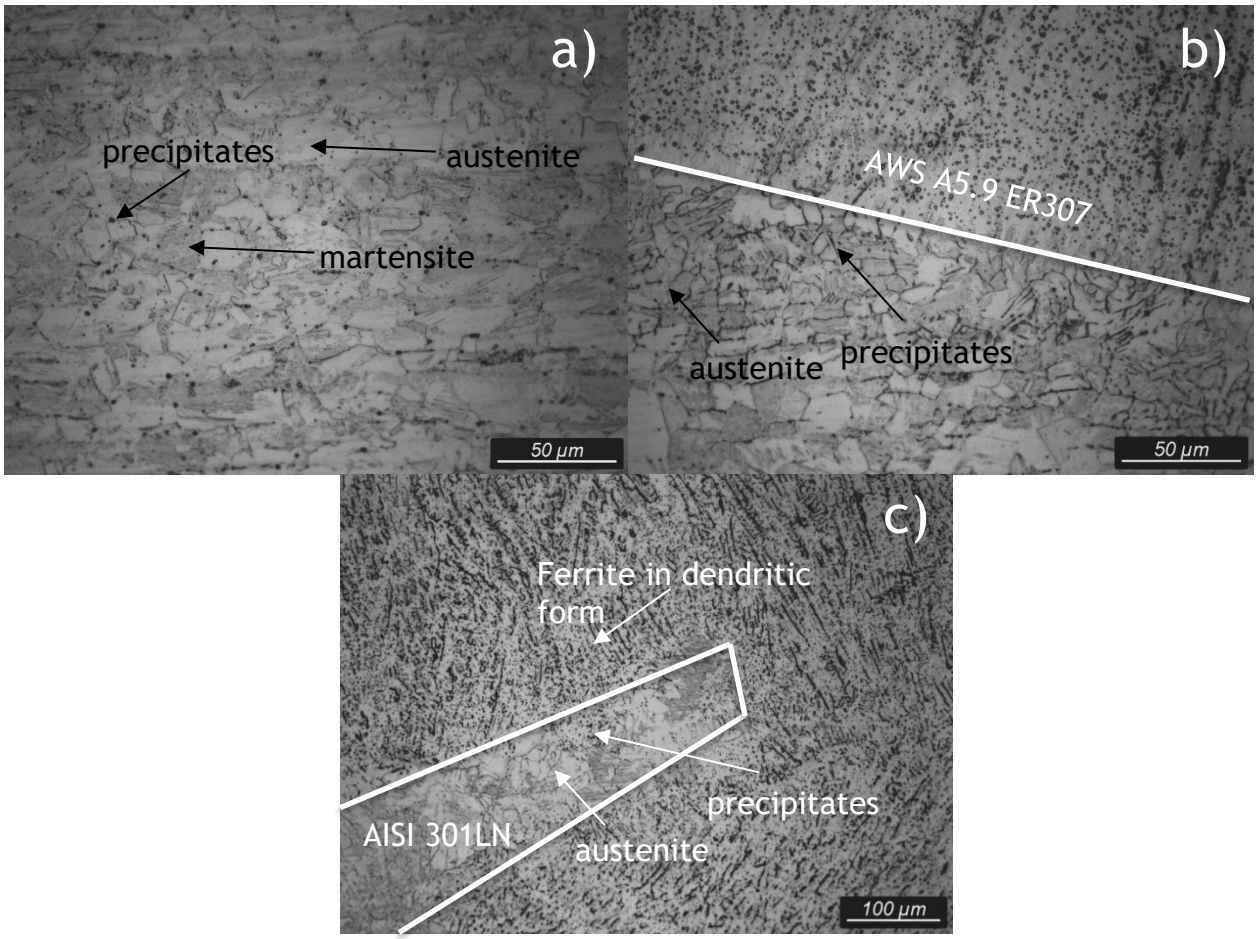


Figure 38: Microstructure of: a) BM AISI 301LN (position 1); b) HAZ and FM upper weld pass (position 2); c) HAZ between upper and centre weld pass (position 3).

The delta ferrite is observed in FM (positions 4 and 5), as shown in Figure 39 a) and Figure 39 b), with skeletal and lathy morphologies, as referred in other studies [23]. In FM 6 and 7, Figure 39 c) and Figure 39 d), the microstructure is significantly finer and has a dendritic form, as observed in other works [104]. In FM 6, a higher fraction of precipitates is observed, possibly due to the diffusion of carbon from steel S355J2 and the formation of chromium carbides. This microstructure is consistent with the WRC diagram, which predicts a lathy and skeletal ferrite morphology.

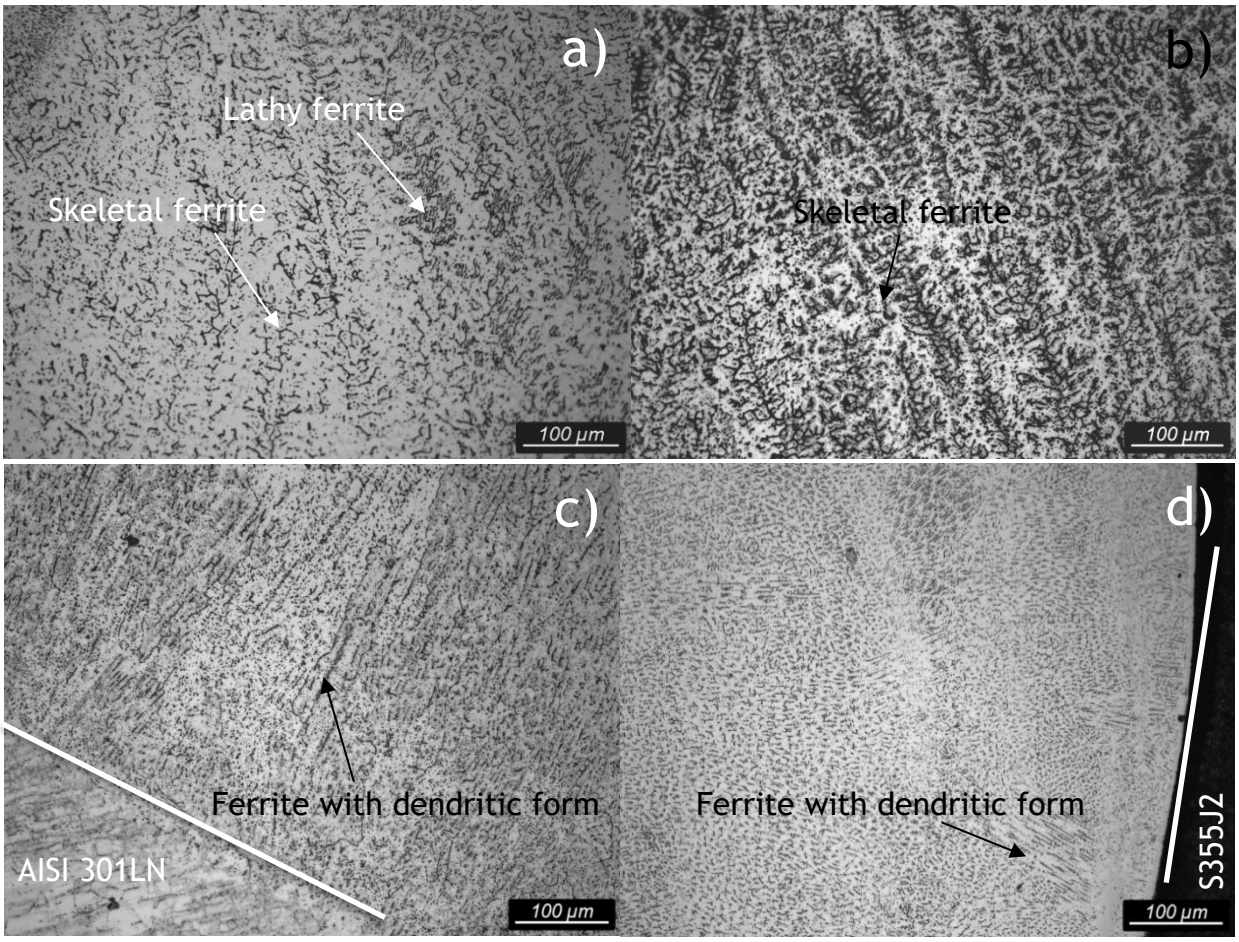


Figure 39: Microstructure of: a) upper right pass (position 4); b) centre weld pass (position 5); c) HAZ (position 6); d) HAZ (position 7).

In the HAZ (positions 8, 9, and 10), Widmanstätten ferrite is observed throughout all welding passes, seen in Figure 40 a), b) and c), but in the upper and lower welding passes, it seems to have a higher quantity visually. One hypothesis is that the upper and lower passes in the HAZ 8 and 10 experience a higher cooling rate than the centre pass, leading to a higher fraction of Widmanstätten ferrite, as the cooling rate plays a key role in its formation, also verified by the dilatometric tests conducted previously [105]. This could be due to a change in current or travel speed during welding, which reduced the heat input and promoted the formation of this microstructure. Therefore, a higher travel speed could explain this difference, as travel speed was not a controlled parameter.

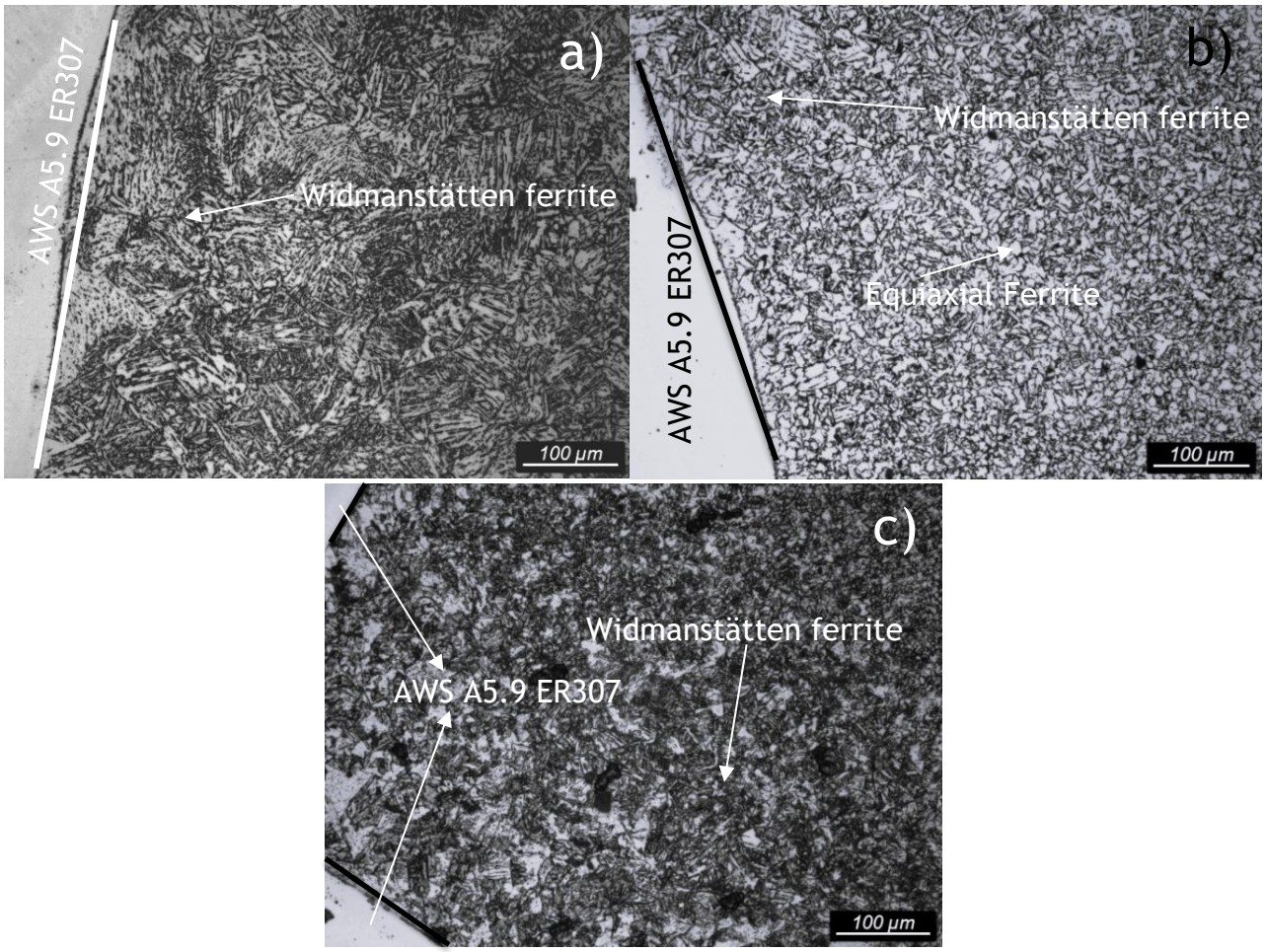


Figure 40: Microstructure of: a) HAZ with upper weld pass (position 8); b) HAZ with centre weld pass (position 9); c) HAZ with lower weld pass (position 10).

In S355J2, the FCHAZ (HAZ position 11), observed in Figure 41 a), can be identified due to the lower grain size, visually compared with the size of BM 12 in Figure 41 b). A ferritic matrix with perlite islands forms both microstructures. The difference lies in the base material, where the grains are elongated due to the rolling process.

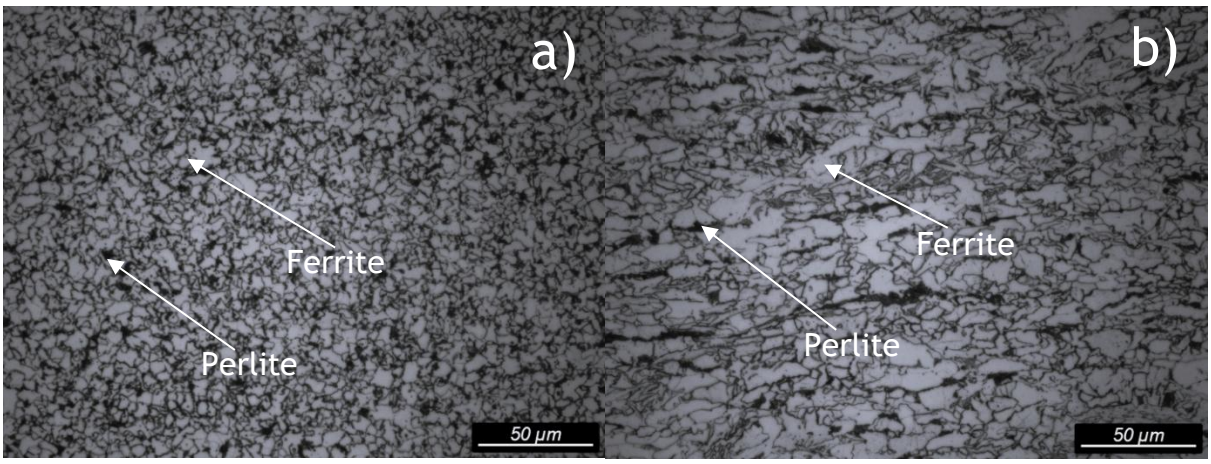


Figure 41: Microstructure of: a) HAZ (position 11); b) BM S355J2 (position 12).

4.3.2 Welding with Filler AWS A 5.9 ER308LSi: 10% ferrite in WRC Diagram

4.3.2.1 Microstructure

The macrostructure of the welded joint is shown in Figure 42. Some defects, highlighted in red, appear likely to be caused by a lack of fusion, and if this is the case, a higher current should have been applied.

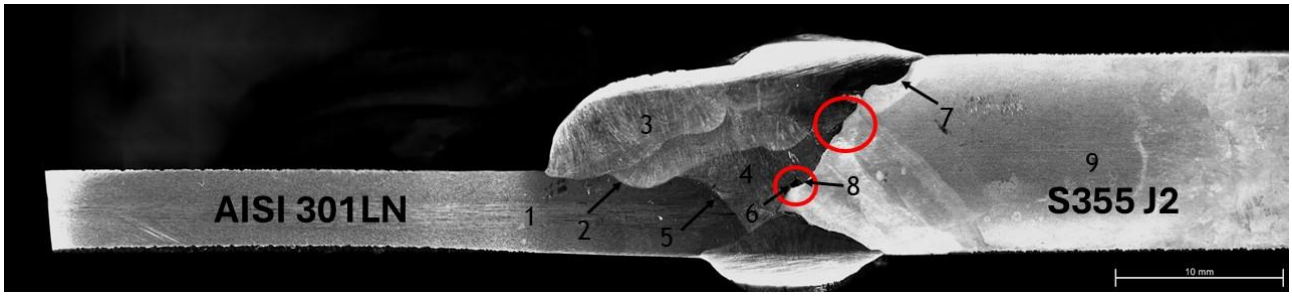


Figure 42: Macrostructure of welded joint with filler metal AWS A5.9 ER308LSi.

As stated in the previous microstructure analysis, the microstructure of the dissimilar joint is inhomogeneous. It can be divided into the FM region, the HAZ on both sides and the BM region.

The BM 1 contains both martensite and austenitic grains along with some precipitates, probably carbide precipitates, indicated in Figure 43 a). In the HAZ 2, in Figure 43 b), a decrease in grain size is observed due to austenite recrystallisation that occurred during the welding process, and martensite is present in a lower fraction. In this zone, precipitates are observed in the grain boundaries of austenitic grains, supposedly chromium carbides. The FM (positions 3 and 4) has, once again, delta ferrite seen in Figure 43 c) and Figure 43 d). Differing from the previous weld metal microstructure, this one has more ferrite with lathy morphology, as an addition to the skeletal morphology, probably due to the higher Cr_{eq} to Ni_{eq} ratio (1.87) in the Schaeffler diagram, compared to the previous filler metal (1.35), which creates this morphology (Figure 13). As this microstructure is ferrite and aligned with the Schaeffler diagram, it can be deduced that the percentage of dilution of the base material has to be near 20%, since after that value, martensite would be formed. This microstructure is also consistent with the WRC diagram, which predicts a lathy and skeletal ferrite morphology, with an emphasis on more lathy morphology.

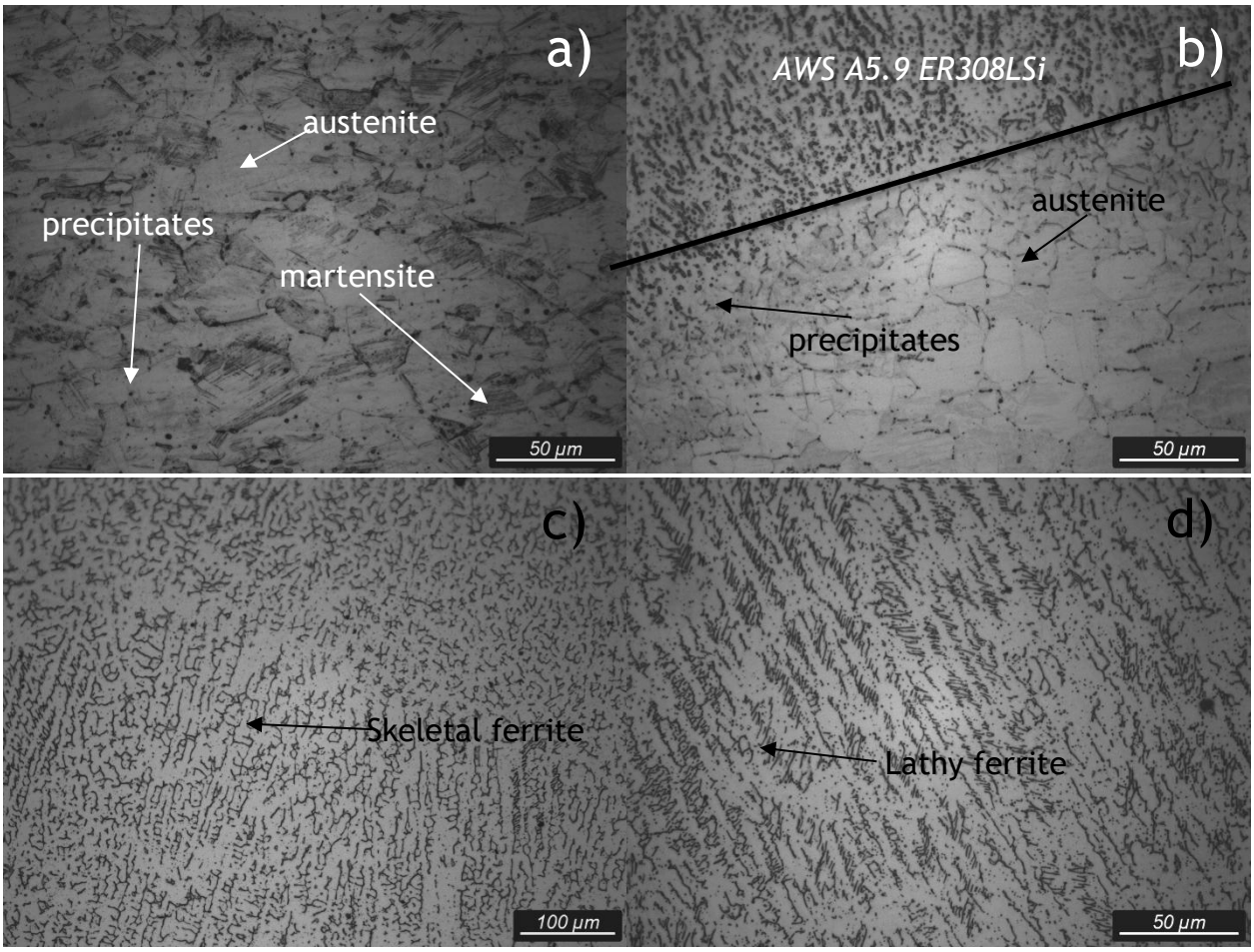


Figure 43: Microstructure of: a) BM AISI 301LN (position 1); b) HAZ with upper weld pass (position 2); c) upper left pass in FM (position 3); d) centre weld pass in FM (position 4).

Analysing the microstructure evaluation in the fusion line of the FM (positions 5 and 6), both sides have a finer microstructure. In the FM 5, this steel is in the direction of the dendritic ferrite. From Figure 44 a), a vertical transition can be observed from skeletal ferrite to dendrite form. There are darker regions due to precipitates. From the FM 6, in Figure 44 b), almost all microstructure is in dendrite form and finer than the previous one, but also exhibits some skeletal and lathy morphologies.

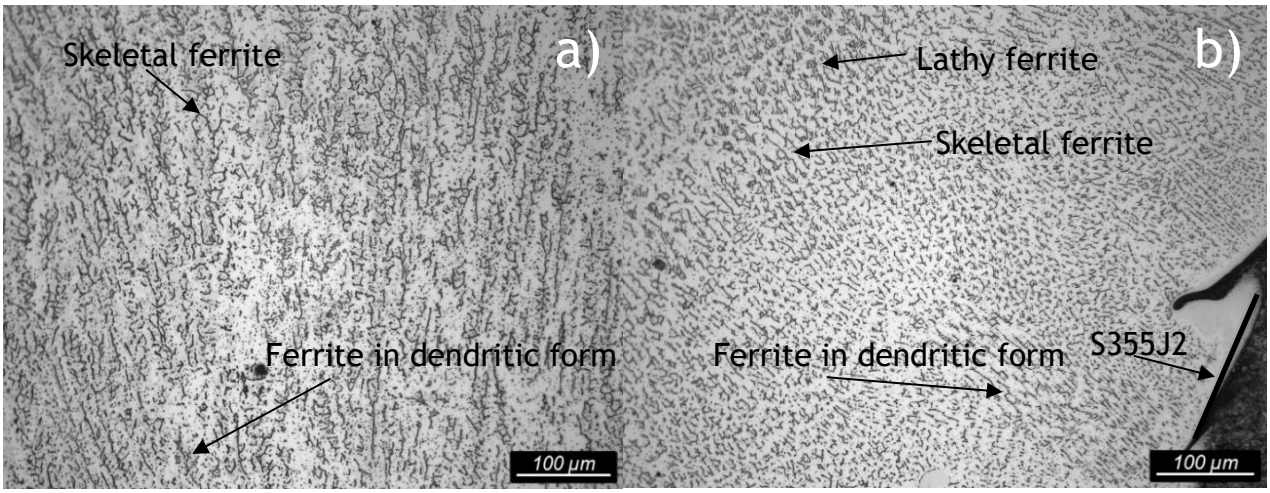


Figure 44: Microstructure of FM: a) position 5; b) position 6.

A Widmanstätten ferrite is present in the HAZ 7 and 8, as seen in Figure 45 a) and Figure 45 b). This is explained in the same way as the previous joint. In the BM 9, a ferrite and perlite microstructure is observed, with elongated grains, in Figure 45 c).

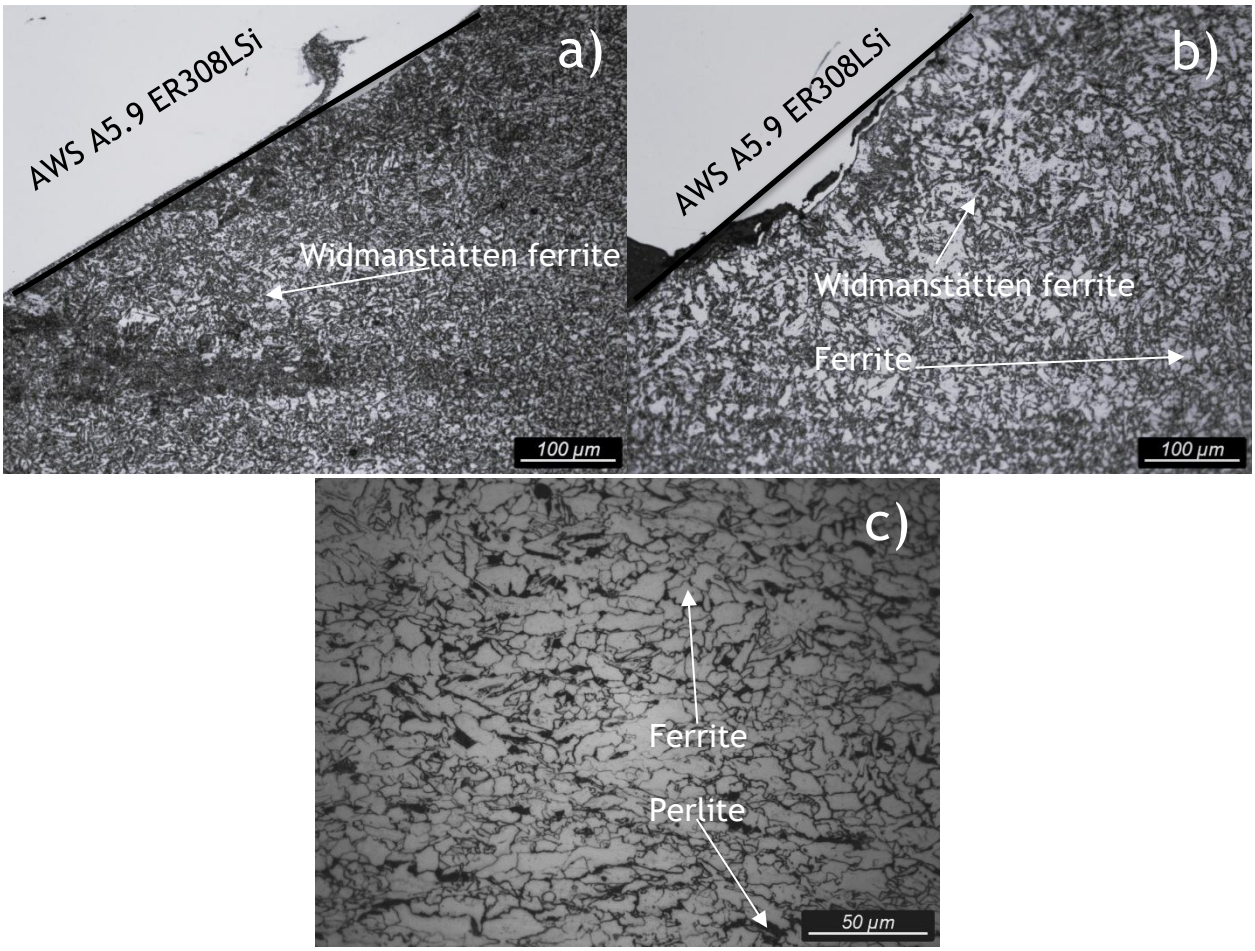


Figure 45: Microstructure of: a) HAZ with upper weld pass (position 7); b) HAZ with centre weld pass (position 8); c) BM S355J2 (position 9).

4.3.3 Welding with Filler AWS A5.22 E309LMoT0-1/4: 28% ferrite in WRC Diagram

4.3.3.1 Microstructure

In the macrostructure (Figure 46), it is noted that the misalignment of the stainless steel is likely due to the plate not being properly fixed.

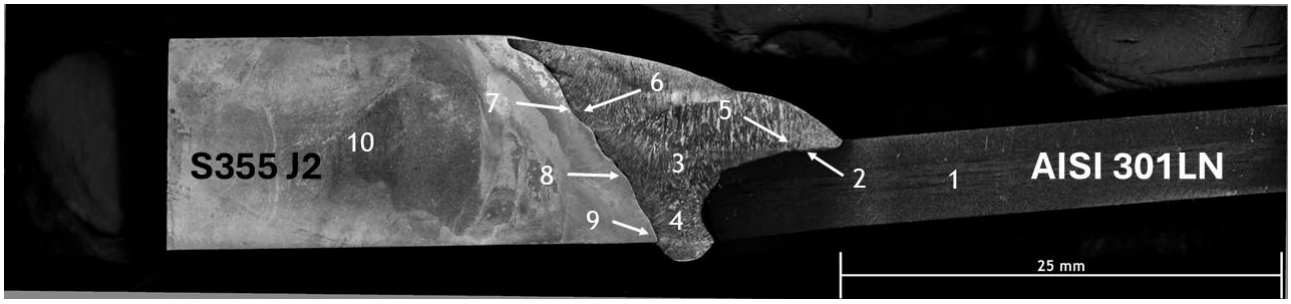


Figure 46: Macrostructure of welded joint with filler metal AWS A5.9 ER309LMoT0-1/4.

The microstructure of BM 1 and HAZ 2, as shown in Figure 47 a) and Figure 47 b), is similar to previous joints. In the FM 3 and 4, as displayed in Figure 47 c) and Figure 47 d), the presence of Widmanstätten ferrite, resulting from the higher Ni_{eq} and Cr_{eq} of the filler metal, and as predicted in the WRC diagram, is observed. According to the Schaeffler diagram, the percentage of ferrite should be between 20% and 50%. In the FM 5 and 6, as seen in Figure 48 a) and Figure 48 b), this morphology is maintained.

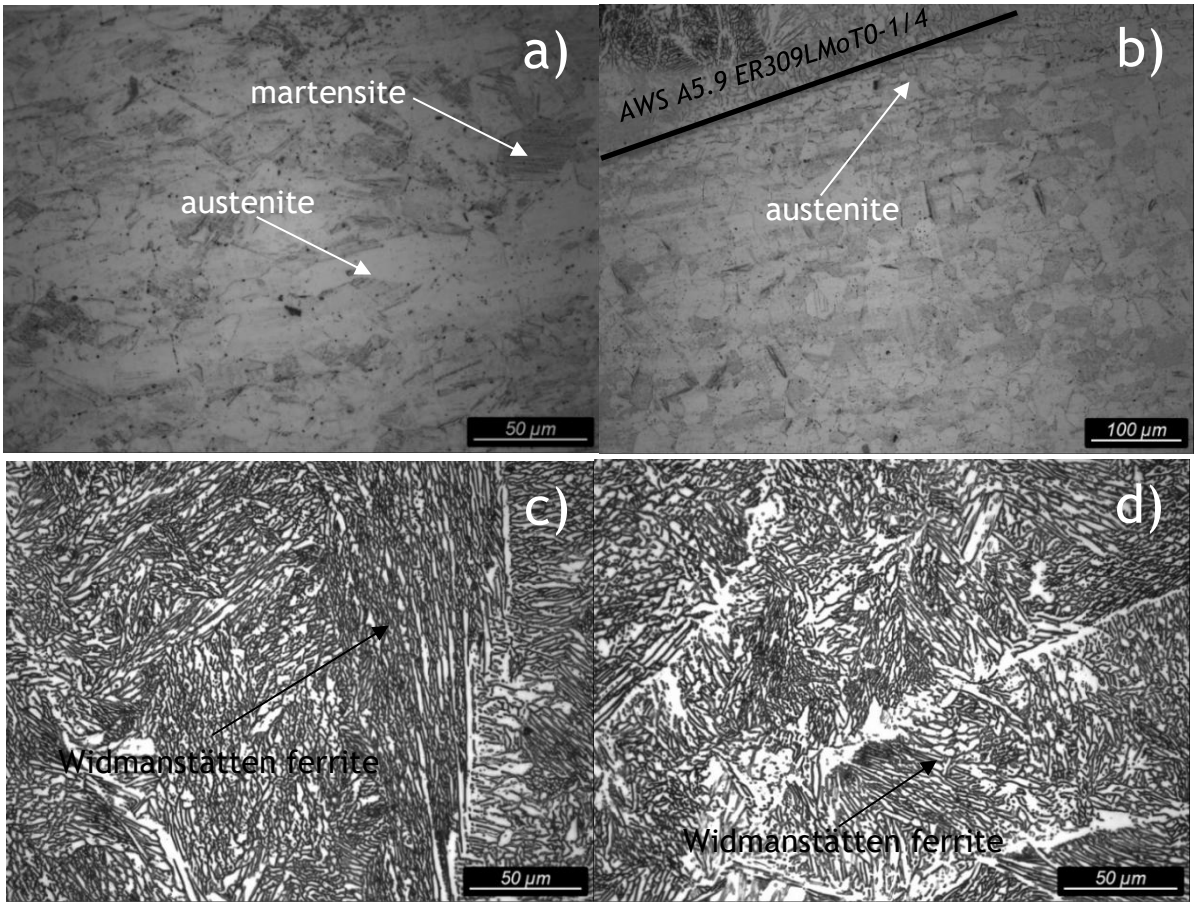


Figure 47: Microstructure of: a) AISI 301LN (location 1); b) HAZ of AISI 301LN with upper pass (location 2); c) centre weld pass of FM (location 3); d) lower weld pass of FM (location 4).

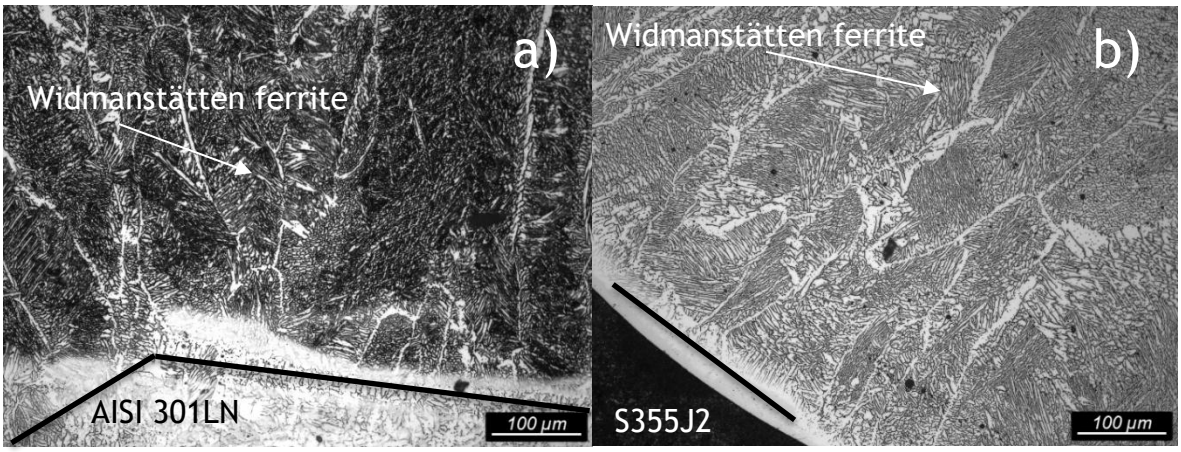


Figure 48: Microstructure of: a) weld metal in HAZ of AISI 301LN (location 5); b) weld metal in HAZ of S355J2 (location 6).

In the HAZ of 7, 8 and 9, in Figure 49 a), Figure 49 b) and Figure 49 c), the Widmanstätten

ferrite is present as well as equiaxial ferrite. In this joint, the morphology is less visually prevalent than in the previous one. The BM 10 in Figure 49 d) does not show perlite bands, and the perlite fraction is much lower, suggesting that the chemical composition of this steel plate differs from the previous ones.

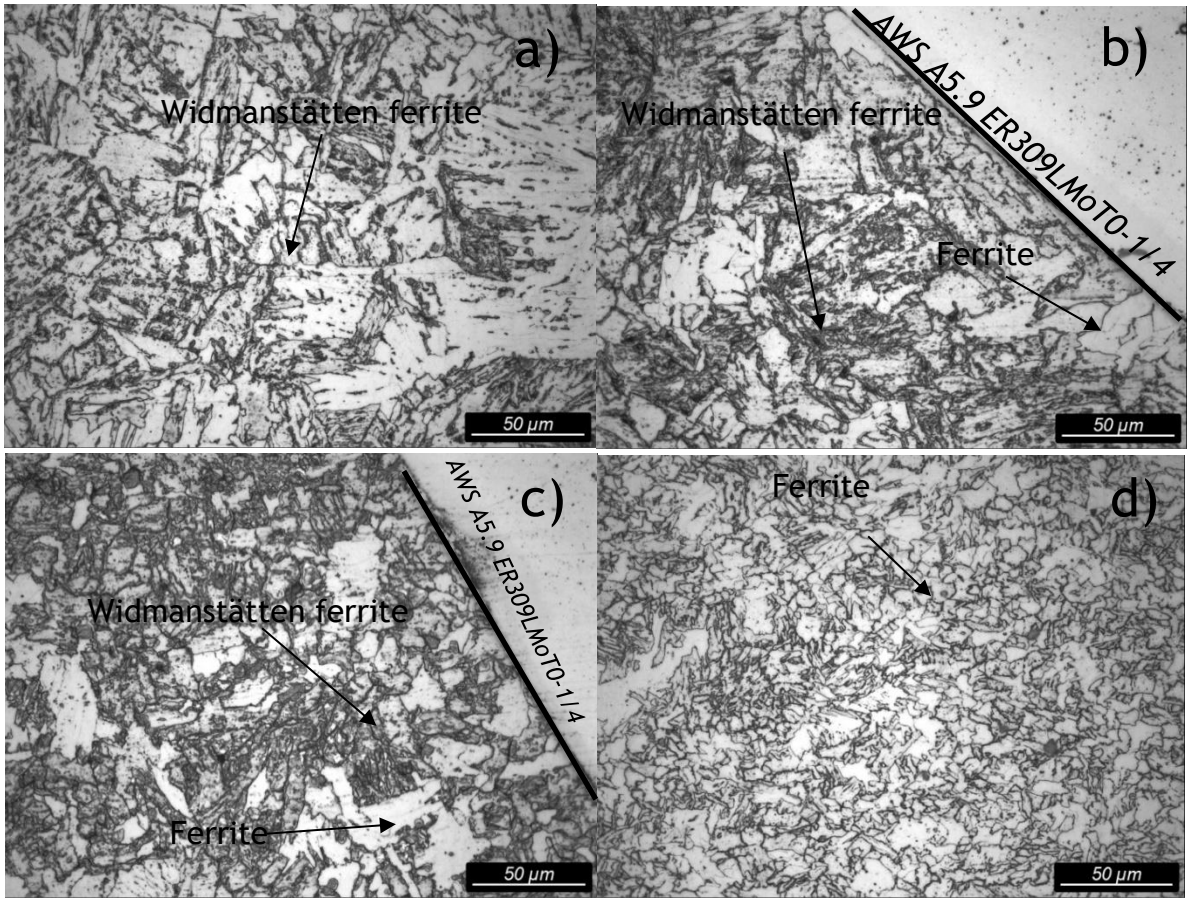


Figure 49: Microstructure of: a) HAZ of S355J2 with upper weld pass (location 7); b) HAZ of S355J2 with centre weld pass (location 8); c) HAZ of S355J2 with lower weld pass (location 9); d) S355J2 (location 10).

4.3.4 Microhardness Test of Welded Joints

The hardness profiles across the weld joint interface are shown in Figure 50, Figure 52 and Figure 54. On the AISI 301LN side, the hardness ranges between 350 HV and 400 HV, showing a decrease in hardness in the HAZ toward the weld metal zone (around the zero point). This may be due to austenite recrystallisation, which reduces the martensite fraction and consequently lowers the hardness. However, in the root and centre bead, there are peak values (439 and 469 HV in joint with AWS A5.9 ER307; 409 and 410 HV in joint with AWS A5.22 E309LMoT0-1/4) associated with a region with martensite on the BM. On the S355J2 side, the hardness is more homogeneous, although slightly higher values are found in the HAZ. This tendency is similar through all joints, but the joint with AWS A5.9 ER307 is the most inhomogeneous. Figure 51, Figure 53 and Figure 55 illustrate the hardness profiles obtained in each joint.

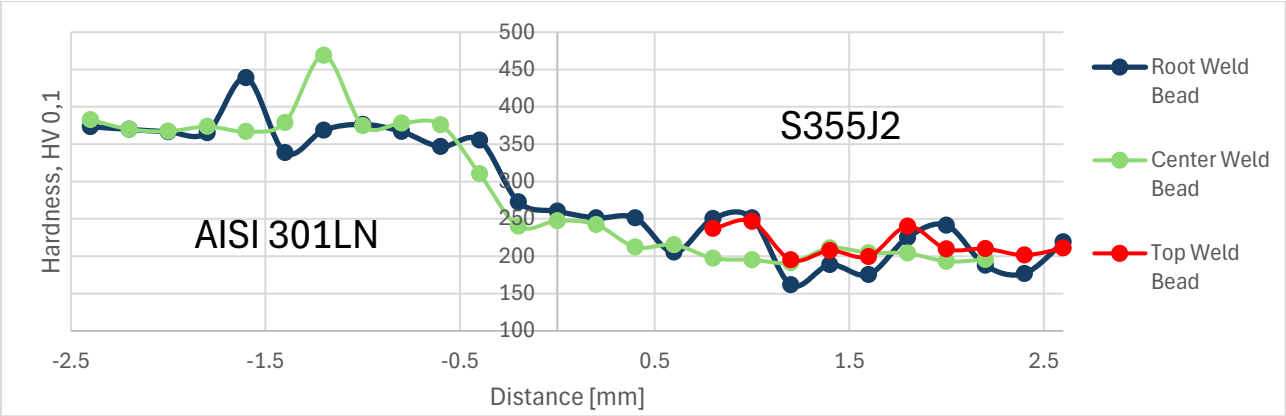


Figure 50: Microhardness profile of the welded joint with filler metal AWS A5.9 ER307.



Figure 51: Macrostructure of welded joint with filler metal AWS A5.9 ER307, with the hardness profile illustrated.

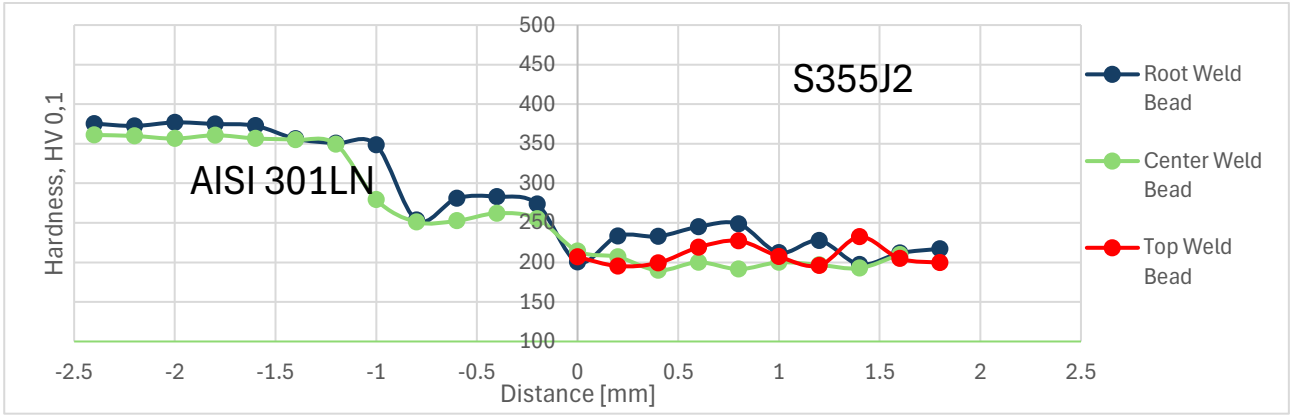


Figure 52: Microhardness of welded joint with filler metal AWS A5.9 ER308LSi.

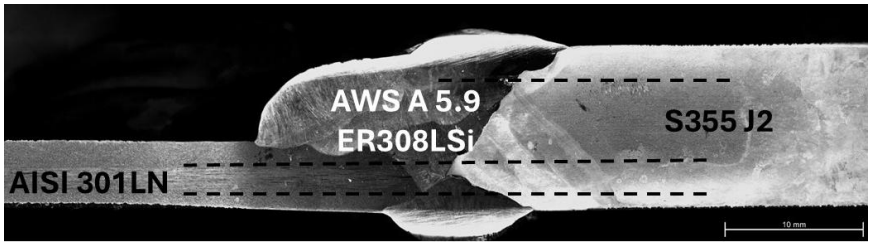


Figure 53: Macrostructure of welded joint with filler metal AWS A5.9 ER308LSi, with the hardness profile illustrated.

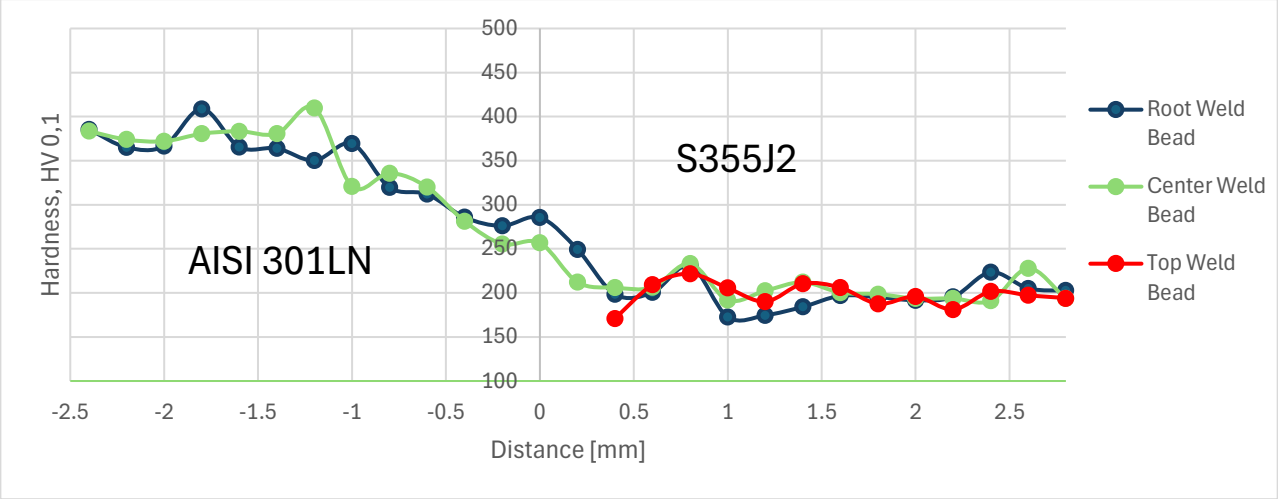


Figure 54: Microhardness of welded joint with filler metal AWS A5.22 E309LMoT0-1/4.

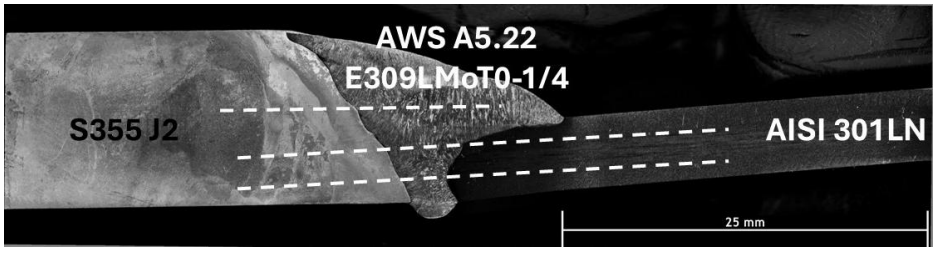


Figure 55: Macrostructure of welded joint with filler metal AWS A5.22 E309LMoT0-1/4, with the hardness profile illustrated.

4.3.5 Tensile Tests of Welded Joints

All the tensile test results are in Table 21. More details of the tensile test results are in Annexe B. All specimens fractured on the side with lower resistance, the S355J2 steel (Figure 56). This suggests that the welding process was well-executed, and, in terms of mechanical strength, all the joints showed satisfactory performance. The joint with AWS A5.22 E309LMoT01/4 presented lower tensile and yield strength because the perlite fraction in the S355J2 steel was lower.

Table 21: Tensile test results of the welded joints.

Mechanical properties	Weld joint with filler AWS A5.9 ER307	Weld joint with filler AWS A5.9 ER308LSi	Weld joint with filler AWS A5.22 E309LMoT0-1/4
Rm (MPa)	550.1 ± 8.6	550.0 ± 5.5	498.5 ± 1.1
Rp 0.2 (MPa)	452.3 ± 10.1	465.2 ± 4.7	428.9 ± 4.8
A (%)	15.8 ± 0.0	14.4 ± 0.0	15.0 ± 0.0
Fracture location	S355J2 steel side		



Figure 56: Tensile specimens of the dissimilar joints fracture.

4.3.6 Fatigue Test of Welded Joints

As described in the Materials and Methods chapter, fatigue tests were conducted on machined welded joint specimens with the applied stress at 85% of the lowest yield stress of the welded joint specimens (429 MPa), as determined from the tensile test. The results are shown as detailed data in Table 22 and in graphical form in Figure 57.

All specimens fractured in the HAZ of AISI 301LN due to the presence of precipitates along the grain boundaries, which likely promoted crack initiation. The welded joints with AWS A5.9 ER307 have superior fatigue performance compared with the other two filler metals. However, these specimens exhibit only 11% and 16% of the maximum cycles established previously ($5X10^6$). Compared to the line IIW FAT 112, the specimen ER308-02 fell within the expected number of cycles in that stress range, while the others exceeded this expectation. Therefore, if only these three options are available, AWS 5.9 ER307 is the most suitable choice due to a much higher number of cycles. Still, for a structural application like this, further testing and experimentation would be necessary to determine whether other filler metals might offer even better performance.

Table 22: Fatigue results for machined specimens.

Specimen	Stress Range (MPa)	Nf (cycles)
ER307-01	346.09	$5.69X10^5$
ER307-02	346.35	$8.00X10^5$
ER308-01	346.38	$1.62X10^5$
ER308-02	346.00	$6.77X10^4$
ER309-01	346.27	$1.11X10^5$
ER309-02	346.65	$1.22X10^5$

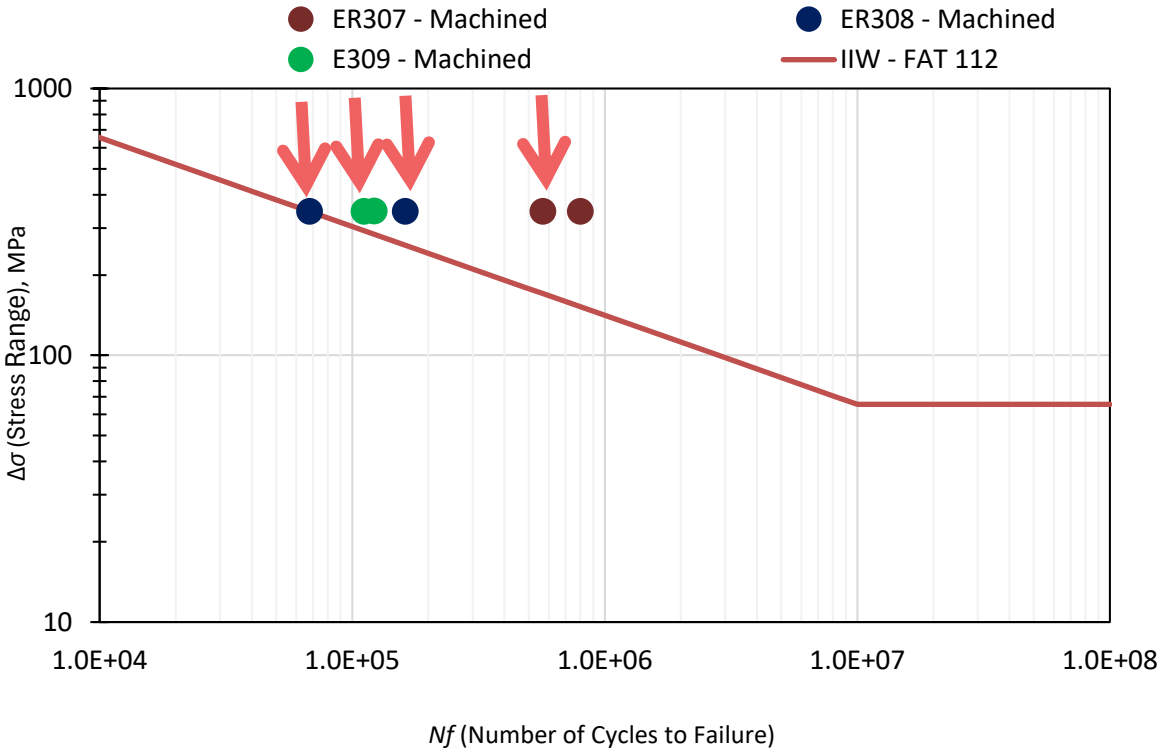


Figure 57: Number of cycles to failure for a stress applied of 85% yield stress.

The fracture surfaces of the specimens marked in Figure 57 were analysed under a stereo microscope. The fracture of ER307-01 (Figure 58) exhibits characteristics of a ductile fracture mode, clearly revealing the crack initiation site and the associated propagation lines.

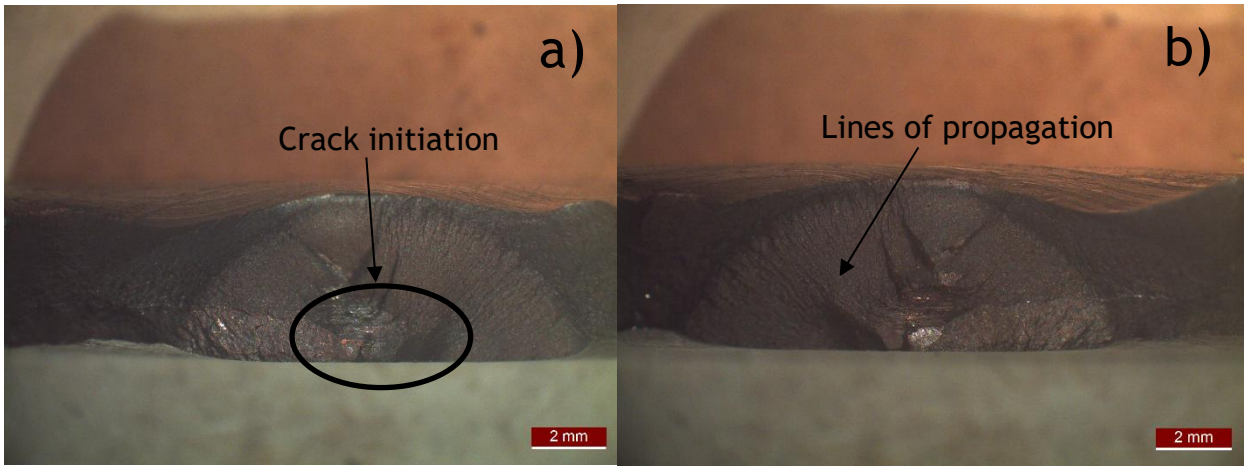


Figure 58: Fracture surface of ER307-01: a) on the AISI 301LN steel side; b) on the S355J2 steel side.

The fracture surface of ER308-1, Figure 59 a) and Figure 59 b), exhibits two distinct zones: on the left, a brittle region, while on the right, a ductile region with a less pronounced propagation line. Adjacent to this region, a lack of fusion defect is observed, which extends to the lateral of the specimen, as seen in Figure 59 c). Possibly, this defect led to localised stress concentrations that served as preferential sites for crack initiation.

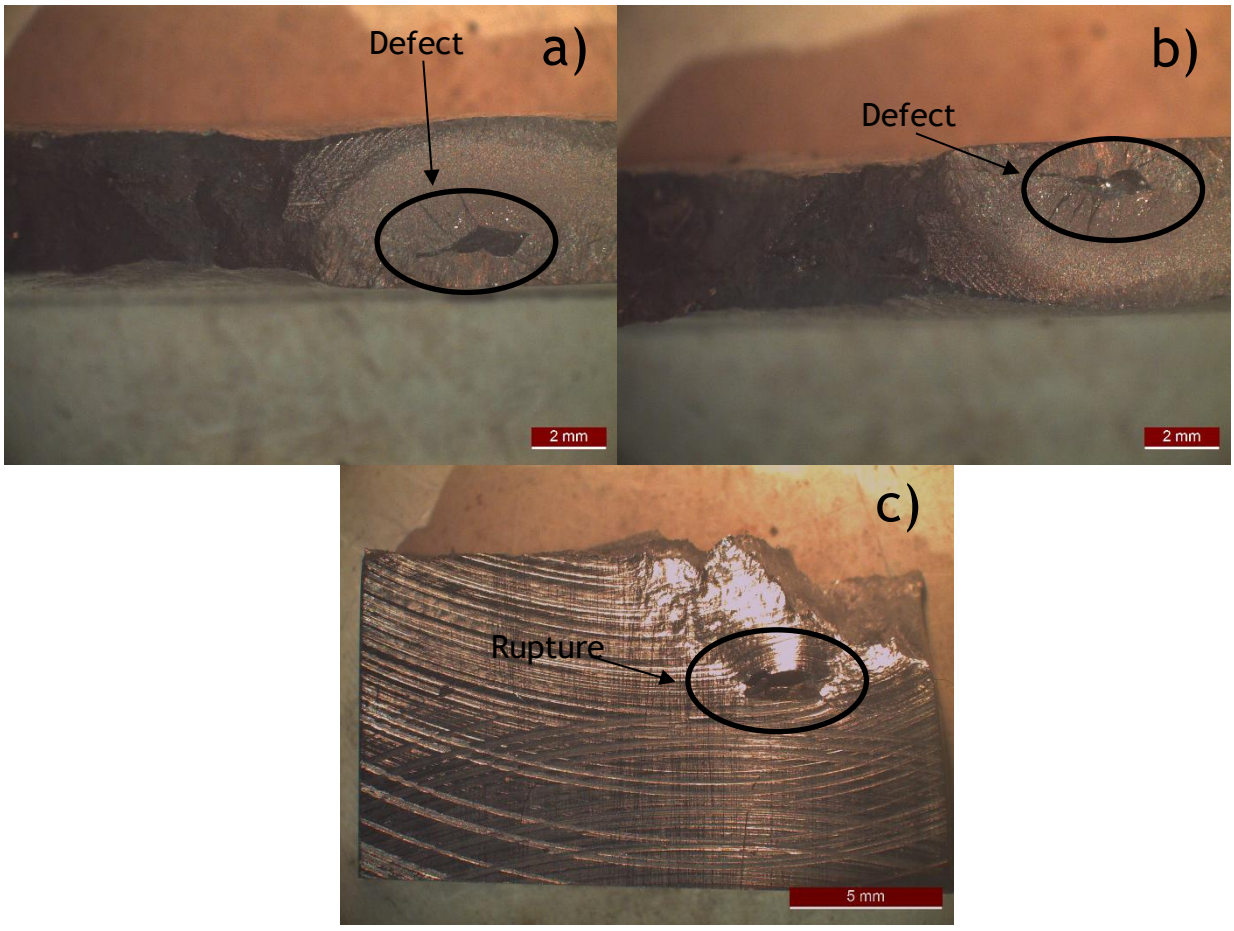


Figure 59: Fracture surface of ER308-01: a) on the AISI 301LN steel side; b) on the S355J2 steel side; c) lack of fusion defect extended to the lateral surface on the S355J2 steel side.

The fracture of ER308-2 (Figure 60) exhibits characteristics of a brittle fracture mode and multiple defects, namely, pores and lack of fusion associated with this type of joint. This may explain why the specimens experienced the fewest cycles till failure.

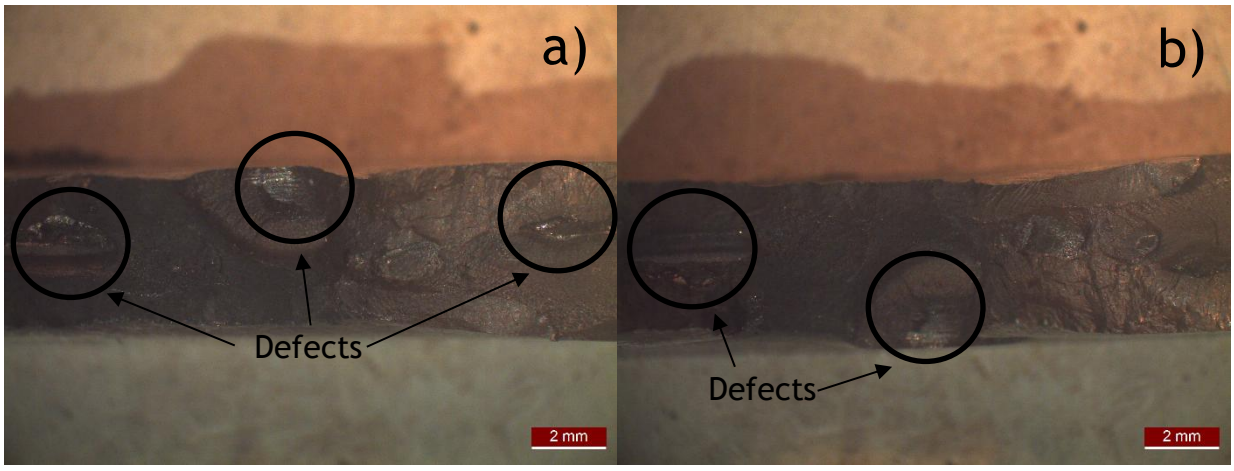


Figure 60: Fracture surface of ER308-02: a) on the AISI 301LN steel side; b) on the S355J2 steel side.

The fracture of ER309-01 (Figure 61) exhibits a small ductile region and a predominantly brittle region, along with several defects distributed across the surface.

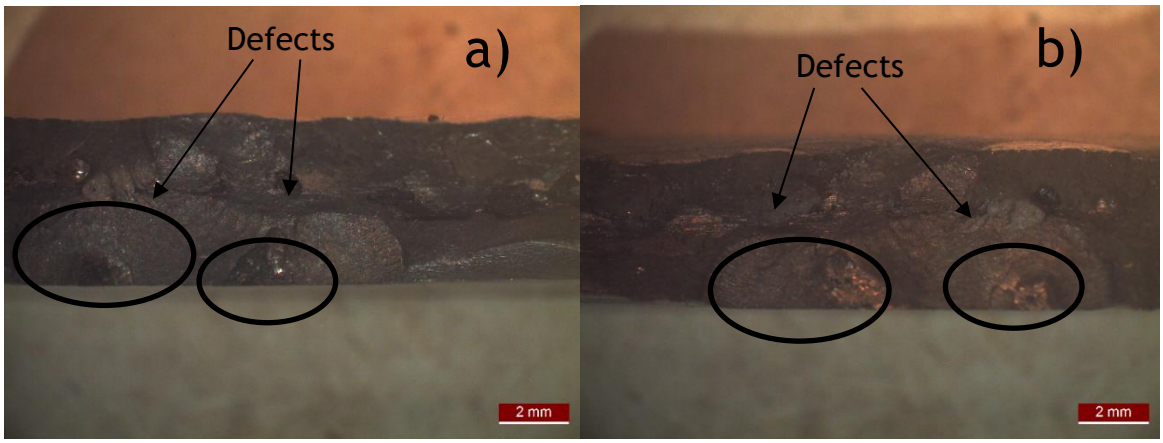


Figure 61: Fracture surface of ER309-01: a) on the AISI 301LN steel side; b) on the S355J2 steel side.

It was also tested on non-machined specimens to assess the fatigue performance of the welded joints to reproduce conditions representative of in-service welded joints in railway vehicles. It was also applied a stress at 85% of the lowest yield stress (429 MPa). These specimens fractured between the weld metal and the AISI 301LN stainless steel.

Table 23 presents the fatigue test results, and Figure 62 provides a graphical representation of them. These results show a high level of consistency.

When comparing these specimens with their machined counterparts, there is a general tendency for the machined ones to exhibit a higher number of cycles till failure. An exception is specimen E309-03, which outperforms the others, possibly due to its fewer internal defects compared with other specimens. The difference in performance between the two types of specimens may be explained by the machining process, which increases the radius of the weld toe. This results in a smoother transition between the weld material and the base material, leading to lower stress concentrations [34].

Analysing these results with the line IIW FAT 72, the ER308-03 is below the expectations, while ER308-05 is at the limit of satisfactory results. The other specimens are above the line, so they would be accepted. This can be explained as stated before, a lack of fusion was registered in multiple places, acting as small cracks, thereby eliminating the crack initiation phase of the specimen's fatigue life [36,47]. Further tests would be necessary to validate these preliminary tests with non-machined specimens.

Table 23: Fatigue results for non-machined specimens.

Specimen Reference	Stress Range (MPa)	Nf (cycles)
ER307-03	346.34	$7{,}95 \times 10^4$
ER307-04		$6{,}59 \times 10^4$
ER307-05		$4{,}67 \times 10^4$
ER308-03		$1{,}32 \times 10^4$
ER308-04		$3{,}42 \times 10^4$
ER308-05		$1{,}70 \times 10^4$
ER309-03		$3{,}86 \times 10^5$
ER309-04		$3{,}50 \times 10^4$

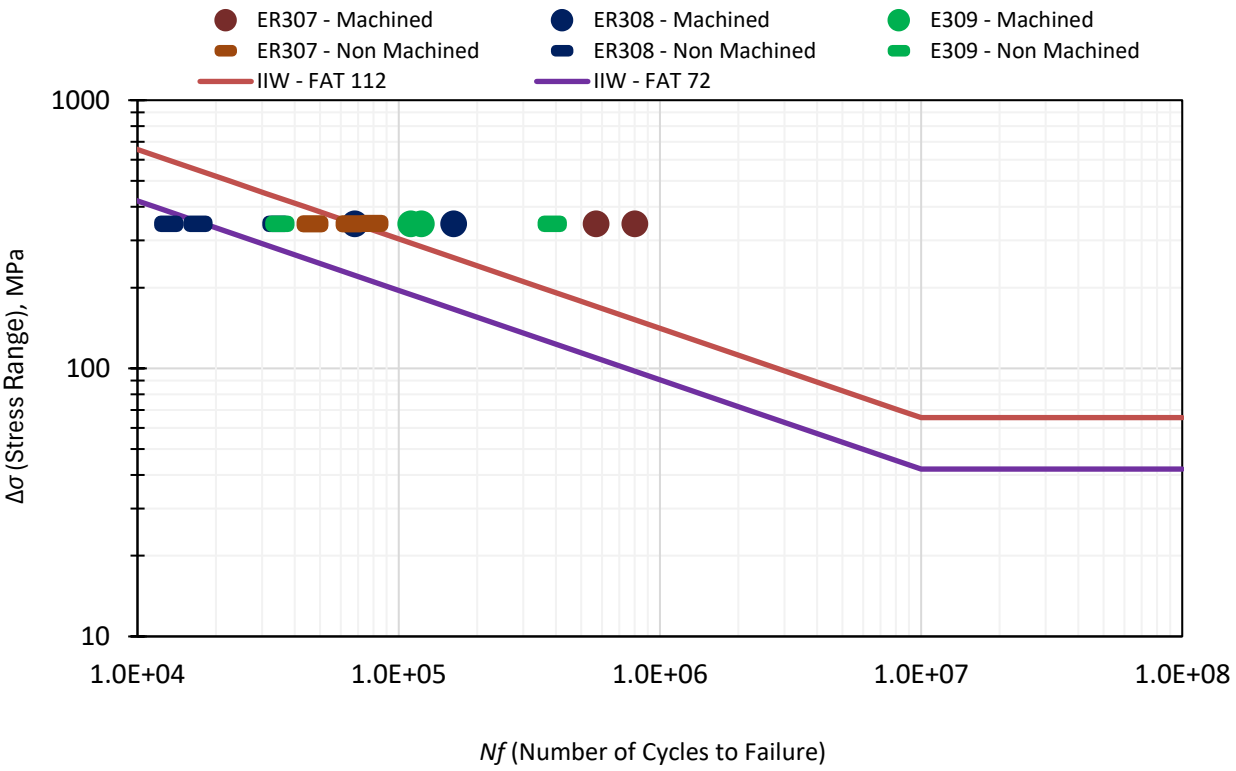


Figure 62: S-N curve for machined and non-machined specimens.

Another characteristic of the non-machined specimens is that they exhibit a brittle and ductile fracture (Figure 63).



Figure 63: Fracture surface of non-machined specimens.

5 CONCLUSIONS AND FUTURE WORK

This dissertation investigated the metallurgical and mechanical properties of dissimilar welded joints between structural steel S355J2 and austenitic stainless steel AISI 301LN, to determine the most suitable filler metal for the floor structure of a railway vehicle. Three filler metals, AWS A5.9 ER307, AWS A5.9 ER308LSi and AWS A5.22 E309LMoT0-1/4, were evaluated using the MAG welding.

From the results of the conducted tests, the following conclusions can be drawn:

- The Schaeffler diagram did not show any accuracy whatsoever, possibly because the dilution percentage of the filler metal was not known, and the diagram by itself is not very rigorous.
- The WRC diagram allowed an approximation of the solidification mode and was accurate in the prediction of the microstructure of joints.
- Regarding the base materials, both exhibited mechanical properties close to the standard specifications.
- The joint with AWS A5.9 ER307 and AWS A5.22 E309LMoT0-1/4 showed no visible defects. In the joint with AWS A5.9 ER308LSi, macrostructure analysis revealed multiple areas of lack of fusion between the weld metal and S355J2. Through microstructure analysis, it can be stated that the Widmanstätten ferrite in the HAZ of S355J2 was formed at a cooling rate higher than the ferrite equiaxial, possibly near 10 ºC/s.
- About the mechanical properties of these joints, the AWS A5.9 ER307 had an ultimate tensile strength of 550 MPa, a yield strength of 452 MPa and an elongation of 16%. The AWS A5.9 ER308LSi had an ultimate tensile strength of 550 MPa, a yield strength of 465 MPa and an elongation of 14%. The joint with AWS A5.22 E309LMoT0-1/4 had an ultimate tensile strength of 499 MPa, a yield strength of 429 MPa, and an elongation of 15%. In the machine specimens, the joints with AWS A5.9 ER307 had the highest number of cycles to failure ($5.69x10^5$ and $8.00x10^5$) with the same stress range as the other joints, as well as ductile fracture. In the non-machined specimens, all but one specimen (AWS A5.22 E309LMoT0-1/4) had a lower number of cycles to failure than the machined one, as expected. Since this specimen was an exception, joints with the filler metal AWS A5.9ER307 are the best option.

In general, this dissertation is of great importance due to the detailed characterisation of dissimilar joints involving materials with substantial differences in thickness and chemical composition, applied within a real industrial context, and demonstrating the feasibility of properly executed MAG welding for structures subjected to high cyclic loading. Nonetheless, the study presents certain limitations. For future research, it is recommended to explore other joint geometries and include more specimens in fatigue tests to enable a more precise decision regarding the implementation of these materials in the train floor. Additionally, it is recommended to implement a method to measure the cooling rate on both sides of the joint and apply the dilatometry test results in the procedure.

REFERENCE

[1] European Comission. July 2025, 'European Commission adopts 9th report on development of the rail market'. Accessed: Aug. 11, 2025. [Online]. Available: https://transport.ec.europa.eu/news-events/news/european-commission-adopts-9th-report-development-rail-market-2025-07-30_en

[2] CP Comboios de Portugal. December 2023, 'Producing railway rolling stock in Portugal'. Accessed: Jun. 26, 2025. [Online]. Available: https://www.cp.pt/institucional/en/press/news/producing-railway-rolling-stock

[3] Train Solutions Portugal. 2023, 'Producing Railway Rolling Stock in Portugal'. Accessed: Jun. 26, 2025. [Online]. Available: https://trainsolutions.pt/uploads/oC43wF3Y9LJwYfN5Z0HV.pdf

[4] SERMEC Group. 2017, 'O Grupo SERMEC The Road of Tomorrow'. Accessed: Jun. 27, 2025. [Online]. Available: https://www.sermec2.pt/group.php#sermec

[5] Train Solutions Portugal. 2024, 'Producing Railway Rolling Stock in Portugal: Mobilizing Agendas for Business Innovation'. Accessed: Jun. 27, 2025. [Online]. Available: https://trainsolutions.pt/en/#entidades

[6] J. Martin, 'Metal and alloys', in *Materials for Engineering*, 3ª., Cambridge England: Woodhead Publishing Limited, 2006, pp. 71–132.

[7] Metalore Foundation for future. 2016, 'Common Applications of S355 Structural Steel Plate'. Accessed: Feb. 19, 2025. [Online]. Available: https://www.metalore.co.in/blog/common-applications-of-s355-structural-steel-plate/

[8] Instituto Português da Qualidade, *Produtos laminados a quente de aços de construção Parte 2: Condições técnicas de fornecimento para aços de construção não ligados*, (NP EN 10025-2: 2007), 2007.

[9] Eurocode Applied.com. 2017, 'Eurocode 3 Table of design material properties for structural steel'. Accessed: Jul. 03, 2025. [Online]. Available: https://eurocodeapplied.com/design/en1993/steel-design-properties

[10] Ovako. January 2025, 'Material data sheet Steel grade S355J2'. Accessed: Jul. 03, 2025. [Online]. Available: https://steelnavigator.ovako.com/steel-grades/s355j2/

[11] M. Ohring, 'Thermodynamics of Solids', in *Engineering Materials Science*, 1ª., Academic Press, 1995, pp. 189–246.

[12] S. Banerjee and P. Mukhopadhyay, 'Diffusional Transformations', in *Phase Transformations Examples from Titanium and Zirconium Alloys*, vol. 12, in Pergamon Materials Series, vol. 12. , Elsevier, 2007, pp. 555–716.

[13] M. Kubiak, W. Piekarska, T. Domański, and Z. Saternus, 'Modelling of Phase Transformations in Solid State and Dilatometric Curves Using Interpolation Methods to Determine CCT Diagrams', *Acta Phys. Pol. A*, vol. 142, pp. 184–187, Jul. 2022, doi: 10.12693/APhysPolA.142.184.

[14] I. Guru. 14/9/2014, 'Copper in Steels'. Accessed: Aug. 13, 2025. [Online]. Available: https://www.ispatguru.com/copper-in-steels

[15] R. Singh, 'Stainless steels and other CRAs', in *Applied Welding Engineering Processes, Codes, and Standards*, 3ª., Elsevier, 2020, pp. 77–84.

[16] CIVMATS. 2025, 'Austenitic STAINLESS STEEL 301 (UNS S30100 / W.Nr. 1.4319)'. Accessed: Mar. 03, 2025. [Online]. Available: https://www.civmats.com/grades/GRADES-301.HTML

[17] European Committee for Standardization, *Stainless steels - Part 2: Technical delivery conditions for sheet/plate and strip of corrosion resisting steels for general purposes*, (EN 10088-2: 2005), Brussels., 2005.

[18] J. A. Brooks and J. C. Lippold, 'Selection of Wrought Austenitic Stainless Steels', in *Welding, Brazing, and Soldering*, vol. 6, United States of America: ASM International, 1993, pp. 1155–1189.

[19] R. Singh, 'Welding, corrosion-resistant alloys—Stainless steel', in *Applied Welding Engineering Processes, Codes, and Standards*, 3ª., Elsevier, 2020, pp. 251–271.

[20] European Committee for Standardization, *Stainless steels - Part 1: List of stainless steels*,

(EN 10088-1:2014), Brussels., Oct. 2014.
[21] D. J. Kotecki, 'Welding of Stainless Steels', in *Welding, Brazing, and Soldering*, vol. 6, United States of America: ASM International, 1993, pp. 1649–1728.
[22] A. Järvenpää, M. Jaskari, T. Juuti, and P. Karjalainen, 'Demonstrating the Effect of Precipitation on the Mechanical Stability of Fine-Grained Austenite in Reversion-Treated 301LN Stainless Steel', *Metals*, vol. 7, no. 9, p. 344 (1–13), Sep. 2017, doi: 10.3390/met7090344.
[23] S. Baskutis, J. Baskutiene, R. Bendikiene, A. Ciuplys, and K. Dutkus, 'Comparative Research of Microstructure and Mechanical Properties of Stainless and Structural Steel Dissimilar Welds', *Materials*, vol. 14, no. 20, p. 6180 (1–15), Oct. 2021, doi: 10.3390/ma14206180.
[24] Y. Suzuki, 'Railway industry', in *Handbook of Adhesion Technology*, vol. 2, Berlin, Heidelberg: Springer, 2011, pp. 1214–1215.
[25] R. Carpmael *et al.*, 'Discussion on Some Developments in Railway - Carriage and Wagon Construction', *J. Inst. Civ. Eng.*, vol. 3, no. 7, p. 283, Jun. 1936, doi: 10.1680/ijoti.1936.14829.
[26] J. Ihme, 'Supporting Structures and Superstructures of Railway Vehicles', in *Rail Vehicle Technology*, Wiesbaden: Springer, 2022, pp. 215–270.
[27] W. Jaxa-Rozen, 'Cold-worked austenitic stainless steels in passenger railcars and in other applications', *Thin-Walled Struct.*, vol. 83, pp. 190–199, Oct. 2014.
[28] Y.-L. Lee, 'Fatigue damage theories', in *Fatigue Testing and Analysis*, Elsevier, 2005, pp. 57–76.
[29] J. J. J. De Cisneros Fonfría, E. Olmeda, S. Sanz, M. Garrosa, and V. Díaz, 'Failure analysis of a train coach underframe', *Eng. Fail. Anal.*, vol. 156, pp. 1–13, Feb. 2024, doi: 10.1016/j.engfailanal.2023.107756.
[30] M. Vogt, K. Dilger, and M. Kassner, 'Investigations on different fatigue design concepts using the example of a welded crossbeam connection from the underframe of a steel railcar body', *Int. J. Fatigue*, vol. 34, no. 1, pp. 47–56, Jan. 2012, doi: 10.1016/j.ijfatigue.2011.01.017.
[31] European Committee for Standardization, *Railway applications - Welding of railway vehicles and components - Part 3: Design requirements*, (EN 15085-3:2022+A1), Brussels., Apr. 2023.
[32] Y.-L. Lee and D. Taylor, 'Stress-Based Fatigue Analysis And Design', in *Fatigue Testing and Analysis*, Elsevier, 2005, pp. 103–180.
[33] W. Fricke, 'Fatigue analysis of welded joints: state of development', *Mar. Struct.*, vol. 16, no. 3, pp. 185–200, May 2003, doi: 10.1016/S0951-8339(02)00075-8.
[34] G. Kang and H. Luo, 'Review on fatigue life prediction models of welded joint', *Acta Mech. Sin.*, vol. 36, no. 3, pp. 701–726, May 2020, doi: 10.1007/s10409-020-00957-0.
[35] G. A. M. Mendes, 'Fadiga de juntas soldadas em aços estruturais de alto limite elástico', Master Thesis, Faculty of Science and Technology of the University of Coimbra, 2009.
[36] P. J. Haagensen, 'Fatigue strength improvement methods', in *Fracture and Fatigue of Welded Joints and Structures*, in Woodhead Publishing Series in Welding and Other Joining Technologies. , Cambridge UK: Woodhead Publishing Limited, 2011, pp. 297–329.
[37] M. A. Kumbhalkar, D. V. Bhope, and A. V. Vanalkar, 'Finite Element Analysis of Rail Vehicle Suspension Spring for Its Fatigue Life Improvement', in *Advanced Manufacturing and Materials Science*, in Lecture Notes on Multidisciplinary Industrial Engineering. , Cham: Springer, 2018, pp. 39–53.
[38] Y.-L. Lee, 'Introduction to stress-based fatigue life estimations', in *Metal Fatigue Testing and Analysis Theory and Pratice*, Elsevier, 2025, pp. 37–77.
[39] K. Weman, 'Introduction to welding', in *Welding Processes Handbook*, 2ª., in Woodhead Publishing Series in Welding and Other Joining Technologies. , Cambridge UK: Woodhead Publishing Limited, 2012, pp. 1–12.
[40] P. Kah, M. Shrestha, and J. Martikainen, 'Trends in Joining Dissimilar Metals by Welding', *Appl. Mech. Mater.*, vol. 440, pp. 269–276, Oct. 2013, doi:

10.4028/www.scientific.net/amm.440.269.
[41] R. E. Avery. May 1991, 'Guidelines for Welding Dissimilar Metals'. Accessed: May 04, 2025. [Online]. Available: https://nickelinstitute.org/media/o3dnv2vx/14018_guidelinesforweldingdissimilarmetals.pdf
[42] F. Silva, *Tecnologia da Soldadura. Uma Abordagem Técnico-Didática*, vol. 1. Porto: Publindústria, 2014.
[43] M. Bäck, 'Welding of dissimilar metals in different welding positions', Master Thesis, KTH Royal Institute of Technology School of Engineering Sciences, Stockholm, 2015.
[44] C. H. Cheng, L. C. Chan, and C. L. Chow, 'Weldment properties evaluation and formability study of tailor-welded blanks of different thickness combinations and welding orientations', *J. Mater. Sci.*, vol. 42, pp. 5982–5990, Aug. 2007, doi: 10.1007/s10853-006-1126-0.
[45] M. Dourado *et al.*, 'A comparative study of fatigue behaviour of MAG and laser welded components using reliability analysis', *Mater. Sci. Eng. A*, vol. 606, pp. 31–39, Jun. 2014, doi: 10.1016/j.msea.2014.03.067.
[46] R. Singh, 'Stresses, Shrinkage, and Distortion in Weldments', in *Applied Welding Engineering Processes, Codes, and Standards*, 2ª., Elsevier, 2016, pp. 201–238.
[47] S. J. Maddox, 'Significant features of welds in relation to fatigue', in *Fatigue Strength of Welded Structures*, 2ª., in Woodhead Publishing Series in Welding and Other Joining Technologies. , Cambridge England: Woodhead Publishing Limited, 1991, pp. 19–29.
[48] W. Fricke, 'Fatigue strength assessment of local stresses in welded joints', in *Fracture and Fatigue of Welded Joints and Structures*, in Woodhead Publishing Series in Welding and Other Joining Technologies. , Cambridge UK: Woodhead Publishing Limited, 2011, pp. 115–138.
[49] R. Singh, 'Weld Defects and Inspection', in *Applied Welding Engineering. Processes, Codes, and Standards*, 2ª., Elsevier, 2016, pp. 277–295.
[50] Sodel, 'Cold Cracking Of Welds'. Accessed: Mar. 04, 2025. [Online]. Available: https://www.sodel.com/medias/iw/cold-cracking-of-welds-sodel.pdf (This is a document and is non-dated)
[51] H. Granjon, 'Hardening and cold cracking in steel welding', in *Fundamentals of Welding Metallurgy*, in Woodhead Publishing Series in Welding and Other Joining Technologies. , Cambridge England: Woodhead Publishing Limited, 1991, pp. 156–177.
[52] S. E. Hughes, 'Fracture Modes and Welding Defects', in *A Quick Guide to Welding and Weld Inspection*, in Woodhead Publishing Series in Welding and Other Joining Technologies. , Cambridge UK: Woodhead Publishing Limited, 2009, pp. 88–107.
[53] G. Mathers, 'Welding metallurgy', in *The Welding of Aluminium and its Alloys*, in Woodhead Publishing Series in Welding and Other Joining Technologies. , Cambridge England: Woodhead Publishing Limited, 2002, pp. 10–34.
[54] P. R. Vishnu, 'Solid-State Transformations in Weldments', in *Welding, Brazing, and Soldering*, vol. 6, United States of America: ASM International, 1993, pp. 162–356.
[55] J. A. Siefert and S. A. David, 'Weldability and weld performance of candidate austenitic alloys for advanced ultrasupercritical fossil power plants', *Sci. Technol. Weld. Join.*, vol. 19, no. 4, pp. 271–294, May 2014, doi: 10.1179/1362171814Y.0000000197.
[56] Nickel Institute, *Welding of Stainless Steels and other Joining Methods - A Designers' Handbook Series No 9002*. Toronto, Ontario: Nickel Institute, 2020.
[57] H. Cerjak and P. Mayr, 'Creep strength of welded joints of ferritic steels', in *Creep-Resistant Steels*, in Woodhead Publishing Series in Metals and Surface Engineering. , Cambridge England: Woodhead Publishing Limited, 2008, pp. 472–503.
[58] S. E. Hughes, 'Materials and Their Weldability', in *A Quick Guide to Welding and Weld Inspection*, in Woodhead Publishing Series in Welding and Other Joining Technologies. , Cambridge England: Woodhead Publishing Limited, 2009, pp. 36–48.
[59] European Committee for Standardization, *Hot rolled products of structural steels - Part 1: General technical delivery conditions*, (EN 10025-1: 2004), Brussels., Nov. 2004.

[60] A. Celik and A. Alsaran, ‘Mechanical and Structural Properties of Similar and Dissimilar Steel Joints’, *Mater. Charact.*, vol. 43, no. 5, pp. 311–318, Nov. 1999, doi: 10.1016/S1044-5803(99)00045-5.
[61] K. Weman, ‘The weldability of steel’, in *Welding Processes Handbook*, 2ª., in Woodhead Publishing Series in Welding and Other Joining Technologies. , Cambridge UK: Woodhead Publishing Limited, 2012, pp. 191–206.
[62] ASM Committee, ‘Material Requirements for Service Conditions’, in *Welding, Brazing, and Soldering*, vol. 6, United States of America: ASM International, 1993, pp. 976–2621.
[63] Tongchuang. March 2025, ‘What is a Heat Sink in Welding?’ Accessed: Jun. 10, 2025. [Online]. Available: https://www.tchthermal.com/blogs/news/what-is-a-heat-sink-in-welding
[64] European Committee for Standardization, *Railway applications - Welding of railway vehicles and components - Part 4: Production requirements*, (EN 15085-4:2023), Brussels., Mar. 2023.
[65] J. G. Feldstein, ‘Dissimilar Welds With Stainless Steels’, in *Welding, Brazing, and Soldering*, vol. 6, United States of America: ASM International, 1993, pp. 1264–1273.
[66] J. R. Davis, ‘Hardfacing, Weld Cladding, and Dissimilar Metal Joining’, in *Welding, Brazing, and Soldering*, vol. 6, United States of America: ASM International, 1993, pp. 1952–2044.
[67] Suheni, A. A. Rosidah, D. P. Ramadhan, T. Agustino, and F. F. Wiranata, ‘Effect of Welding Groove and Electrode Variation to the Tensile Strength and Macrostructure on 304 Stainless Steel and AISI 1045 Dissimilar Welding Joint Using SMAW Process’, *J. Phys. Conf. Ser.*, vol. 2117, no. 012018, pp. 1–6, Nov. 2021, doi: 10.1088/1742-6596/2117/1/012018.
[68] J. L. Marulanda Arevalo, V. M. Burbano, and J. A. Peláez, ‘Análisis de soldabilidad de aceros inoxidables con aceros de medio y bajo carbono por SMAW’, *Rev. Fac. Ing.*, vol. 22, no. 35, pp. 91–100, Dec. 2013, doi: 10.19053/01211129.2517.
[69] L. Nhung, P. Mai Khanh, A. Tuan Hoang, and D. Nam Nguyen, ‘Microstructure Change For Multi-Pass Welding Between Austenitic Stainless Steel And Carbon Steel’, *J. Mech. Eng. Res. Dev.*, vol. 41, no. 2, pp. 97–102, Jul. 2018, doi: 10.26480/jmerd.02.2018.97.102.
[70] B. Szczucka-Lasota and T. Węgrzyn, ‘Improvement Of The Mechanical Properties Of Mobile Platform Stainless Construction Elements’, *Transp. Probl.*, vol. 17, no. 4, pp. 91–102, Dec. 2022, doi: 10.20858/tp.2022.17.4.08.
[71] K. E. Easterling and H. Cerjak, ‘Modelling the Evolution of Microstructure in Steel Weld Metal’, in *Mathematical Modelling of Weld Phenomena*, vol. 1º, London, 1993, pp. 109–182.
[72] C. C. C. and P. Abe, ‘Influence of Welding on Steel Weldment Properties’, in *Welding, Brazing, and Soldering*, vol. 6, United States of America: ASM International, 1993, pp. 1068–1093.
[73] K. Weman, ‘MIG/MAG welding’, in *Welding Processes Handbook*, 2ª., in Woodhead Publishing Series in Welding and Other Joining Technologies. , Cambridge UK: Woodhead Publishing Limited, 2012, pp. 75–97.
[74] Weldas Europe. 2025, ‘Comparison of welding processes: MIG and MAG welding’. Accessed: Aug. 25, 2025. [Online]. Available: https://www.weldaseurope.com/knowledge-base/difference-mig-mag-welding
[75] ESAB University. March 2022, ‘MIG Welding: Techniques, Advantages and Applications’. Accessed: Aug. 25, 2025. [Online]. Available: https://esab.com/pt/eur_en/esab-university/blogs/mig-welding-techniques-advantages-and-applications
[76] Universal Technical Institute. July 2025, ‘What Is Metal Active Gas (MAG) Welding?’ Accessed: Aug. 25, 2025. [Online]. Available: https://www.uti.edu/blog/welding/gmaw-mag-welding
[77] I. Davila-Rios, I. Lopez-Juarez, L. Martinez-Martinez, and L. M. Torres-Treviño, ‘Implementation of an Intelligent Robotized GMAW Welding Cell, Part 1: Design and Simulation’, in *Robot Manipulators Trends and Development*, InTechOpen, 2010, pp. 543–562.

[78] D. Naidu, K. Moore, and S. Ozcelik, 'Gas Metal Arc Welding: Modeling', in *Modeling, Sensing and Control of Gas Metal Arc Welding*, Oxford UK: Elsevier, 2003, pp. 9–93.
[79] D. H. Phillips, 'Arc Welding Processes', in *Welding Engineering An Introduction*, Chichester United Kingdom: John Wiley & Sons, 2016, pp. 4–73.
[80] R. Singh, 'Physics of welding', in *Applied Welding Engineering*, 3ª., Elsevier, 2020, pp. 125–155.
[81] R. Singh, 'Physical Effect of Heat on Material During Welding', in *Applied Welding Engineering*, 2ª., Elsevier, 2016, pp. 197–200.
[82] R. Khatri, 'Measurement of Cooling Time in Welding', Master Thesis, Hame University of Applied Sciences, 2020.
[83] R. Kumar, H. K Arya, and R. K. Saxena, 'Experimental Determination of Cooling Rate and its Effect on Microhardness in Submerged Arc Welding of Mild Steel Plate (Grade c-25 as per IS 1570)', *J. Mater. Sci. Eng.*, vol. 3, no. 2, pp. 1–4, 2014, doi: 10.4172/2169-0022.1000138.
[84] K. A. Lyttle, 'Shielding Gases for Welding', in *Welding, Brazing, and Soldering*, vol. 6, United States of America: ASM International, 1993, pp. 148–306.
[85] SERMEC Group. Unpublished certificate, 'Quality Certificate of S355J2'. Mar. 20, 2024.
[86] SERMEC Group. Unpublished certificate, 'Inspection certificate of 1.4318- X2CrNiN18-7 AISI 301LN'. Feb. 14, 2025.
[87] SERMEC Group. Unpublished certificate, 'Quality Certificate of AWS A5.9 ER307'. Mar. 08, 2021.
[88] SERMEC Group. Unpublished certificate, 'Inspection certificate of AWS A 5.9 ER308LSi'. Jan. 17, 2023.
[89] SERMEC Group. Unpublished certificate, 'Inspection certificate of AWS A 5.22 E309LMoT0-1/4'. Jan. 21, 2020.
[90] C. García De Andrés, F. G. Caballero, C. Capdevila, and L. F. Álvarez, 'Application of dilatometric analysis to the study of solid–solid phase transformations in steels', *Mater. Charact.*, vol. 48, no. 1, pp. 101–111, Feb. 2002, doi: 10.1016/S1044-5803(02)00259-0.
[91] K. Zhang, W. Dong, and S. Lu, 'Finite element and experiment analysis of welding residual stress in S355J2 steel considering the bainite transformation', *J. Manuf. Process.*, vol. 62, pp. 80–89, Feb. 2021, doi: 10.1016/j.jmapro.2020.12.029.
[92] International Organization for Standardization, *Welding — Guidelines for a metallic materials grouping system*, (ISO/TR 15608:2017), Geneva Switzerland., 2017.
[93] International Organization for Standardization, *Welding consumables — Gases and gas mixtures for fusion welding and allied processes*, (ISO 14175:2008), Geneva Switzerland., 2008.
[94] SERMEC Group. Unpublished certificate, 'Welding Procedure Qualification Record Nr 031/2023'. Oct. 06, 2023.
[95] American Society for Testing and Materials, *Test Methods for Tension Testing of Metallic Materials*, (E8/E8M − 16a), 2019.
[96] Instituto Português da Qualidade, *Materiais metálicos: Ensaio de tração Parte 1: Método de ensaio à temperatura ambiente*, (NP EN ISO 6892-1:2022), Caparica., 2022.
[97] International Organization for Standardization, *Destructive tests on welds in metallic materials — Transverse tensile test*, (ISO 4136:2022 E), Geneva Switzerland., 2022.
[98] International Organization for Standardization, *Destructive tests on welds in metallic materials — Macroscopic and microscopic examination of welds*, (ISO 17639:2022 E), Geneva Switzerland., 2022.
[99] G. F. Vander Voort, 'Appendix I: Etchants For Revealing Microstructure', in *Metallography: principles and practice*, 4ª., Ohio USA: ASM International, 2007, pp. 610–711.
[100] M. R. Hirsch, 'Fretting Fatigue Of AISI 301 Stainless Steel Sheet In Full Hard Condition', Master Thesis, Georgia Institute of Technology, 2008.
[101] G. Petzow, 'Metallographic Etching', in *Metallographic Etching: Techniques for Metallography, Ceramography, Plastography*, 2ª., ASM International, 1999, pp. 52–102.
[102] International Organization for Standardization, *Metallic materials — Fatigue testing Axial*

force-controlled method, (ISO 1099:2017), Geneva Switzerland., 2017.
[103] A. F. Hobbacher and J. Baumgartner, 'Fatigue Resistance', in *Recommendations for Fatigue Design of Welded Joints and Components*, 3ª., in IIW Collection. , Cham, Switzerland: Springer, 2024, pp. 43–123.
[104] S. A. Rizvi and S. P. Tewari, 'Effect of Different Welding Parameters on the Mechanical and Microstructural Properties of Stainless Steel 304H Welded Joints', *Int. J. Eng.*, vol. 30, no. 10, pp. 1–6, Oct. 2017, doi: 10.5829/ije.2017.30.10a.21.
[105] S. J. Jones and K. D. H. Bhadeshia, 'Kinetics of the Widmanstatten Ferrite Transformation in Steels', in *International Conference on Displacive Phase Transformations and Their Applications in Materials Engineering: in honor of Professor C.M. Wayman on the occasion of his retirement*, Pennsylvania, USA: The Minerals, Metals and Materials Society, 1998, pp. 419–426.

APPENDIX

A Tensile Test Results of base materials

	AISI 301LN			S355J2		
	Test Nº1	Test Nº2	Test Nº3	Test Nº1	Test Nº2	Test Nº3
Rm (MPa)	1004	1013	1029	495	495	496
Rp0.2 (MPa)	792	821	791	411	414	417
A (%)	27	28	28	27	26	28

B Tensile Test results of welded joints

	AWS A5.9 ER307 1º	AWS A5.9 ER307 2º	AWS A5.9 ER308LSi 1º	AWS A5.9 ER308LSi 2º	AWS A5.22 E309LMoT-1/4 1º	AWS A5.22 E309LMoT0-1/4 2º
Rm (MPa)	544	556	546	554	498	499
Rp0.2 (MPa)	445	459	469	462	423	432
A (%)	16	16	14	15	15	16